Plastic spintronics : spin transport and intrinsic magnetoresistance in organic semiconductors

Plastic Spintronics

Spin transport and intrinsic magnetoresistance in organic semiconductors

Wiebe Wagemans

Plastic Spintronics

Spin transport and intrinsic magnetoresistance in organic semiconductors

PROEFSCHRIFT

ter verkrijging van de graad van doctor aan de
Technische Universiteit Eindhoven, op gezag van de
rector magnificus, prof.dr.ir. C.J. van Duijn, voor een
commissie aangewezen door het College voor
Promoties in het openbaar te verdedigen
op maandag 14 juni 2010 om 14.00 uur

door

Wiebe Wagemans

geboren te Arnhem

Dit proefschrift is goedgekeurd door de promotoren:

prof.dr. B. Koopmans
en
prof.dr.ir. H.J.M. Swagten

Copromotor:
dr. P.A. Bobbert

A catalogue record is available from the Eindhoven University of Technology Library.

ISBN 978-90-386-2255-2

This research is supported by the Dutch Technology Foundation STW, which is the applied science division of NWO, and the Technology Programme of the Ministry of Economic Affairs (project number 06628).

Printed by Ipskamp Drukkers B.V., Enschede.

Contents

Preface **5**

1 Introduction **7**
1.1 Organic electronics 7
1.2 Spintronics 12
1.3 Organic spintronics 14
1.3.1 Spin transport in organic materials 15
1.3.2 Organic magnetoresistance effect 17
1.3.3 Models for organic magnetoresistance 20
1.3.4 Comparison of OMAR models with experiments 26
1.4 This thesis 31

2 Measuring organic magnetoresistance **33**
2.1 Introduction 33
2.2 Sample fabrication 34
2.3 Setup 35
2.4 Field Modulation 36
2.5 Photocurrent 38
2.6 Conclusion 41

3 A two-site bipolaron model for organic magnetoresistance **43**
3.1 Introduction 43
3.2 Two-site bipolaron model 44
3.3 Results 46
3.4 Conclusion 49

4 Frequency dependence of organic magnetoresistance **51**
4.1 Introduction 51
4.2 Methods 52
4.3 Results 52

4.4 Discussion . . . 54
4.5 Conclusion . . . 56

5 Angle dependent spin--spin interactions in organic magnetoresistance 57
5.1 Introduction . . . 57
5.2 Experimental . . . 58
5.3 Results . . . 58
5.4 Discussion . . . 60
5.5 Conclusion . . . 66

6 Spin diffusion in organic semiconductors 67
6.1 Introduction . . . 67
6.2 Model . . . 68
6.3 Spin diffusion . . . 69
6.4 Modeling a spin valve . . . 72
6.4.1 Phenomenological device model . . . 73
6.4.2 Fitting of the experimental data to the model . . . 75
6.5 Conclusion . . . 77

7 Angle dependent spin-diffusion length 79
7.1 Introduction . . . 79
7.2 Model . . . 80
7.3 Results . . . 81
7.4 Waiting Time Analysis . . . 83
7.5 Hanle Experiment . . . 86
7.6 Spin Valves . . . 87
7.7 Conclusion . . . 88

8 Extensions of the experiments and models 89
8.1 Extending the two-site bipolaron model with physical parameters . . . 89
8.2 An alternative approach to OMAR line shapes . . . 92
8.3 OMAR and spin injection . . . 97

9 Outlook 101

Summary / Samenvatting 105

Curriculum vitae 111

List of publications 113

Acknowledgements / Dankwoord 115

Bibliography 126

Index 127

Preface

Plastics are widely known for their easy processing and possibilities to make flexible or transparent products with vastly different properties. Most people know plastics for their electrically insulating properties. However, in 1977, it was shown that certain plastics—or organic materials, as they mostly consist of carbon and hydrogen, like living organisms—can conduct electricity. This discovery, which was rewarded with the Nobel Prize in Chemistry in 2000, was the start of the huge research field of organic electronics. All the interesting properties of plastics could now be used in electronics applications. A great boost came in 1987 when the first organic light emitting diode (OLED) was demonstrated, showing that these organic materials can be used for producing light. Since then, this application has rapidly evolved. OLED lighting panels are now commercially available and OLED displays are incorporated in several mobile devices. These displays can even be made flexible, allowing a whole new range of possibilities. Organic solar cells are another promising application. Although their efficiency is still much lower than that of their inorganic counterparts, they are much cheaper and allow roll-to-roll processing in large volumes, which is thought to be essential if solar power has to be scaled up to a level where it can cover a significant part of our power consumption.

A completely different field is the field of spintronics, or spin electronics. In most electronic devices, the charge of electrons is used to transport or store information. Besides a charge, electrons also have a spin, which can be thought of as a small magnet that can either point up or down. It is this property that is used in spintronics. The spin of electrons can be influenced by sending them through a magnetic material, or by applying a magnetic field. One widely used application of spintronics is the read head used in every modern hard disk. This sensor consists of a stack of magnetic and non-magnetic layers that respond to the bits on the disk, which are small magnets that point up (1) or down (0). The current through the stack is different depending on the orientation of the magnets, allowing the stored data to be read electronically using the spin-dependent interactions of the electrons. The change in current is called giant magnetoresistance (GMR)—the discovery of which (in 1988) was rewarded with the Nobel Prize in Physics in 2007. GMR allowed for the fast miniaturization and increase of

storage density of hard disks in the last fifteen years. Another example of a spintronics application is the magnetic random access memory (MRAM), which uses the fact that a magnet preserves its orientation without the need to apply a voltage, like in conventional RAM. This may be used in computers that can be turned on instantly and consume significantly less power.

As both organic electronics and spintronics offer many advantages and possibilities, the combination of the two fields seems to be a logical step. On the one hand, by using spins in organic electronics, new functionalities can be added to existing organic devices. On the other hand, organic materials can be employed in spintronics applications, benefitting from their low cost, ease of processing and chemical tunability. The resulting field of organic spintronics is relatively new and the last couple of years first reports have been made on the successful combination of the fields of organic electronics and spintronics, and even of entirely new phenomena, unique to the field of organic spintronics. It is thus a new and exciting field that is not only interesting because of the new physics that is involved, but also because of the possible applications it promises.

In this thesis, two aspects of organic spintronics are investigated. First (Ch. 2–5), a new magnetic effect in organic materials is investigated. On applying a magnetic field, the resistance of typical organic devices changes, even without the use of magnetic materials. This intrinsic organic magnetoresistance (OMAR) is believed to be the result of the spins of interacting charges. No consensus has been reached yet on the exact origin of this effect. Therefore, both experimental and theoretical results will be presented that aim to further the understanding of OMAR. Second (Ch. 6 and 7), the transport of spin information through organic materials is studied, as this is crucial for successfully using organic materials in spintronics applications like a GMR sensor. It will be shown that due to the type of charge transport characteristic for these materials, spin transport is predicted to show specific properties.

Chapters 2–7 can each be read separately, but the first part of Ch. 1 offers an overview of the basics of organic electronics and spintronics, followed by a review of recent progress in organic spintronics, also indicating how the following chapters fit into this picture. In Ch. 8, three possible extensions of the models and experiments are presented, including suggestions for a combination of the two subjects studied. This is followed by a general outlook on the future of organic spintronics (Ch. 9). Finally, the reader is pointed to an index at the end of this thesis for easy reference of the topics covered.

Wiebe Wagemans, Eindhoven, March 2010.

1 Introduction

The first part of this chapter provides a basic introduction into organic electronics and spintronics, while the last part serves to give a broader perspective on the topics covered in this thesis. This chapter starts with a general introduction of organic electronics. Then, it introduces the basic concepts of spintronics, using the spin valve as an example. After these general sections, we zoom in on the use of organic materials in spintronics, which is the field of organic spintronics. Two topics are discussed in more detail. First, spin transport in organic materials is reviewed, highlighting some of the recent results. Second, an extended overview of organic magnetoresistance is given, starting with describing its main characteristics and explaining the different models. Whereafter these models are compared with a selection of the many experiments available in literature. Finally, the structure of this thesis is explained.

1.1 Organic electronics

Organic electronics, or 'plastic electronics', uses conducting organic materials in electronics applications. The materials we call 'plastics' are organic materials, which consist mostly of carbon and hydrogen. Using organic materials for electronics offers many advantages. They are easy to process and cheap, and also offer new possibilities as they are chemically tunable and can allow for flexible or transparent applications. Many different applications have been developed like organic light-emitting diodes (OLEDs), polymer solar cells, and organic field-effect transistors (OFETs).[31,42,57,130] Many of these applications are already commercially available, for instance in OLED displays. Organic electronics is thus a very broad field containing many sub-fields, which can be considered as mature fields on their own, about which many books, reviews and even journals are published. In this section we will not try to give a full overview, but will merely highlight the topics that are relevant for this thesis.

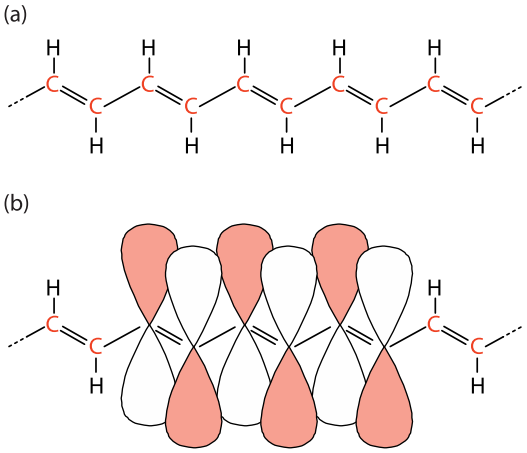

Figure 1.1: (a) Part of a polyacetylene polymer, with alternating single and double bonds. (b) Several p_z orbitals from the carbon atoms.

Origin of conductivity

Conduction in many organic molecules is possible because of π-conjugation, resulting in the presence of alternating single and double bonds in a chain of carbon atoms. Figure 1.1(a) shows part of the structure of the polymer polyacetylene as an example. The carbon atoms each have three sp^2 orbitals, which overlap to form σ-bonds with the adjacent carbon and hydrogen, and one p_z orbital, which overlaps with the neighboring p_z orbitals, see Fig. 1.1(b). This overlap results in the formation of π-bonds, leading to a delocalization of the π-electrons along the molecule, giving the conducting properties. The delocalized electrons occupy the bonding π-orbitals, while the anti-bonding π-orbitals remain empty. The bonding π-orbital with the highest energy is called the highest occupied molecular orbital (HOMO), while the anti-bonding π-orbital with the lowest energy is called the lowest unoccupied molecular orbital (LUMO). These orbitals are comparable to the valence band and conduction band in inorganic semiconductors. Due to a geometric relaxation, the delocalization does not extend over the whole molecule, but single and double bonds are formed. This so-called Peierls distortion leads to the presence of an energy difference, a band gap, of several eV between the HOMO and LUMO. As a result, these organic materials are semiconducting.

The layers of organic materials studied in this thesis are disordered, or amorphous, meaning that no (long-range) order exists between the molecules. Due to this disorder and the weak interaction between molecules, charges are localized on the molecules, or part of the molecule. Linked to the spatial disorder, an energetic disorder of the sites exists, as is illustrated in Fig. 1.2. The density of states is often assumed to be a Gaussian distribution, with a width σ of 75–150 meV.[9,136] Charge transport occurs via hopping between localized sites, which can be described by phonon assisted tunneling. As a result, mobilities in organic semiconductors are several orders smaller than for inorganic semiconductors. A typical value is 10^{-6} cm^2 V^{-1} s^{-1} for the materials used in this thesis.

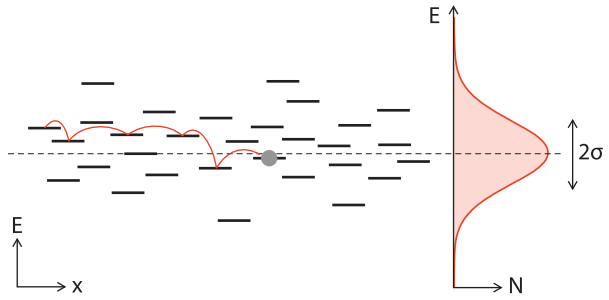

Figure 1.2: Disorder in the energy (E) of localized sites, here illustrated in the x direction (left). The number of sites per energy (N) follows a Gaussian density of states with a width σ (right). The hopping of a carrier is illustrated.

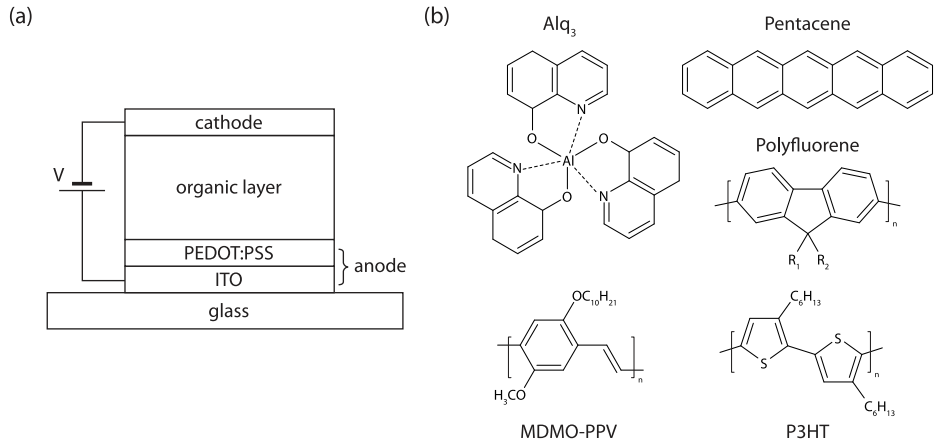

Figure 1.3: (a) Schematic of a vertical device layout. (b) Examples of typical semiconducting polymers and small molecules.

Electrical devices

For electrical applications, charges need to be injected into and extracted from the organic layer. This is usually done with (metal) electrodes. Figure 1.3(a) illustrates a typical lay-out, where an organic layer is sandwiched between two electrodes. As the anode, transparent indium tin oxide (ITO) is used, to allow light output, in combination with a layer of poly(3,4-ethylenedioxythiophene): poly(styrenesulfonate) (PEDOT:PSS). For the active layer, many different organic materials can be used. Here, we typically use the small molecule tris-(8-hydroxyquinoline) aluminum (Alq_3), which is thermally evaporated in vacuum, or the polymer poly[2-methoxy-5-(3',7'-dimethyloctyloxy)-1,4-phenylene vinylene] (MDMO-PPV), which is spin-coated from solution. Both molecular structures are shown in Fig. 1.3(b) with several other examples. As the cathode, we typically use a very thin layer of LiF, capped with aluminum.

In first order, the alignment of the work functions of the electrodes with the HOMO and LUMO determines the efficiency of charge injection. A typical case is sketched in Fig. 1.4(a). With a low work function (Φ_e), best alignment is achieved with the LUMO

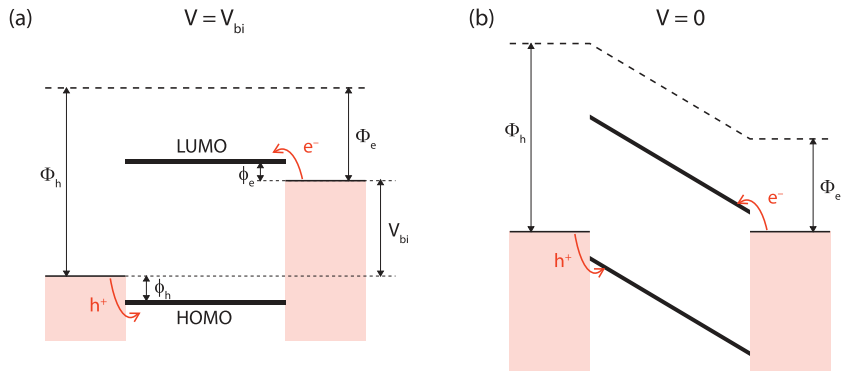

Figure 1.4: Energy diagrams of an organic device with hole (electron) injection barriers $\phi_{h(e)}$, and electrode work functions $\Phi_{h(e)}$. For an applied bias (a) $V = V_{bi}$ (b) $V = 0$.

and electrons (e) are easiest injected. On the other hand, a high work function (Φ_h) facilitates hole (h) injection. In reality, additional effects like the formation of interface dipoles can also play a role. If an energy difference between the electrode and the HOMO or LUMO exists, an injection barrier ϕ can be present. Depending on the height of the barrier, the transport of the specific carrier is injection limited. In absence of a barrier, the contact is Ohmic. By choosing specific combinations of electrode materials, it is possible to tune which carriers are present; only electrons or only holes (single-carrier, or unipolar), or both electrons and holes (double-carrier, or bipolar). At zero bias, the Fermi energies of the electrodes are aligned [Fig. 1.4(b)], resulting in a reverse electric field in the organic layer. Charges can only be efficiently injected when the applied voltage is such that this electric field is at least balanced, so for a voltage that is equal to or larger than the built-in voltage V_{bi} [Fig. 1.4(a)].

Charges in organic materials

Once charges are injected, they move to the other electrode under the influence of the local electric field in the device. These charges induce a displacement of the nearby atoms, lowering the total energy. The charge and its distortion are called a polaron.* When two like charges meet, they will feel a Coulomb repulsion, but they also benefit from sharing their polaronic distortion. If this balance is positive, a stable bipolaron can be formed. Opposite charges also interact and can recombine to produce light—a property that is exploited in OLEDs. This process starts by the electron and hole becoming Coulombically bound; they form an e–h pair, which is also called a polaron pair. When decreasing their separation so that their wave functions overlap, exchange interactions become important and, only then, the pair is called an exciton.

Pairs of charges (each charge with spin $\frac{1}{2}$) like bipolarons, e–h pairs and excitons can have either total spin 0, which is a singlet (S), or total spin 1, which are triplets (T). The triplets split up in T_-, T_0, and T_+ due to the Zeeman energy under the influence of a magnetic field is applied. The specific spin state is of relevance for interactions and reactions of the pair. Only a pair of charges in the singlet state can form a bipolaron. For

*When we speak of electrons and holes we actually mean negatively and positively charged polarons, respectively.

excitons only singlet excitons can recombine under emission of light due to spin conservation. Because injected charges have a random spin, a S–T ratio of 1:3 is expected, although deviations have been observed and explained. [145]

Charge transport

When applying an electric field to an organic layer, all charge has to be electrically injected when the layer is undoped. Furthermore, the injected charges drift in this electric field to the opposite electrode, giving a typical V^2 behavior of the current. The resulting current is called a space-charge limited current (SCLC), because the current is impeded by the presence of the (space) charge in the device. By solving the Poisson equation and the drift equation for a single-carrier device, the exact relationship (called the Mott–Gurney law) for the current density is: [14]

$$J = \frac{9}{8}\epsilon\mu\frac{V^2}{L^3}, \tag{1.1}$$

with ϵ the electric permittivity, μ either the electron mobility μ_e or the hole mobility μ_h and, L the thickness.

For a double-carrier device, cancelation of net charge by the injection of oppositely charged carriers allows for more carriers at the same space charge and thus a much larger current. Moreover, electrons and holes can also recombine, which reduces the current as they do not transit the whole length of the device. These type of devices exhibit Langevin recombination, which can be characterized by a recombination mobility $\mu_r = r(\mu_e + \mu_h)$, with $r \ll 1$ a constant that is small for weak recombination. Parmenter and Ruppel showed that for ohmic contacts the resulting current density is: [101]

$$J = \frac{9}{8}\epsilon\sqrt{\frac{2\pi\mu_e\mu_h(\mu_e+\mu_h)}{\mu_r}}\frac{V^2}{L^3}. \tag{1.2}$$

The mobilities for holes and electrons are usually different. With 'minority' and 'majority' carriers we will refer to the carriers with the smaller and larger mobility, respectively. So, in a double-carrier device, also a typical V^2 dependence of the current is found. However, many other processes can occur in organic devices, the discussion of which is beyond the scope of this thesis.

One effect worth mentioning is the effect of trapping of carriers. Carriers can become trapped in sites that lie within the band gap of the material. These sites can originate from defects or impurities, but also from the long tail of the density of states. These traps limit the mobility of the carriers as they spend a long time in the trap before being (thermally) released. On increasing the voltage, the current rapidly increases by trap filling. This increase results in a power law dependence of the current, $J \propto V^n$, with $n > 2$. [14] At voltages smaller than the built-in voltage, a small current is already present, which is the result of transport by impurities and defects, and also by diffusion. This current is linear with voltage, $J \propto V^1$. Thus, studying the voltage dependence of the current on a log–log scale can give information about (changes in) the type of conduction.

Besides electrical injection, charges can also be generated by illuminating the organic material—a property that is exploited in organic solar cells. On absorption of a

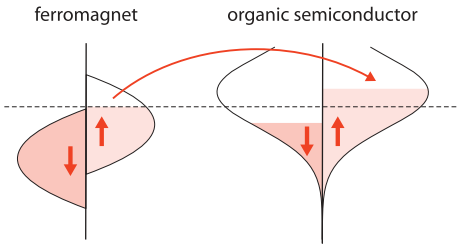

Figure 1.5: Density of states of a ferromagnet and a non-magnetic organic semiconductor, the selective injection of spin-up electrons from the ferromagnet results in a spin polarization in the non-magnetic material.

photon, a charge is excited from the HOMO to the LUMO, resulting in a singlet exciton. This exciton can either recombine (photoluminescence) or dissociate into free carriers, which drift in the electric field to the electrodes. Depending on the diffusion length of the excitons, the dissociation can occur in the bulk, at defect sites, or at the electrode.[8]

Conclusion

In conclusion, we have seen that charge transport in organic semiconductors occurs through hopping. Charges hop between localized sites that are disordered in position and energy. The charges are called polarons and can interact and form e–h pairs, excitons and bipolarons. The current in a typical organic device is limited by space charge, resulting in typical $J(V)$ characteristics.

1.2 Spintronics

Traditional electronics uses the charge of electrons to store or transport information, but by also using their spin, many new and exciting applications are available. Examples are magnetic-field sensors, non-volatile memory, and even applications such as quantum computing or 'race-track memory'.[25,118,140,146] One famous example of a spintronics application is the sensor in the read head of every modern hard disk; the development of which enabled the fast miniaturization and increase in storage density of hard disks in the last decades.[25] For the demonstration of giant magnetoresistance (GMR),[6,13] as is also used in the sensor in the hard disk, Fert and Grünberg received the Nobel Prize in Physics in 2007.

Many different spintronics applications have been developed. Here, we will describe the working of a spin valve to illustrate a typical example. For many of the other applications and related theory we refer to, for instance, Ref. 140. A spin valve consists of two ferromagnetic electrodes, separated by a non-magnetic spacer layer. In ferromagnetic materials, an imbalance exists between the spin-up and spin-down density of states at the Fermi level (Fig. 1.5). A current injected from the ferromagnetic electrode into the spacer layer will have an imbalance between the number of spin-up ($N_\uparrow$) and spin-down ($N_\downarrow$) electrons, resulting in a spin polarization,

$$P = \frac{N_\uparrow - N_\downarrow}{N_\uparrow + N_\downarrow}. \tag{1.3}$$

The spin polarization is transported by a spin-polarized current. During the transport

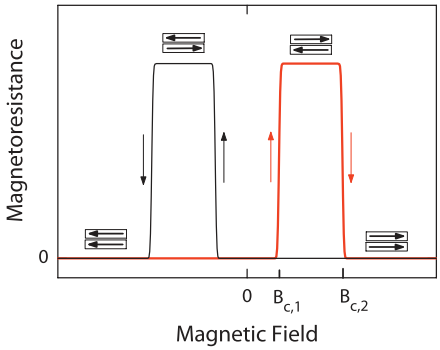

Figure 1.6: Schematic of MR(B) of spin valve, indicating the magnetization directions of the electrodes with the horizontal arrows. Both a forward (thick, red) and backward (thin, black) sweep are shown. The sweep direction is indicated by the vertical arrows. The magnetization directions switch at the indicated coercive fields.

to the other electrode, the spin polarization is gradually lost by spin flip events.[140] This loss typically follows an exponential decay that is characterized by a spin-diffusion length l_s. At the other electrode, depending on the relative orientation of the magnetization directions of the two electrodes, the spin polarization can have the same or the opposite sign. As a result, the device shows a smaller or larger resistance for parallel or anti-parallel alignment of the magnetization directions.

An illustration of the resistance of a spin valve as a function of the magnetic field B is shown in Fig. 1.6. At large negative B, the magnetization directions are aligned parallel (as indicated by the horizontal arrows), resulting in a low resistance. On increasing B beyond zero, the electrode with the smallest coercive field $B_{c,1}$ reverses its magnetization first, resulting in an anti-parallel alignment and a large resistance. Increasing B further also reverses the magnetization of the second electrode, returning the device in the low resistance state. Sweeping B back to a large negative value, again results in switching of the magnetization directions, with a corresponding step in resistance, but now at $-B_{c,1}$ and $-B_{c,2}$. The magnetoresistance is the relative change in resistance,

$$\mathrm{MR}(B) = \frac{R(B) - R_0}{R_0}, \tag{1.4}$$

with R_0 (usually) the resistance in the parallel case.

MR(B) curves similar to those for spin valves can also be obtained with magnetic tunnel junctions. In this case, we speak of tunnel magnetoresistance, TMR.[84] Instead of transporting carriers through the spacer layer, they tunnel through a thin tunnel barrier separating the two magnetic electrodes. As spin is conserved in a tunneling step, and the resistance of the barrier scales with the product of the density of states at both sides, a higher resistance is found in the anti-parallel case. This results in an MR(B) curve identical to the MR(B) curve of a spin valve as shown in Fig. 1.6. One of the differences between a spin valve and a tunnel junction is the possibility to manipulate the spins during transport in the spin valve. This is a property we will explore in Ch. 7.

For a properly working spin valve, an obvious requirement is that the spin-diffusion

length should be larger than or comparable to the thickness of the spacer layer. There are, however, many more conditions that affect its working. The efficiency of spin injection, for example, strongly depends on the details of the interface between the electrode and the spacer layer, and gradual switching of the magnetization directions can result in differently shaped curves, in particular when the coercive fields are not properly separated. Another possible issue is the reduction of MR by a 'conductivity mismatch'.[118,119] Significant spin injection is prevented by a conductivity mismatch when the resistivity of the material into which spins are injected is much larger than the resistivity of the ferromagnetic electrode (evaluated over a thickness of the order of the spin-flip length). This issue can be overcome by inserting a spin-dependent interface resistance, e.g., a tunnel barrier, like a thin oxide layer or a Schottky barrier.[118]

1.3 Organic spintronics

Organic spintronics deals with the electronic effects of spins in organic materials.[36,87,115] The use of organic materials for organic spintronics has attracted much attention because of the long spin lifetimes,[76,152] as significant spin–orbit coupling is negligible due to the low-weight atoms organic materials are composed of (spin–orbit coupling scales with Z^4, where Z is the atomic number). Moreover, the cheap and easy processing, and almost infinite chemical tunability make organic materials very appealing alternatives for the materials currently used in spintronics. One has to remark though that the long spin lifetime is accompanied by relatively small mobilities, but still is in a usable range.[36]

From an *inorganic* spintronics point of view, an obvious step is to replace the inorganic spacer layer in a spin valve with an organic material. There are, however, more applications of organic spintronics, like single molecule spintronics[109] and organic magnets,[73] but these will not be covered in this thesis. In addition, we note that is should be possible to enhance OLED efficiency by using spin polarized electrodes. With antiparallel alignment of the magnetization directions, 50% singlet excitons can be formed compared to 25% in a normal OLED.[10] However, no successful realization of this enhancement effect has been reported yet.[32,113]

A new spintronics effect, unique to disordered organic semiconductors, deals with the interaction and correlation of spins in organic semiconductors, leading to an organic magnetoresistance (OMAR). OMAR has gained much interest as it is an intrinsic effect observed in many (very different) organic materials. Because of the relatively large effects (up to 10–20%) at room temperature and small magnetic fields (10 mT), OMAR is very interesting for applications. For instance, magnetic functionality can be added to existing applications.[138] Moreover, it also offers new physics and a new handle to study processes in organic devices.

Spin transport in organic semiconductors and organic magnetoresistance seem to be two very different topics, but as we will see, they both depend on very similar spin-dependent processes and are thus interesting to study in parallel. First, in Sect. 1.3.1, a brief overview of recent experiments on spin transport in organic materials is given. Second, in Sect. 1.3.2, the key properties of OMAR are introduced and Sect. 1.3.3 describes the various models that have been suggested to explain the observed OMAR effects and discusses them in the light of recent experiments.

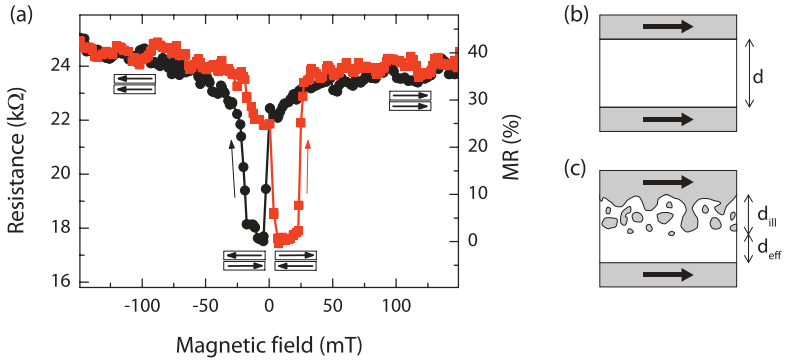

Figure 1.7: (a) First organic spin valve measurement by Xiong *et al.*, measured on a LSMO/Alq_3/Co device at 11 K. Forward sweep (squares, red) and backward sweep (circles, black) with parallel and anti-parallel magnetization directions illustrated. Data adapted from Ref. 149. (b) Ideal spin valve. (c) Spin valve with inclusions from the top electrode, resulting in an 'ill-defined' layer d_{ill}.

1.3.1 Spin transport in organic materials

Spin injection into a layer of a small molecule (sexithiophene), with two ferromagnetic $La_{0.67}Sr_{0.33}MnO_3$ (LSMO) electrodes, was first claimed in 2002.[35] However, no straightforward proof of correlation of the observed MR with the orientations of the magnetization directions was given. In 2004, Xiong *et al.* reported the first organic spin valve, using Alq_3 as the organic spacer layer and LSMO and Co as the electrodes.[149] Their measurement, shown in Fig. 1.7(a), is not a typical MR(B) curve as introduced in the previous section. Lower resistance was found in the anti-parallel configuration, which is believed to be from spin polarization opposite to the magnetization at interface.[36] Also, no sharp, but gradual switching was observed. Note, however, that also switching before zero was observed, which we believe to be a possible signature of magnetic-field dependence of the spin-diffusion length as will be covered in Ch. 6. The authors reported a spin-diffusion length of 45 nm, based on measurements on samples with variable spacer thickness measured at 11 K.[149] For this they did have to assume a significant 'ill-defined' layer of 87 nm, possibly from pinholes or Co inclusions in the spacer layer [Fig. 1.7(c)]. For increasing temperature, the MR strongly decreased, which was attributed to the temperature dependence of the LSMO electrode.[34] After this first report, several other groups reported on spin valves using organic spacer layers. The LSMO/Alq_3/Co spin valve was reproduced,[34,71,144,150] but also other materials have been tried, like polymers.[71,85] For an excellent overview we refer to Refs. 87 and 36, in which also other devices than spin valves are discussed.

Some controversy still exists about the experimental reports of organic spin valves. The main question is wether the observed MR is really the result from spin transport through the layer, or that it is from tunneling through thin regions.[59,139,150] One of the main arguments for tunneling is that the voltages at which results have been reported are well below the built-in voltage, but still the resistances are low, which is not a typical characteristic of organic devices.[59,139,150] In *inorganic* semiconductors, spin transport has been unambiguously demonstrated by manipulating the spins during transport, or

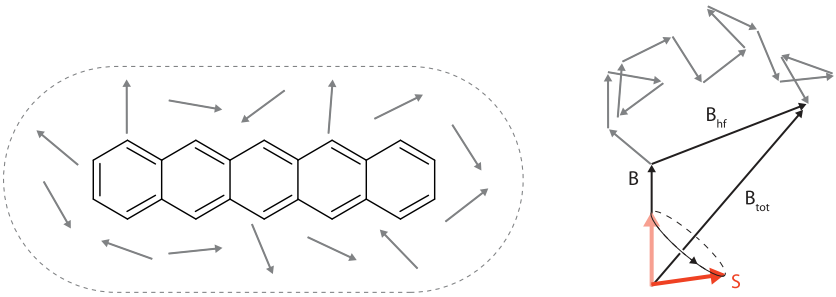

Figure 1.8: The spin S of a polaron on a pentacene molecule interacts with the hyperfine fields from the hydrogen nuclei (grey arrows). The polaron spin precesses around the sum of hyperfine fields from surrounding hydrogen nuclei and the external magnetic field. Figure adapted from Ref. 24.

optically measuring them at specific positions along the transport channel.[30,58,60,66] The optical route is not available in organic materials because of the low spin–orbit coupling.[115] The manipulation of spins during transport with a perpendicularly applied magnetic field—which is called a Hanle experiment—has not been reported yet for organic semiconductors. We believe that this is the crucial experiment that has to be performed on organic spin valves. Therefore, we model these experiments in Ch. 7. Recently, the profile of the spin distribution inside an organic layer was measured via two new approaches: two-photon photoemission spectroscopy and a muon spin-rotation technique.[27,40,137] Both these experiments involve rather complicated schemes to interpret the data.

One of the main questions regarding spin transport is about the origin of the spin-flip processes that determine the spin-diffusion length. Are they caused by the small, but finite, spin–orbit interactions, or do other processes dominate in organic materials? Inspired by the interpretation of OMAR (Sect. 1.3.3), we suggested that hyperfine fields could be the main source of spin relaxation, as will be discussed in full in Ch. 6. The hyperfine field that is sensed by the spin of a carrier originates from the surrounding hydrogen nuclei [Fig. 1.8]. The spin of the π-electrons couples indirectly to these nuclear spins through the interaction with the hydrogen s-electrons.[77] In addition, a dipole–dipole coupling between the spin of the π-electron and the nucleus is present. As the electron spin interacts with many neighboring nuclei, the total effect can be described by a classical hyperfine field on the order of a few millitesla.[121] After a spin is injected into the the organic layer, it will precess around the local hyperfine field. Because the hyperfine field is random at every site, this precession will change in a random direction between hops, causing a loss of spin polarization. In Ch. 6, we will show how this affects the spin-diffusion length and how an external field can reduce this loss.

Very recent experiments by Nguyen *et al.* confirmed the dominant role of hyperfine fields in determining the spin-diffusion length.[24,92] The authors used a PPV-derivative and replaced all relevant hydrogen with deuterium. Deuterium has more than a factor six smaller hyperfine constant, so a larger spin-diffusion length is expected if hyperfine interactions are the main source of loss of spin polarization. Indeed, when comparing spin valves using the hydrogenated and deuterated polymer, the latter showed a much

larger magnetoresistance and a spin-diffusion length of 49 nm (versus 16 nm). Moreover, the authors showed that MR(B) curves can be successfully fitted with the model we obtained based on hyperfine-field-induced spin relaxation (Ch. 6). In the same paper, the authors also experimentally confirmed the key role of the hyperfine fields for OMAR, as will be discussed in Sect. 1.3.3.

A remaining question is the role of the conductivity mismatch in organic spin valves.[59,119] Because the resistance of the organic layer is large compared to the electrode resistance, a significant reduction of MR could be expected. Experimentally, however, considerable MR has been observed. This suggests that the observed effects are either from tunneling through thin regions, or the analysis of conductivity mismatch is not directly applicable to organic semiconductors. It is indeed suggested[107] that this issue is not relevant for these materials, as an interfacial tunnel barrier—which is the standard solution to overcome conductivity mismatch—is naturally present due to hopping injection.[2]

A different approach to organic spin valves is using a very thin organic layer as a tunnel barrier, aiming for TMR. First results were, however, questionable, see the discussion in Ref. 36. A related approach that can also give information about spin transport is the use of a hybrid barrier: the combination of an inorganic tunnel barrier with a thin organic layer.[114,120,126,132,153] We used this approach to investigate the combination of an Al_2O_3 tunnel barrier of constant thickness with a thin Alq_3 layer of variable thickness.[120] At very small Alq_3 thickness, the charges tunnel through the combination of the two layer, while for thicker layers, they first hop to an intermediate site inside the Alq_3. At this onset of multi-step tunneling, we observed a change in the MR(B) that agreed well with a model where the spin of the carrier precesses in the random hyperfine field while at the site in the Alq_3.[120]

In conclusion, first steps have been made in using organic materials spin valves. However, it is still debated wether the observed MR is from transport or tunneling. This could be resolved by performing experiments in which manipulation of spins during transport is demonstrated.

1.3.2 Organic magnetoresistance effect

Magnetic field effects on the kinetics of chemical reactions and on the photoconductance and luminescence in organic solids have been studied intensively over the past decades, see for instance reviews in Refs. 129 and 55. However, only when considerable changes in the current on applying a magnetic field were reported,[43] much renewed interest was drawn. In this section, we briefly describe the main characteristic of this change in current, dubbed organic magnetoresistance (OMAR).

OMAR has now been shown in **many different materials**, from small molecules like Alq_3 to polymers like PPV [for structures, see Fig. 1.3(b)].[79] The observed relative change in current on applying a magnetic field B is generally quantified by the

magnetoconductance (MC):†

$$\mathrm{MC}(B) = \frac{I(B) - I_0}{I_0} = \frac{\Delta I}{I_0}, \tag{1.5}$$

with I_0 the current at $B = 0$ and, for small effects, $\mathrm{MC}(B) \approx -\mathrm{MR}(B)$ [Eq. 1.4]. Many groups have reported **large MC values** up to 10–20% at **small magnetic fields** of typically 10 mT, with in some cases much larger values.[154] Simultaneously, in addition to effects in the current,[11,16,39,70,79,96,143,154] similar effects were observed in the electroluminescence,[45,56,62,79,90,94,99,143,147] and photocurrent.[37,44,147] OMAR is observed at **room temperature** and low temperatures. Only weak temperature effects have been reported.[44,80] The observation at room temperature makes it very interesting for possible applications.[138]

For all the different materials, the $\mathrm{MC}(B)$ curves usually show a **typical shape**, see Fig. 1.9, which is found to be fitted well with either a Lorentzian,[79]

$$\mathrm{MC}(B) = \mathrm{MC}_\infty \frac{B^2}{B^2 + B_0^2}, \tag{1.6}$$

where MC_∞ is the MC at infinite magnetic field and B_0 is the half width at half maximum, or with an empirically found 'non-Lorentzian' function,

$$\mathrm{MC}(B) = \mathrm{MC}_\infty \frac{B^2}{(|B| + B_0)^2}, \tag{1.7}$$

where B_0 is the half width at quarter maximum. The non-Lorentzian line shape saturates notably slower (see fits in Fig. 1.9) and is the most commonly observed shape. Generally, a B_0 of 3–6 mT is found.[17,18,79,123,125] In Sect. 8.2, we will make suggestions for an alternative empirical function, which allows us to describe the transition from one shape to the other and which gives us additional information about the physics involved. In addition, by introducing a strong spin–orbit coupling, a larger B_0 was observed.[93,124]

In many cases the observed MC is positive, however also negative MC values have been observed. **Sign changes** have been observed as function of temperature,[16,18,79] voltage[11,16,38,79,122,148] and by modifying the injection efficiency of one of the carriers.[54] In Fig. 1.10 we show a typical measurement of the MC at a fixed magnetic field as a function of voltage. The effect starts negative, increases and changes sign, whereafter it has a maximum and then decreases. This shape of the $\mathrm{MC}(V)$ curve is commonly observed[5,17,95] (although not always starting negative) and will be discussed using different models in Sect. 1.3.4. Because it can give important information about OMAR, in Ch. 2 we introduce a new technique to quickly measure $\mathrm{MC}(V)$. We identified the point where the sign change occurs with the onset of efficient minority carrier injection.[16,17] This change was shown by a change in the power law fit of the $I(V)$ curve in combination with the onset of electroluminescence and with a change in capacitance.[17]

OMAR is believed to result from **effects in the bulk** of the device and not from

† In this thesis we will systematically use the magnetoconductance MC, because we measure the change in current. We will still call it the organic *magnetoresistance* effect, even though it is uncommon to use the resistance in devices with such a strong non-linear $I(V)$.

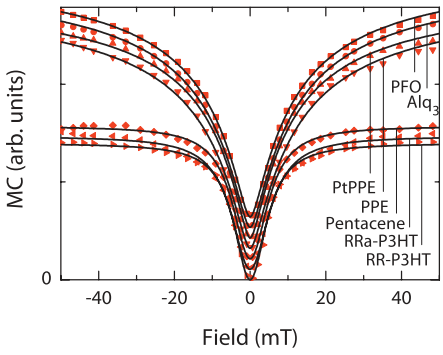

Figure 1.9: Normalized OMAR curves for different materials. The lines are fits with either a non-Lorentzian, Eq. 1.7 (PFO, Alq_3, PtPPE, PPE) or with a Lorentzian, Eq. 1.6 (Pentacene, RRA, RRE). The curves are vertically shifted. Data adapted from Ref. 79.

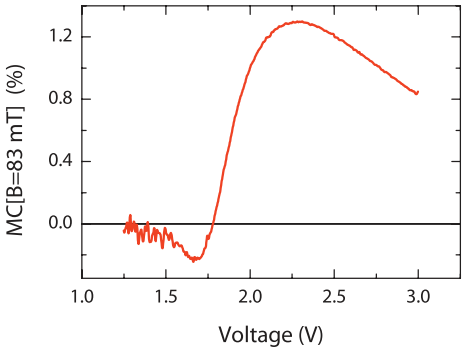

Figure 1.10: Magnetoconductance of a PPV based device as a function of voltage, measured at B = 83 mT with the technique described in Ch. 2.

injection. This was confirmed by measuring the same type of devices with different thicknesses, thereby decreasing the relative influence of the injection step.[79,98] It was found that the MC increased approximately linearly with thickness, thus ruling out a magnetic field dependent injection. The increase with thickness is an interesting effect, because it shows that a thicker device cannot be regarded as the sum of two thin devices, each with the same MC, because that would not result in an increase in MC. The origin of this has not yet been explained. Moreover, it is reported that OMAR is independent of the **orientation of the magnetic field** with respect to the sample.[11,43,47,154] However, in Ch. 4, we will show that a small change *can* be observed on changing the orientation.

By applying a relatively large current density for some time, called **conditioning**, the magnitude of the MC can be increased. Niedermeier *et al.* showed that, for PPV-based devices, the maximum MC increased from 1% to 15% on applying 1.25×10^3 A m^{-2} for 1 hour.[96] Smaller current densities also resulted in significant, but smaller, changes. Optical depletion of traps by illuminating the sample, or waiting several days, partly reversed the increase.[5] The increase is believed to result from the formation of traps.[5]

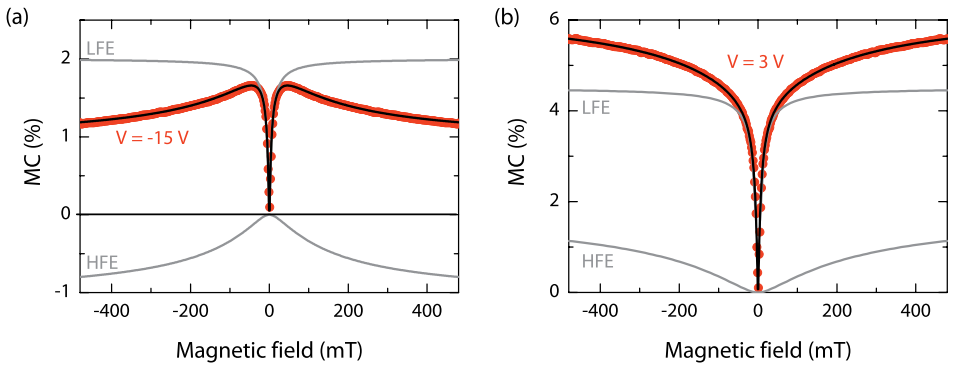

Figure 1.11: Measurement of the high-field effect (HFE) in the photocurrent of an Alq_3 device. The data are fitted using the sum two non-Lorentzians with different widths and magnitude (black lines). The HFE and low-field effect (LFE) contributions from the fits are also plotted separately (grey lines). (a) Large reverse bias results in $B_{0,\mathrm{LFE}} \approx 3\,\mathrm{mT}$ and $B_{0,\mathrm{HFE}} \approx 60\,\mathrm{mT}$. (b) Forward bias results in $B_{0,\mathrm{LFE}} \approx 3\,\mathrm{mT}$ and $B_{0,\mathrm{HFE}} \approx 117\,\mathrm{mT}$. [116]

This result is linked to the general observation that OMAR is larger in devices made with materials that show a large disorder.

In some cases, deviations from the 'standard' OMAR curves were reported at high magnetic fields. [33,65,70,133,143,151] Instead of a saturation of the MC at large fields, these **high-field effects** either show a continuous increase or decrease. Figure 1.11 shows an example of the MC in the photocurrent as a function of magnetic field for two different voltages. At large positive bias an increasing slope is present and at large reverse bias a negative slope. Wang *et al.* found high-field effects in the current to be absent in the electroluminescence and attributed the effect to a difference in g-factors of the electron and hole. [143] We believe the differences in g-factors needed to explain these effects are unrealistically large. Alternatively, we showed that these high-field effects might be better explained by interactions of triplet excitons with charges. [116]

Experiments have been performed on **single-carrier devices** and almost-single-carrier devices. [90,143] For these, a (negative) MC is found which is small compared to the MC in double-carrier devices using the same material. For single-carrier devices, the MC is also largest for the minority carrier. [90,143] In Sect. 1.3.4, we will compare these and other results to the models presented in Sect. 1.3.3.

1.3.3 Models for organic magnetoresistance

In this section, we introduce the main models that have been suggested in order to explain OMAR. In the next section, these will be compared to available results. Common models for magnetoresistance, like Lorentz force deflection, hopping magnetoresistance or effects like weak localization cannot explain the effect. [79,91] Alternative models are therefore needed. In all the models that have been proposed for OMAR, the correlation of the spins of interacting carriers and its dependence on the magnetic field play an essential role.

Many different models have been suggested for OMAR to explain the observed magnetic field effects in the current, electroluminescence, photocurrent, and fluorescence.

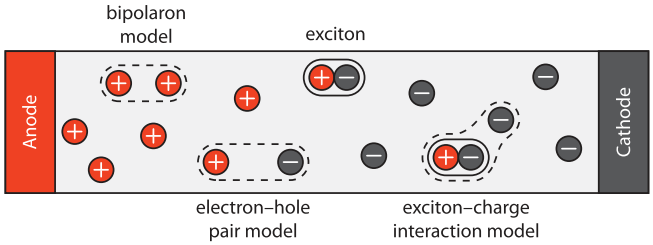

Figure 1.12: Illustration of the particle interactions that are considered in the different OMAR models. Figure adapted from Ref. 97.

Some of them show similarities. In this section, we will summarize the main groups of models to illustrate the different mechanisms that are believed to play a role. The models can be classified based on the pairs of particles that they consider for spin-dependent interactions. As illustrated in Fig. 1.12, these different particle pairs can be e–e pairs or h–h pairs as considered in the bipolaron model, e–h pairs as considered in the e–h pair models, and excitons and free or trapped charges as considered in the triplet–charge interaction model.

It is important to note that these spin-dependent interactions depend on the relative orientation of the spins and not on a net spin polarization. It is thus a dynamic process of spins that are in an out-of-thermal-equilibrium situation. The energy difference between the spin-up and spin-down states is negligible compared to the thermal energy.

Bipolaron model

First, we consider the bipolaron model.[20,141] Due to energetic and positional disorder, charge transport occurs via a limited number of percolation paths. On such paths, one carrier may be blocking the passage of another carrier. Depending on the spins of the two (identical) particles, a bipolaron can be formed as an intermediate state, subsequently allowing the carrier to pass. This is only possible if the spins of the two carriers are in a singlet configuration, as illustrated in Fig. 1.13(a). If they are in a triplet configuration, we speak of spin blocking, see Fig. 1.13(b). This can be lifted in the following way.

Even without an external magnetic field, the carriers still experience magnetic fields from the nearby hydrogen nuclei, the hyperfine fields. The total hyperfine field one carrier experiences is the sum of many random hyperfine fields (Fig. 1.8). As a result, two carriers will each experience a different total hyperfine field. In a magnetic field, spins will perform a precession. This precession changes the spin configuration of a pair because each experiences a different hyperfine field. Let us consider two spins, initially in a triplet configuration, see Fig. 1.13(c). Due to different precession of the spins, a singlet character will mix in, creating a finite chance to form a bipolaron, thus lifting the blocking.

On applying a large external magnetic field, the spins will precess around the sum of this field and the local hyperfine field, see Fig. 1.13(d). Because the hyperfine field is almost negligible, the spins experience approximately the same field. As a result, two

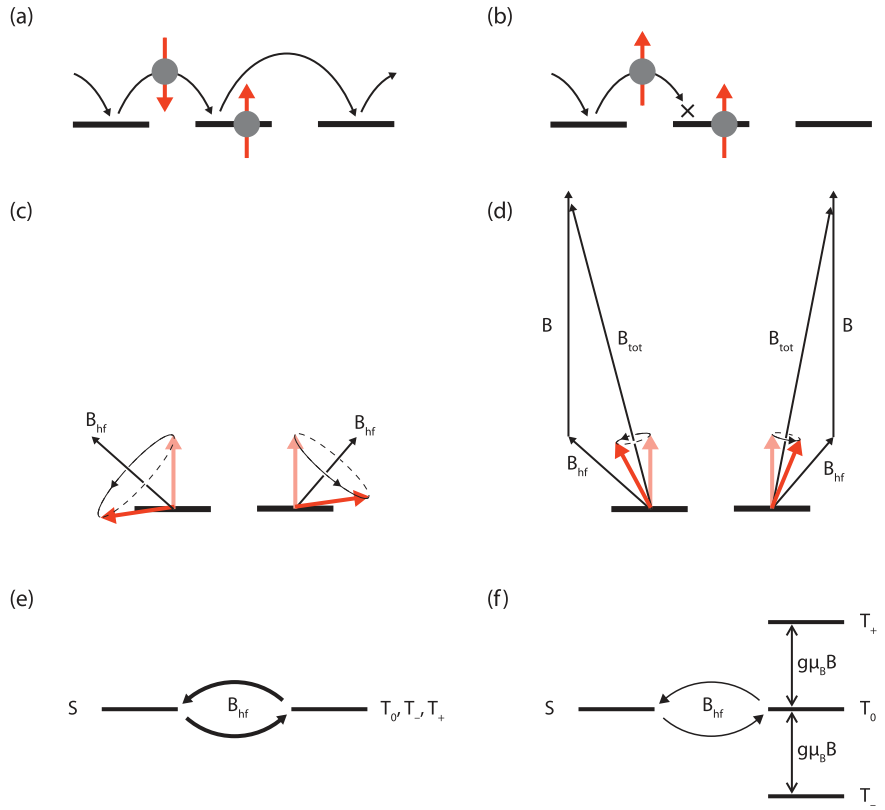

Figure 1.13: (a,b) Illustration of spin-blocking in bipolaron formation. Two particles with parallel spins cannot form an intermediate bipolaron. (c,d) Illustration of spin precession of two neighboring spins in (c) only the local hyperfine fields B_{hf} or (b) in the total field B_{tot} that is the sum of the local hyperfine field and the external field B. (e,f) Corresponding energy diagrams. (e) Without an external field, the hyperfine field mixes the singlet S and all three triples, T_+, T_0, and T_-. (f) An external field Zeeman splits the triplets. Mixing occurs only between S and T_0.

parallel spins will remain parallel and no mixing occurs. This can also be understood from considering the diagram of the energy levels of the total spin state of the two carriers, see Fig. 1.13(e,f). This consists of one singlet (S) and three triplet (T) states. At zero external field [Fig. 1.13(e)], S and all three triplets are degenerate in energy and are all mixed by the random hyperfine fields, allowing a large current to flow. However, on applying a large magnetic field the triplets split in energy [Fig. 1.13(f)]. As a consequence, no mixing is possible between S and T_+ and T_-, due to the Zeeman energy being larger than the hyperfine energy, resulting in a reduced current, so a negative MC.

According to the above reasoning, a decrease in bipolaron formation by applying a magnetic field results in a decrease in current and thus a negative MC. A positive MC is also possible as we will discuss below. Bobbert *et al.* investigated the bipolaron model using Monte Carlo simulations.[20] They looked at the current of charges on a grid of many sites with and without a magnetic field, explicitly including the possibility of bipolaron formation. With realistic parameters, indeed a finite MC was found. The

MC is generally negative, but a positive sign can be obtained when also including long range Coulomb repulsion. The *long range* Coulomb repulsion is believed to enhance bipolaron formation.[20] When more bipolarons are formed, there are less free carriers to carry a current. By applying a magnetic field, the number of bipolarons is decreased which gives a positive MC.

When a charge is blocked, it also has the possibility to take an alternative route, around the blocking site. How strongly it is forced to go through the blocking site is described by the branching ratio b. In both Monte Carlo simulations[20] and analytical calculations (Ch. 3), it was found that a small b gives a narrow MC(B) curve, corresponding to a Lorentzian [Eq. (1.6)]. For large b, the curves broaden and converge to a non-Lorentzian [Eq. (1.7)]. The experimentally found line shapes can thus be reproduced by the bipolaron model. One important requirement is that the spin precession occurs faster than the hopping of carriers, which we call 'slow hopping'. It was shown that this requirement is fulfilled in typical organic materials.

Whether it is energetically favorable to form a bipolaron depends on the energy gain from sharing the polaronic distortion and the energy loss from the Coulomb repulsion, the difference of which is U. In the Monte Carlo simulations, it was found that maximum MC is obtained when U is comparable to the disorder strength σ,[20] which is reasonable according to experiments.[53] We will comment on this result in Sect. 8.1. If the Coulomb repulsion is large compared to the gain from sharing the polaronic distortion, sites in the tail of the density of states or deeply trapped charges might play an important role. This could explain the larger MC observed in minority single-carrier devices,[143] and the increase when inducing traps by conditioning.[96] It could also explain why OMAR is generally larger in materials with a larger disorder, as in these materials there are relatively more sites with a site energy favorable for bipolaron formation.

Finally, we note that similar models were used to explain magnetic field effects found in double quantum dots in ^{13}C carbon nanotubes,[26] colloidal CdSe quantum dot films,[51] doped manganites,[1] and amorphous semiconductors.[86]

e–h pair model

For the other models, which are based on e–h pairs and excitons, it is useful to first discuss the diagram in Fig. 1.14. The diagram shows the different paths via which pairs of free polarons can recombine to the ground state. Free polarons (top) are first Coulombically bound as singlet and triplet e–h pairs with a ratio 1:3. These can recombine into excitons (with rates k_S and k_T) or dissociate back to free polarons (with rates q_S and q_T). Singlet and triplet e–h pairs can be mixed by the hyperfine fields, resulting in intersystem crossing with a rate m_{ISC}. The singlet and triplet excitons have a different energy due to the exchange interaction.

Several variations of the e–h model have been suggested.[4,11,44,56,62,75,99,105,106,125,147] Recombination of free polarons leads to a reduction of the current because this reduces the number of free carriers. In the e–h model the recombination (k) and/or dissociation (q) of e–h pairs are assumed different for singlet and triplets. Therefore, a change in the mixing of these pairs by a magnetic field results in a change in the current. The way the magnetic field reduces the mixing by the hyperfine fields is equivalent to the

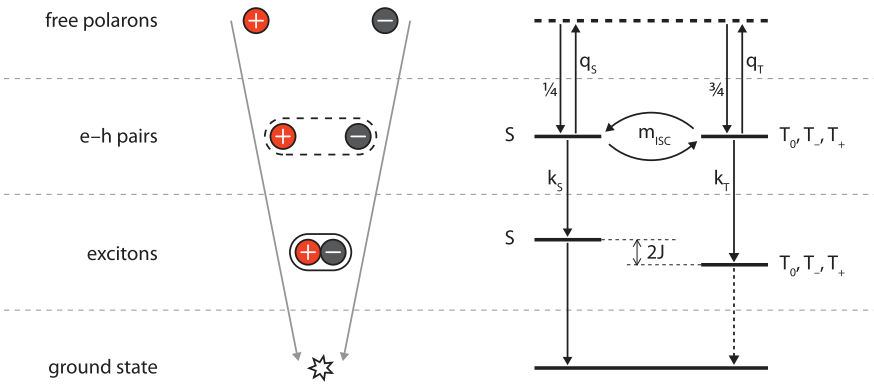

Figure 1.14: Diagram of possible routes for recombination of free electrons and holes to the ground state, by first forming an e–h pair which turn into an exciton. The different transitions are explained in the text. Figure adapted from Ref. 97.

reduction of mixing in the bipolaron model. Instead of mixing the total spin state of two equally charged polarons (e–e or h–h, see Fig. 1.13), the total spin state of an e–h pair is mixed.

By balancing the recombination and dissociation rates, Prigodin *et al.* derived a magnetic field dependent recombination rate, which was then linked to the recombination mobility μ_r, see Eq. (1.2).[11,106] The authors assumed that singlets have a larger recombination rate than triplets ($k_S > k_T$). The triplets then mostly contribute to dissociation. So, with less mixing due to B, there is less recombination. This reduction leads to more current and thus a positive MC. In addition, an attempt was made by the authors to explain a negative MC by introducing a regime where the current responds oppositely to a change in recombination.

Recently, Bagnich *et al.*[4] extended an early model explaining magnetic field effects on photocurrents, proposed in 1992 by Frankevich *et al.*[44] Bagnich *et al.*[4] explained the effects on injected charges by analyzing the magnetic-field dependence of the lifetimes of e–h pairs and their steady-state concentration. Similar arguments as made by Prigodin *et al.* were used; however, the formation of secondary charges from e–h dissociation was studied instead of the recombination rate. Bagnich *et al.* introduced one important requirement: the lifetime of the e–h pair should be larger than the time of spin evolution to allow for mixing.[4] This lifetime is expected to be reduced in a large electric field. The typical shape of MC(V), like in Fig. 1.10, was then explained as follows (except for the sign change). At low V, the effect of the electric field on the lifetime is negligible and only the increase of the number of e–h pairs with increasing V is relevant, leading to an increase in MC. At a certain voltage, the lifetime of e–h pairs becomes comparable to the time of spin evolution, resulting in a decrease in MC. The ratio of the singlet and triplet lifetimes, and the ratio of the singlet and triplet dissociation rates are both important model parameters. Depending on their values both positive and negative MCs are predicted. However, a voltage-dependent sign change would require a voltage dependence of one of the two ratios, which was not yet included.

For the e–h models, there are several requirements to make an effect possible. First,

there needs to be a significant dissociation of e–h pairs to see an effect on the free carriers. In e–h pairs, Coulomb attraction rapidly increases for decreasing separation. This suggests that only distant e–h pairs can play a role, because for more strongly bound e–h pairs recombination into an exciton seems inevitable. Second, an essential assumption is that either the recombination rate (k) of an e–h pair into an exciton is different for singlets and triplets, or the dissociation rate (q) to free carriers is different for singlets and triplets. Otherwise a change in e–h S:T ratio by reducing the mixing would have no effect. This requires a spin-state-dependent dissociation or recombination, which is not trivial as in an e–h pair the interaction between the two spins does not yet play a role.

Exciton–charge interaction model

Instead of considering the e–h pairs, Desai *et al.* considered the excitons.[37,39] Mostly triplet excitons are present due to their long lifetime (≈ 25 µs in Alq_3). An exciton can transfer its energy to a charge carrier on recombining to the ground state, called an exciton–charge interaction.[41] Desai *et al.* also considered a reduction of the mobility of the free carriers by scattering on the exciton (an intermediate state of the exciton–charge interaction).[39] The authors then suggested that a magnetic field acts on the intersystem crossing of singlet and triplet *excitons*, reducing the number of triplets in an applied field.[37,39] This would then give a reduced scattering of free charges on the triplets, thus a positive MC. A negative MC could result from dissociation of the excitons into free carriers by the charge interaction. However, the suggested magnetic-field dependence of the intersystem crossing between singlet and triplet excitons is highly unlikely as the energy splitting is very large (0.7 eV in Alq_3[28]) compared to the Zeeman splitting by a typical hyperfine field (0.5 µeV at 5 mT). We therefore consider the mixing of singlet and triplet *excitons* not to be applicable.

Exciton–charge interactions can play a role via a different route. The reaction itself is spin dependent as the total spin has to be conserved in the reaction.[41] Therefore, applying a magnetic field reduces the average triplet–charge interaction rate by Zeeman-splitting the energies of the particles. Different arguments lead to both a positive and a negative MC. The exciton charge interaction can detrap charges, thus increasing the current, resulting in a negative MC. However, in the reaction the triplet exciton is lost, so it cannot contribute to the current anymore via dissociation, which would result in a positive MC. The operating conditions determine which effect is strongest.[46] In addition to the hyperfine fields, the zero-field splitting parameters of the triplet exciton also play a role. These are caused by spin–spin interactions between the charges in the exciton, splitting the three triplet states in energy at zero field.[135] The zero-field splitting parameters determine the width of the magnetic field effect as they are larger than the hyperfine interactions (68 and 12 mT in Alq_3[29]). We have shown that similar, although broader, line shapes can be simulated.[116] For this we need to average over all different orientations because the zero-field splitting is anisotropic.

Hu *et al.* suggested the combination of two mechanisms to play a role: reduced mixing of e–h pairs giving a positive MC and exciton–charge reactions giving a negative MC.[55] For the e–h pairs, analogous to the e–h model, the authors suggested that singlet pairs have a larger dissociation rate because of their relatively stronger ionic

nature.[151] Besides the reduced mixing of e–h pairs, the authors also consider magnetic field effects on a spin-dependent formation of e–h pairs,[54] a view that is highly debated.[67] For the exciton–charge reactions, the release of trapped charges is considered, but also dissociation of the triplets by the reaction, which is believed to increase the current.

Hu *et al.* thus considered the total magnetic field effect to be a balance of e–h mixing (positive) and exciton–charge interaction (negative). The ratio can be changed by changing the charge balance or the electric field.[55] When the electrons and holes are unbalanced, the exciton–charge interactions dominate, resulting in a negative effect.[54] At high electric fields, the e–h pairs can dissociate more easily, resulting in a positive effect.[55]

Next to exciton–charge interactions, exciton–exciton interactions can also play a role. Two triplets can interact to form a ground state singlet and an excited singlet, which rapidly decays on emitting a photon, giving delayed fluorescence. This T–T annihilation is spin dependent and can be influenced by a magnetic field.[60,81] Like with exciton–charge interactions, the zero-field splitting parameters determine the field scale on which effects can be observed. In this case, the calculated line shapes are different from the ones discussed before and show a distinct feature around zero field due to level crossings.[116]

Summary of the OMAR models

Three groups of models have been introduced. First, in the bipolaron model, like charges can form an intermediate bipolaron if their total spin is in a singlet configuration. However, on applying a magnetic field, mixing of spin states by the hyperfine fields is suppressed, resulting in 'spin-blocking'. The basic model gives a negative MC, but it is also possible to explain a positive MC. Second, in the e–h model, the loss of free carriers by recombination is considered. The singlet and triplet e–h pairs that are formed in the recombination process are mixed by the hyperfine fields. A magnetic field suppresses this mixing, causing a positive MC because singlet e–h pairs are believed to either dissociate or recombine more easily than triplets. Third, in the exciton–charge interaction model, the effect of the magnetic field on this spin-dependent interaction is held responsible for the MC. A negative MC results from detrapping of charges. A positive MC could result from a loss of excitons by the interaction, making them unavailable for contributing to the current by dissociation. Triplet excitons dominate these effects as they have a longer lifetime than singlet excitons. From the three models, only the bipolaron model predicts the effect to be from like charges.

1.3.4 Comparison of OMAR models with experiments

In this section, we compare the proposed models with several of the experimental results. Many experiments on OMAR have been reported, but it can be difficult to compare between measurements. In several cases, only measurements at a single voltage are reported when changing parameters like temperature or thickness. As OMAR shows a significant voltage dependence (Fig. 1.10), this could unintentionally suppress effects, or suggest effects that are not real. In organic devices, changing only one parameter is very difficult because many processes are linked. Moreover, even with (almost) the same

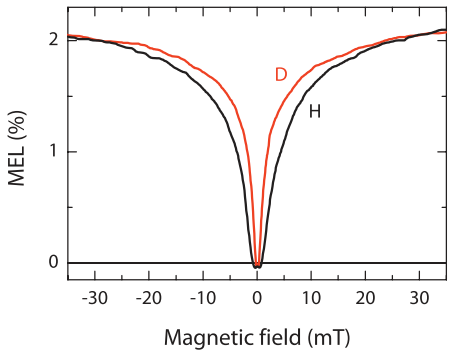

Figure 1.15: Relative change in electroluminescence on applying a magnetic field. Measurements for a PPV derivative with either hydrogen or deuterium at the backbone. Adapted from Ref. 92.

devices and materials, different magnitudes are reported.[97] This is to be expected as effects like conditioning and trapping play an important role. So, these differences could be the result of different material purity, fabrication procedures, and measurement history. For comparing the proposed models with experimental results, we will only focus on the main observations.

Hyperfine fields

Most models suggest that the suppression of the hyperfine-field induced mixing of spin states by a magnetic field is responsible for the observed changes in current and electroluminescence. The magnitude of the hyperfine fields then determines the width of the experimentally observed MC(B) curves. Very recently, this role of the hyperfine fields was confirmed by Nguyen *et al.* via experiments with a deuterated polymer (already introduced for spin valves in Sect. 1.3.1).[92] Not only did they observe an increased spin-diffusion length on replacing hydrogen with deuterium, also much narrower magneto-electroluminescence curves were obtained due to the much smaller hyperfine coupling constant for deuterium (Fig. 1.15).[92] This is the first direct proof that the competition between the hyperfine fields and the external field is indeed responsible for OMAR. It should be that a similar experiment was performed with Alq_3, which did not show any clear changes.[111] However, these measurements were performed at relatively large fields, while we expect the most notable changes at low fields.

Line shapes

OMAR shows a typical line shape, so the functions that were empirically found to fit the MC(B) curves (Fig. 1.9) might help identifying the correct model. However, for the bipolaron model and the e–h model similar, line shapes are expected because both can be evaluated in a similar way.[23] We confirmed this by performing calculations with an adapted Liouville equation,[116] as will also be discussed in Ch. 7. In these simulations, we found that a Lorentzian line shape is most dominant, as was also found by Sheng *et al.*[125] By tuning the relative rates, a broadening could be obtained. In particular, increasing the hopping rate relative to the precession rate decreased the magnitude but also broadened the curves.[116] In Ch. 3 we will show, for the bipolaron model, how

averaging over sets of parameters results in curves that can be fitted well with a non-Lorentzian. The role of the microscopic model on the broadening can be separated from the role of the hyperfine field. We do this by using the alternative function for the line shape, which we describe in Sect. 8.2. For the other models, using a similar Liouville equation resulted in similar curves.[116] By including effects like triplet–triplet annihilation also some of the high-field effects could be reproduced.

Single-carrier versus double-carrier devices

The most obvious test to discriminate between the bipolaron model and the other models is the measurement of OMAR in single-carrier devices. As the other models rely on the presence of e–h pairs or excitons, both electrons and holes are needed and no effect is expected in a single-carrier device. The bipolaron model, on the other hand, predicts an effect even in single-carrier devices. Wang *et al.* performed measurements on both hole-only and electron-only devices based on a PPV derivative.[143] In both devices a small negative MC was observed, which was smallest for the majority carriers. Nguyen *et al.* studied hole-only and electron-only Alq_3-based devices. No effect was found in the electron-only (majority) device while an MC was found in the hole-only (majority) device that was slightly smaller then in a double-carrier device.[90] These results seem to favor the bipolaron model. However, it is generally a question if there are really no opposite charges present. Some carriers might still be injected in the tails of the HOMO or LUMO, and there might be adjustments of the energy levels at the interface, lowering the expected injection barriers.

An elegant approach was recently proposed, where a doped silicon wafer was used to 'filter' the opposite carriers.[154] In single-carrier devices fabricated in this way, no clear magnetoconductance was reported.[154] Very small effects might, however, be missed by the way these samples were measured. Another indication for the requirement of e–h pairs could be that OMAR was reported to be correlated with the onset of light emission of the device,[39] but we found it also to be present before this onset.[17]

Nguyen *et al.* varied the work function of the electrodes by changing the electrode material.[90] They found the largest effects for well balanced double-carrier devices, and the effect decreased strongly on limiting the electron (majority) injection, suggesting an important role for e–h pairs. However, based on the observation of nearly equal effects in almost-hole-only devices and well-balanced devices, they concluded that OMAR is not an e–h pair effect as the number of e–h pairs is much smaller in these devices.[90]

In the bipolaron model, the presence of opposite charges might also play a role. The large Coulomb repulsion might be reduced by the interaction of the bipolaron with an oppositely charged polaron,[131] or a counter ion resulting from (un)intentional doping.[112] A bipolaron and an oppositely charged polaron can form a particle called a trion, which was recently experimentally observed in a PPV derivative.[61] This stabilization by opposite charges could be a different reason why, also in the bipolaron model, the largest OMAR effects are observed in well balanced double-carrier devices.[90] A different reason for the observation of large OMAR effects in double-carrier devices could be that there is only a significant effect on the minority carriers, which is communicated to the majority carriers via the space charge, as will be described below.[15]

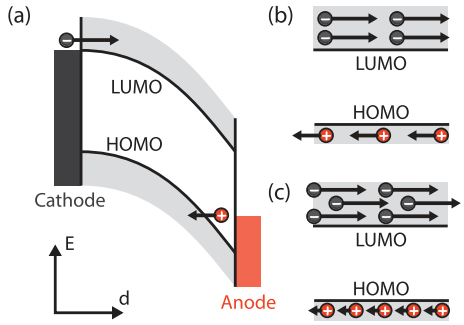

Figure 1.16: (a) Illustration of charge transport in a device with an Ohmic electron contact and an injection limited minority contact. (b,c) Decreasing the mobility of the holes (indicated by the length of the arrows) results in an increase in their density, allowing more electrons to be transported.

Sign changes

The sign of OMAR could give an important clue in validating the models. The e–h and exciton models primarily predict a positive MC, while in the bipolaron model a negative effect is straightforward and a positive effect needs further assumptions and is also smaller. In the experiments, the largest effects are positive.

Using a device model, we showed that even with *only negative effects* on the mobilities of electrons and holes a positive MC can be obtained.[15] Using this model, we could explain the observed sign changes and the MC(V) curves (an example was shown in Fig. 1.10). In short, these can be explained in the following way. We assume that the minority carriers are injection limited. So, a decrease in their mobility by the magnetic field mostly results in an increase of their density, Fig. 1.16. Via the space charge, this allows more majority carriers to be injected. Because these carry most of the current, an increase in current is observed, leading to a positive MC.

With this model, we can understand the MC(V) in Fig. 1.10 as follows. At low V, only electrons (majority) are efficiently injected, resulting in a negative MC. When holes (minority) start to be efficiently injected, the MC becomes positive via the mechanism described above. Here, we also use the experimental observation that the magnetic field effects in minority carriers are larger than in the majority carriers.[90,143] For larger V, the minority injection becomes less injection limited, resulting in a decrease of the positive MC. For large V, the MC is even expected to turn negative again. Two sign changes have not yet been observed in one device. However, in literature an opposite sign change at high voltage has been reported.[79] The negative effect can be strongly enhanced when traps are included in the calculations.[15] The first sign change is a superposition of two effects. If the effect in the majority carriers has a different width than the minority carriers, an anomalous line shape is expected. We observed such different widths for the negative and positive MC at low temperatures in Alq_3, in good agreement with this model.[16]

Hu *et al.* describe the observed sign changes with a balance of e–h mixing (positive MC) and exciton–charge interaction (negative MC).[55] In P3HT-based devices, they measured a magnetic-field dependence of the photocurrent that appeared to be a super-

position of a positive and a negative effect.[151] On mixing in a small amount (0–1%) of PCBM (an acceptor material), the positive effect disappeared and only a broad negative effect remained. The authors suggested that at these low concentrations only e–h pairs are effectively dissociated, resulting in only exciton–charge interactions.[151] For PCBM concentrations above 5%, also the negative effect disappeared, as then also the excitons were believed to be efficiently dissociated.[151]

The broader, negative signal is consistent with what would be expected based on the magnetic-field dependence of exciton–charge interactions.[116] Most of the sign changes reported in literature, however, do not show such a large difference in width between the positive and negative contribution. Therefore, we believe that in these other cases exciton–charge interactions cannot be responsible for the observed effects. Also in other experiments by Hu *et al.* where they observe a sign change on changing the charge balance in the devices, the width of the positive and negative effects is similar,[54] suggesting a different origin than exciton–charge reactions.

Singlet and triplet densities

The main concept in the e–h model is the interconversion between singlet and triplet e–h pairs. An applied magnetic field reduces this mixing and the concentration of triplets is thus expected to increase at the expense of the singlets. By studying both the luminescence and phosphorescence, Reufer *et al.* showed that these signals from singlets and triplets, respectively, did not change after stabilizing the e–h pairs in an electrical field for an extended time.[108] After this time, no interconversion was observed, which the authors attributed to a long-range exchange coupling in the e–h pair, resulting in a significant exchange splitting that prevents mixing. They showed that luminescence and phosphorescence both increase with applied magnetic field, contrary to what is predicted by the e–h models.

In the e–h model by Bagnich *et al.*, only a very small negative effect on the triplets concentration compared to a large positive change in the singlets was predicted.[4] Niedermeier[97] suggested this possible discrepancy could be explained by the polymer used in the experiments by Reufer *et al.*,[108] which incorporated (heavy) Pd atoms to allow phosphorescence from the triplets by locally inducing strong spin–orbit coupling. These atoms, however, have a very low concentration (1 in 1000 polymer repeat units) and their spin–orbit coupling is highly localized.[108]

Nguyen *et al.* separately measured the density of polarons, singlet excitons and triplet excitons.[89,91] They performed current-induced absorption spectroscopy in a magnetic field to measure changes in the optical transmission spectrum resulting from absorption by injected carriers and their recombination by-products for several different materials.[89,91] With this technique they separately measured the absorption by triplet excitons and polarons; in addition, they obtained a measure for the singlet excitons from the electroluminescence. Unlike the opposite change in singlet and triplet exciton density as predicted by the e–h models, both increased with magnetic field.[89,91] This is in agreement with the increase in electroluminescence and phosphorescence with field found by Reufer *et al.*[108] On analyzing the e–h models, Nguyen *et al.* predicted the effect on the current to be a higher order effect than in densities, so an effect of 10% in densities would only give a 1% effect in current.[91] They, however, observed

comparable changes in both. In the bipolaron model, the changes in mobility result in changes in the densities of the products, which all should show the same sign. [91] In the absorption experiments, no signal from bipolaron absorption was observed. However, no clear absorption of bipolarons is known. [91]

In the exciton–charge interaction models, the density of triplet excitons plays a crucial role. As the triplet exciton lifetime is strongly temperature dependent, [7] significant temperature-dependent changes in the MC should be observable, which is not the case. Except for recent experiments on high-field effects in the electroluminescence of an Alq_3 device at various temperatures. Liu *et al.* observed a wide negative high-field effect, which they believe results from T–T annihilation. [65] The effect was strongly reduced at higher temperatures, while the narrow positive contribution was almost unaffected. This experiment shows that triplet excitons will only play a marginal effect in room-temperature measurements. Moreover, via current-induced absorption spectroscopy Nguyen *et al.* showed a strong signal from triplet excitons at 10 K, which is absent at 200 K, while the OMAR effects are comparable at both temperatures. [91]

Conclusion

In conclusion, many different experiments have been performed, but no unambiguous evidence for one of the models has been found yet. The widely predicted role of the hyperfine fields has been established, but this does not exclude any of the models. The experimental results, in general, seem to favor a unipolar effect, like the bipolaron model. However, no direct proof of the existence and role of bipolarons has been found up to now. It is also not unlikely that multiple effects can play a role, for instance a combination of the e–h model with the bipolaron model. [143] Finally, a complete understanding of the mechanisms responsible for OMAR will not only be of relevance for the field of organic spintronics, but could also improve the understanding of the processes involved in organic electronics in general.

1.4 This thesis

The outline of this thesis is as follows. **Chapter 2** discusses the device fabrication and (new) measurements techniques. It demonstrates these techniques through an investigation of OMAR in the photocurrent. **Chapter 3** presents calculations on the bipolaron model using an analytical two-site model that is capable of reproducing both the typical line shapes and the sign changes. Measurements on OMAR are presented in the next two chapters: **Chapter 4** focuses on the frequency dependence and **Chapter 5** on the angle dependence. We show that the magnitude of OMAR is reduced when an oscillating magnetic field is used. Changing the angle of the magnetic field results in a small change in magnitude, which we attribute to anisotropic spin–spin interactions. **Chapter 6** presents a theory for spin diffusion in disordered organic semiconductors. In this model, the random hyperfine interactions are assumed to be the main cause of loss of spin information. **Chapter 7** extends the work in the previous chapter by theoretically investigating the influence of changing the orientation of the magnetic field with respect to the spin polarization. Experiments are simulated that could unambiguously demonstrate spin transport through the organic layer. **Chapter 8** discusses three extensions of the work presented in this thesis. The three topics are: extending the two-site

bipolaron model, using an alternative function for fitting the OMAR curves, and the effect of a spin-polarized current on OMAR. Finally, **Chapter 9** gives a more general outlook of the future of organic spintronics.

Measuring organic magnetoresistance

2

*This Chapter gives an introduction of the different measurement techniques used for measuring organic magnetoresistance (OMAR) in samples containing organic layers. In addition, the typical fabrication of such samples is discussed. New measurement techniques include the use of a modulation of the magnetic field to measure the derivative of the current to the magnetic field, which gives more accurate measurements and suppresses time-dependent changes in the current, and the use of fixed magnets to quickly measure the voltage dependence of OMAR. In addition to measuring the current resulting from charges injected by the electric field, we also illuminated the sample to photo-generate charges. To illustrate the measurement techniques, we present measurements of magnetoconductance (MC) in the photocurrent and the injected current in an Alq_3 based device. We use both a magnetic field modulation and a modulation of the intensity of the illumination to separate the contributions from the photocurrent and the injected current to the MC and show that these contributions cannot be combined, but should be treated separately.**

2.1 Introduction

Recently, a considerable magnetoresistance has been observed in devices using organic semiconducting materials; this effect is called organic magnetoresistance (OMAR), see Sect. 1.3.2. The unexpectedly large values, up to 10% at room temperature, make the effect both interesting for potential applications and a source of scientifically interesting questions. Next to the many experimental reports (see Sect. 1.3.2), several suggestions have been made for theoretical models, all based on the mixing of spins by the hydrogen hyperfine fields being suppressed by the applied field, see Sect. 1.3.3. The models are, however, based on different (combinations of) carriers. These models can be split into excitonic or electron–hole pair models,[11,106,147] an exciton–charge quenching model[39] and a bipolaron model.[20,141] Debate is still going on which model is

* Published as: *Separating photocurrent and injected current contributions to the organic magnetoresistance* W. Wagemans, W.J. Engelen, F.L. Bloom and B. Koopmans, Synth. Met. **160**, 266–270 (2010).

applicable; it has recently been suggested that some of the observed effects could even be explained by a combination of models.[143]

The shape of the OMAR versus magnetic field curves can give much information. The width of these curves is generally believed to be related to the total hydrogen hyperfine fields the carriers experience. By detailed fitting of the curves, combinations of multiple curves have been identified, sometimes with different signs, which can result in a sign change of the effect.[16–18,143] In all these cases detailed measurements are needed to capture these sometimes subtle effects. This is not straightforward as in many organic devices a time-dependent change in the current, also called drift, is observed when measuring at constant voltage, which could result from degradation or conditioning.[96,128] In a typical measurement, the magnetic field effects in the current are superimposed on the drift, requiring a correction before the OMAR effect can be studied. Several methods were used for this correction: performing a null measurement, i.e., averaging start and end points,[39,96] and using a Fourier transformation of the current while frequently switching on and off the magnetic field.[124] However, as the drift contribution is not linear in time, the line shape can be erroneously modified.

In the present work, we introduce a field modulation technique to measure OMAR, which successfully removes drift. In addition, we introduce a technique that allows us to quickly make detailed measurements of OMAR as a function of voltage. Finally, we use these techniques and an additional photocurrent modulation technique to separate the different OMAR contributions in the photocurrent and the injected current. Isolating the photo-generated charges is interesting as they start as singlets and thus could potentially be used to modify the S–T ratio in these devices, which is of relevance in the excitonic and e–h pair models (see Sect. 1.3.3).[11,106,147] So far most reports of OMAR in photocurrent focus on effects at zero or low bias,[37,110,151] while we use this technique to separately measure the influence of the photocurrent also at voltages where charges are electrically injected from the electrodes. This may answer the question if photo-generated charges add to the injected charges or if they should be treated separately.

2.2 Sample fabrication

For characterizing the different measurement techniques and to get the first results using a modulated photocurrent, we used typical OMAR samples containing the small molecule tris-(8-hydroxyquinoline) aluminum (Alq_3) as the active layer. As the anode, we used patterned indium tin oxide (ITO) on a glass substrate covered with poly(3,4-ethylenedioxythiophene): poly(styrenesulfonate) (PEDOT:PSS) spin coated from a dispersion (H.C. Starck), filtered using a 5 µm filter. The PEDOT:PSS serves to improve hole injection into the Alq_3. The Alq_3 (Sigma–Aldrich) layer was then thermally deposited in high vacuum system (~ 10^{-7} mbar) inside a nitrogen filled glove box. In another vacuum system within the same glove box, LiF and Al were subsequently evaporated as the cathode. The total junction stack thus consists of ITO/PEDOT:PSS(60 nm)/Alq_3(100 nm)/LiF(1 nm)/Al(100 nm), with a junction area of 3 mm × 3 mm.

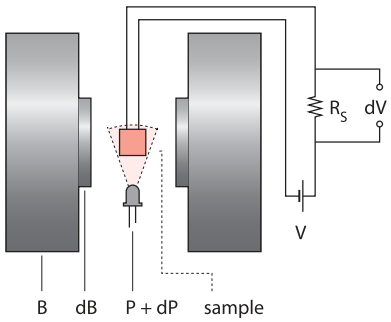

Figure 2.1: Setup used for the field modulation measurements. A DC magnetic field B and an AC magnetic field dB are applied by two separate sets of coils. The sample sits between the poles of the magnet and can also be illuminated by an LED with an intensity P and modulation dP. A voltage V is applied to the sample and the voltage over a series resistor R_S is measured with a lock-in amplifier in order to get the change in the current dI.

2.3 Setup

The samples were measured at room temperature in a cryostat that is attached to a glove box with a nitrogen atmosphere. The cryostat is suspended between the poles of an electromagnet with two sets of coils, one set is used to create a constant magnetic field B, the other set is used to add a small modulation dB (typically 0.5 mT), see Fig. 2.1. The field modulation has a frequency f_B, typically 27 Hz. This modulation is used to measure the derivative of the current with respect to the magnetic field (dI/dB). A voltage is applied to the sample with a Keithley 2400 source meter, which also records the current. Simultaneously, a lock-in amplifier records the voltage dV at the frequency f_B over a resistor R_S in series with the sample. Additionally, an LED (wavelength 400 nm), mounted close to the sample, can be used to illuminate the sample to create a photocurrent. The current which is sent through the LED has both a DC and an AC component, resulting in an intensity $P + \mathrm{d}P(f_P)$, with f_P typically 45 Hz and with a ratio $\mathrm{d}P/P = 1/3$. Here the modulation is used to separate and measure the part of the current affected by the illumination. This signal occurs at the frequency $f_B + f_P$.

A second setup is used to measure voltage dependent magnetoconductance data [MC(V)]. Usually, a fast way to obtain MC(V) is to perform two measurements of the current I as a function of voltage, with and without a (fixed) magnetic field B, and for each voltage calculate

$$\mathrm{MC}(B) = \frac{I(B) - I_0}{I_0} = \frac{\Delta I(B)}{I_0}, \tag{2.1}$$

with I_0 the current at $B = 0$. In these samples this is not reliable because of the time-dependent drift in the current. Alternatively, MC(V) can be obtained by repeatedly measuring MC(B) at a different constant voltage, which can be very time consuming and does not easily give a high voltage resolution. This is solved by measuring only at a few fixed fields while the voltage is varied, with little time between the different fields. For this, two permanent magnets are used that are mounted on the outside of a disk, see Fig. 2.2(a). The size of the magnets (20 mm × 20 mm) is chosen such that the field is homogenous over the junction area. The sample is placed under the disk, which is then

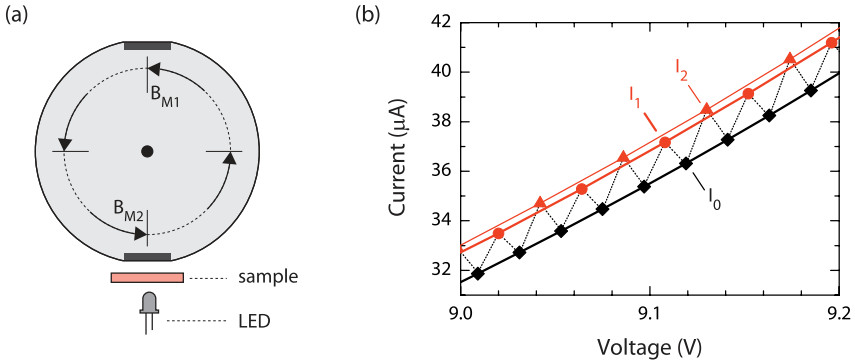

Figure 2.2: (a) Setup used for MC(V) measurements. The disk is rotated in quarter turns. The two permanent magnets B_{M1} and B_{M2} apply a magnetic field to the sample, which can also be illuminated with an LED with intensity P. (b) Resulting $I(V)$ data for four full rotations. I_1, I_2 and I_0 (lines) are extracted for B_{M1}, B_{M2} and zero field, respectively.

rotated between four positions using a stepper motor: two positions without a magnet ($B = 0$), and two positions with a magnet ($B_{M1} \approx 14$ mT and $B_{M2} \approx 83$ mT at the junction). The Keithley source meter is used to measure the current as a function of voltage and is programmed such that it triggers a quarter rotation of the disk after every applied voltage. In the obtained $I(V)$ data every other point is at $B = 0$, while the other points are alternately at either B_{M1} or B_{M2}, see Fig. 2.2(b). The current data is separated into three data sets (I_0, I_1 and I_2) and interpolated to all voltages. The magnetoconductance as a function of voltage is then calculated for both magnets: $\mathrm{MC}_n = (I_n - I_0)/I_0$, $n = 1, 2$. Finally, with this technique it is also possible to illuminate the sample with an LED (400 nm), making it easy to compare the voltage dependence of the total current including the photocurrent.

2.4 Field Modulation

With the addition of a small modulation dB to the magnetic field it is possible to measure the derivative of the current with respect to the magnetic field (dI/dB). To illustrate the dI/dB technique, we use a measurement of an Alq_3 sample at a voltage of 7 V. Figure 2.3(a) shows the current as a function of magnetic field as measured with the source meter. It is clear that the current is not symmetric around zero field, since a non-linear decrease in current with increasing time (which corresponds to increasing field) is superimposed on the typical OMAR curve. To remove this time-dependent change in current, simultaneously, the lock-in amplifier recorded the voltage over the series resistor R_S. This series resistor was chosen small compared to the resistance of the sample R ($R_S \approx 0.01R$). From the measured voltage, the change in current dI is calculated and divided by the modulation amplitude to get d$I(B)$/dB as plotted in Fig. 2.3(b). This is then integrated to get $\Delta I(B)$, which is vertically shifted so that $\Delta I(0) = 0$, resulting in MC(B) when divided by I_0, see Fig. 2.3(c). The fit shows a good agreement with the 'non-Lorentzian' line shape,[79]

$$\mathrm{MC}(B) = \mathrm{MC}_\infty \frac{B^2}{(B_0 + |B|)^2}, \tag{2.2}$$

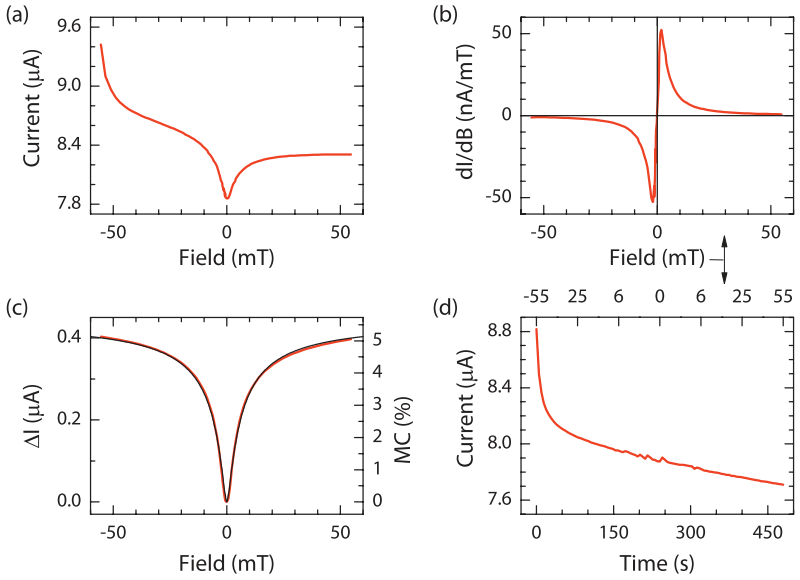

Figure 2.3: (a) $I(B)$ measured at 7 V. (b) $\mathrm{d}I/\mathrm{d}B$ simultaneously obtained with the lock-in amplifier, using a series resistor of 10 kΩ. (c) ΔI (red) fitted with non-Lorentzian (black) with B_0 = 2.9 mT and MC_∞ = 5.7%. (d) $I(t)$ obtained by subtracting ΔI from $I(B)$, note the non-linear field scale (top axis).

with B_0 the half width at quarter height, and MC_∞ the MC at infinite magnetic field. It should be noted that by using the field modulation, features smaller than the modulation amplitude will be suppressed and a small broadening of the curve will occur. We have simulated these effects and found the effects to be smaller than 1% for $\mathrm{d}B/B_0 = 0.1$. Sometimes, at very large junction resistances, the RC-time of the junction can become comparable to $1/f_B$, reducing the measured signal. Moreover, as we will show in Ch. 4, the transport in the device itself can have a frequency dependence, also resulting in a smaller signal.

The magnetic field independent part of the current I_0 can be recovered by subtracting $\Delta I(B)$ from $I(B)$. Figure 2.3(d) shows I_0 as a function of time. (It should be noted that more data points were taken around zero magnetic field; hence the non-linear field scale on the top axis.) The decrease in current is generally believed to be caused by degradation of the device, for instance by trap formation which leads to an increase in space charge.[128] Traps could be formed because for Alq_3 the cationic species are instable.[3] To calculate the MC, it would be logical to divide $\Delta I(B)$ by the $I_0(t)$ for the different fields. This, however, clearly does not give the right result as it reintroduces the time dependence which is almost absent in $\Delta I(B)$. Therefore, we choose to divide by $I(B = 0)$.

There is still a very small asymmetry in $\Delta I(B)$, but it is too small to clearly see in Fig. 2.3(c). This shows that while I_0 initially decreases rapidly in time, ΔI decreases much more slowly, and the time scale on which ΔI noticeably changes is smaller than the time for the measurement (~500 s). This has been confirmed by separate measure-

ments of $\mathrm{d}I/\mathrm{d}B$ as a function of time at a constant magnetic field, where the strong initial decrease is absent while a slow decrease remains, but slower than in I_0. This difference in decrease could be the reason why these type of samples can be 'conditioned', i.e., increasing the MC by applying a large current density for some time.[96] Because ΔI decreases slower in time than I_0, the MC will increase. This suggests that the processes responsible for OMAR are less affected by the degradation of the device. Thus, by better understanding the degradation processes occurring in these devices, it might be possible to exclude effects responsible for OMAR.

2.5 Photocurrent

Next, we discuss a study of the influence of illumination on the MC. Under illumination the current in these devices can be split in a current from electrically injected charges and photo-generated charges, respectively:

$$I = I_\mathrm{i} + I_\mathrm{p}. \tag{2.3}$$

The injected current has both a contribution due to leakage, which is dominant at low voltages, and a contribution from regular transport that starts around the built-in voltage.

To get a general idea about the voltage dependence of the MC with and without illumination, we used the rotating permanent magnets. Figure 2.4(a) shows $\mathrm{MC}_2(V)$ both with and without illumination. Without illumination, there are no magnetic field effects in the ohmic leakage current regime. The onset of MC occurs at 4.8 V and has a maximum of 8.4% at 6.5 V after which it decreases. When the sample is illuminated, the maximum shifts to 3.8 V, while the MC slightly decreases to 7.6%. At 1.4 V a sharp anomaly is observed where the MC diverges to $\pm\infty$. This is caused by the total current going through zero because the photocurrent and the leakage current are balanced, as can also be seen from the dip in the zero-field current with illumination $I_{0,P}$ in Fig. 2.4(b). The leakage current determines the zero crossing of $I_{0,P}$, while it has (almost) no influence on $\Delta I_{2,P}$. Therefore, the position of the zero crossing of $\Delta I_{2,P}$ at 1.6 V gives the voltage where the photocurrent is zero due to a flat band condition in the device, resulting in no electric field to move the photo-induced charges. At low voltages, the zero-field current without illumination $I_{0,P=0}$ shows an ohmic leakage current $\propto V^1$, which strongly increases at 4.8 V (with a power law $\propto V^{11}$). Fits to a power law are used to get an indication of the conduction mechanisms in different voltage regimes. To physically understand why a regime has a certain power law exponent is not trivial, but it has been shown that for instance space charge[101] and traps[14] can influence it. The correlation of the onset of MC with a change in power law is in agreement with previous observations,[16] although a negative MC is not observed. In contrast, $I_{0,P}$ with illumination shows a power law $\propto V^4$ at intermediate voltages which converges to the current without illumination for large voltages. When comparing the trend of $\Delta I_{2,P=0}$ and $I_{0,P=0}$ without illumination, there is a clear difference which explains the $\mathrm{MC}(V)$ behavior. The maximum in MC is observed when $\Delta I_{2,P=0}$ bends down to a power law of $\propto V^9$. For voltages above this point, a decrease in MC $\propto V^{-2}$ is thus observed. A similar comparison with illumination shows much less clear differences.

An advantage of this measurement technique is that it can also give information

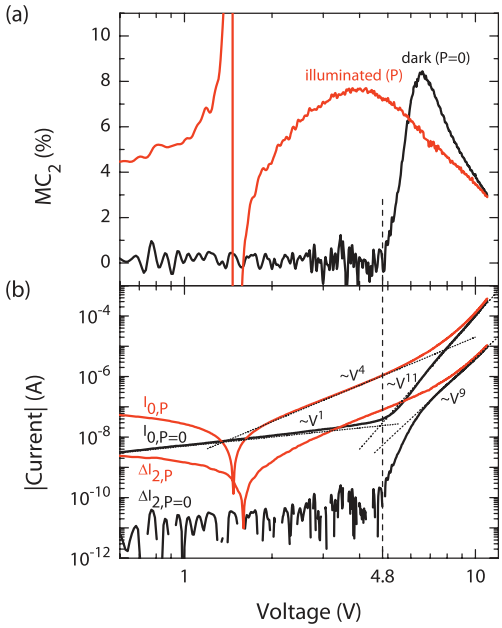

Figure 2.4: (a) $MC_2(V)$ (at 83 mT) with and without illumination. (b) Log–log plot of absolute values of I_0 and ΔI_2 as a function of voltage without (black lines) and with illumination P (red lines). Dotted lines indicate fits to different power laws as indicated.

about changes in the line shape if two different magnetic fields are used. If only the magnitude of the MC changes with voltage, the ratio MC_2/MC_1 will remain constant. If the curve also broadens, the ratio will increase. Moreover, if the line shape is non-Lorentzian, the parameters B_0 and MC_∞ can be solved. In Fig. 2.5(a), MC_2/MC_1 with illumination is plotted. As is indicated by the solid curve, a transition from large ratio to a smaller ratio is observed. For a non-Lorentzian, this corresponds to a narrowing of the curve. Below 1.6 V, the ratio is again smaller, but this might be caused by errors in the calculation due to the small current in this region.

To separate the contribution of the photocurrent from the injected current, we add a modulated illumination to our field modulation technique. First, we investigate the different ΔI that can be obtained with both these techniques. We compare three cases: (1) No photocurrent, $P = 0$: we measure $(\mathrm{d}I/\mathrm{d}B)|_{P=0}$, giving the injected current. (2) Constant photocurrent: we measure $(\mathrm{d}I/\mathrm{d}B)|_P$, giving the total current: both the injected and photocurrent. (3) Modulated photocurrent: we measure $(\mathrm{d}I/\mathrm{d}B)|_{P+\mathrm{d}P}$, giving only the photocurrent. At several voltages all three measurements were performed and the obtained data were processed and fitted to get ΔI at infinite magnetic field (Fig. 2.6), and B_0 [Fig. 2.5(b)]. We observe that the change in photocurrent dominates at low voltages and is equal to the injected current at 6.7 V after which the latter dominates. To validate the technique, also $(\mathrm{d}I/\mathrm{d}B)|_{P=0} + (\mathrm{d}I/\mathrm{d}B)|_{P+\mathrm{d}P}$ is plotted, which falls on top of the $(\mathrm{d}I/\mathrm{d}B)|_P$ data. This confirms that the photocurrent can be properly separated from the injected current.

A relevant question is whether the transport of the photo-generated charges and

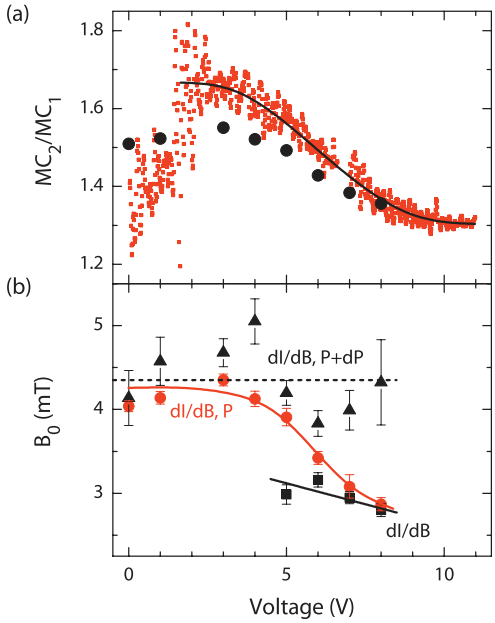

Figure 2.5: (a) Ratio MC_2/MC_1 as a function of voltage, the solid line is a guide to the eye. The large data points are the ratios calculated for the total current with illumination $(dI/dB)|_P$ from panel (b). (b) B_0 as a function of voltage obtained from fitting measurements for the three different cases: total current without illumination [$(dI/dB)|_{P=0}$, black squares], total current with illumination [$(dI/dB)|_P$, red], and photocurrent with modulated illumination [$(dI/dB)|_{P+dP}$, black triangles]. Lines are a guide to the eye.

the electrically injected charges can be treated in the same way or should be treated separately. In the first case, they would both show the same shape of $MC(B)$. Therefore, it is interesting to look at B_0 of the MC in the photocurrent and injected current separately in the region where they coexist. Figure 2.5(b) shows B_0 obtained for the three cases. With constant illumination, B_0 gradually decreases from 4.2 mT to 2.8 mT with increasing voltage, this widening is also visible from the two normalized ΔI curves obtained at 0 V and 8 V (inset Fig. 2.6). B_0 of the photocurrent, however, remains constant at 4.3 ± 0.3 mT, even while an injected current is present with a B_0 of 3.0 ± 0.2 mT. The trend in B_0 with constant illumination agrees well with the trend in the ratio shown in Fig. 2.5(b), and this agreement is even better shown by MC_2/MC_1 calculated for these data and plotted in Fig. 2.5(a) (large data points). The observation that B_0 of the photocurrent remains constant shows that the photocurrent does not just add to the total current, but that (part) of it is differently affected by the magnetic field.

Two different values for B_0 are observed simultaneously, suggesting two separate processes must be present: one which is dominated by the photocurrent, with a larger B_0, and one dominated by the injected current, with a smaller B_0. Our experiments do not yet give an answer to what these two processes could be. Previously, in Alq_3, effects with different B_0 have been reported.[18] In that case the different widths were assigned to different effects from electrons and holes, possibly by electrons and holes

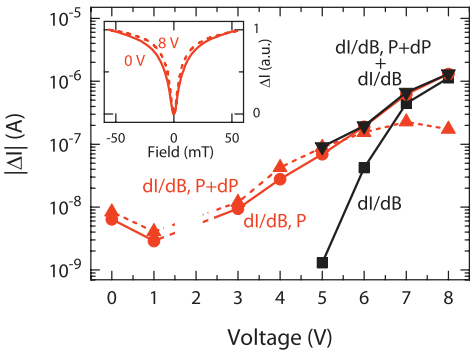

Figure 2.6: Absolute value of ΔI at infinite magnetic field as a function of voltage, obtained from fitting $\Delta I(B)$ measurements for three different cases: total current without illumination [$(\mathrm{d}I/\mathrm{d}B)|_{P=0}$, black squares], total current with illumination [$(\mathrm{d}I/\mathrm{d}B)|_{P}$, red circles], and photocurrent with modulated illumination [$(\mathrm{d}I/\mathrm{d}B)|_{P+\mathrm{d}P}$, red triangles]. The sum of $(\mathrm{d}I/\mathrm{d}B)|_{P=0}$ and $(\mathrm{d}I/\mathrm{d}B)|_{P+\mathrm{d}P}$ is also plotted (black triangles). The inset shows the normalized ΔI with illumination for 0 V and 8 V

experiencing a different hyperfine field. The width decreased when holes were injected and the devices became bipolar. This could suggest that, in our case, the injected current is dominated by holes, while the photocurrent is dominated by electrons, although no sign change is observed like in Ref. 110. Another suggestion could be that the photogenerated charges are more mobile from the excess energy after excitation (excitation with 3.1 eV compared to a HOMO–LUMO gap of 2.7 eV). In the bipolaron model, a change in the mobility could correspond to a different 'branching ratio' (see Sect. 1.3.3 and Ch. 3), which would result in a change in line width, even without a change in hyperfine fields. [20,141] It has recently been shown that the way in which the line shapes are found in the bipolaron model is also applicable to e–h pairs. [23] Finally, it could be speculated that different models are applicable to both currents. The effects in the photocurrent could be affected by excitonic effects since photo generated charges start as singlet excitons, while those in the injected current could be dominated by a different effect, like field dependent bipolaron formation. [20]

2.6 Conclusion

In conclusion, we have shown that we can remove the drift in the current by using a field-modulation technique to measure $\mathrm{d}I/\mathrm{d}B$. By measuring the MC at a few fixed magnetic fields we can quickly get a detailed picture of how the magnitude and the line width of the effect change as a function of voltage. Using these techniques, we confirm that the onset of MC occurs with the deviation from an ohmic behavior to a higher power law. Adding a photocurrent by illuminating the sample results in OMAR also at lower voltages. Combining the field modulation with an additional modulation of the illumination, we isolated the magnetic field effects on the photocurrent. We observed that the width of the MC(B) curve of the photocurrent remains constant with voltage and is larger than for the MC(B) curve observed with the electrically injected current, even when both currents are present.

A two-site bipolaron model for organic magnetoresistance

3

*The recently proposed bipolaron model for large 'organic magnetoresistance' (OMAR) at room temperature is extended to an analytically solvable two-site scheme. It is shown that even this extremely simplified approach reproduces some of the key features of OMAR, viz., the possibility to have both positive and negative magnetoresistance, as well as its universal line shapes. Specific behavior and limiting cases are discussed. Extensions of the model, to guide future experiments and numerical Monte Carlo studies, are suggested.**

3.1 Introduction

An entirely novel organic magnetoresistance (OMAR) phenomenon has started to puzzle the scientific community: magnetoresistance (MR) values up to 10% at room temperature and at fields of only a few millitesla have recently been reported in various organic materials, see Sect. 1.3.2. OMAR can be both positive and negative, and displays universal line shapes of approximately the same width B_0 for many small molecules and polymers. The magnetoconductance, $\mathrm{MC}(B) = [J(B) - J(0)]/J(0)$, where J is the current density and B is the applied field, is described by either a Lorentzian $B^2/(B_0^2 + B^2)$ or a specific non-Lorentzian $B^2/(|B|+B_0)^2$.[79] A number of models have been suggested to account for this intriguing behavior, see Sect. 1.3.3. One class of models assigns OMAR to spin-related excitonic effects.[39,106] Such a mechanism would only explain finite MC in double-carrier devices where both types of carriers are present. However, this interpretation is in conflict with reports that claim the observation of a finite OMAR in single-carrier devices, see Sect. 1.3.4.[79] Bobbert *et al.* proposed a *bipolaron model*[20] that does not rely on electron-hole recombination. A Monte Carlo scheme was implemented to describe hopping conductance on a large grid of molecular sites displaying energetic disorder. Thus, both positive and negative MC, as well as the particular line shapes, were reproduced.

*Published as: *A two-site bipolaron model for organic magnetoresistance* W. Wagemans, F.L. Bloom, P.A. Bobbert, M. Wohlgenannt, and B. Koopmans, J. Appl. Phys. 103, **07F303** (2008), with the addition of a clarification of the role of Coulomb repulsion and Figs. 3.2 and 3.5.

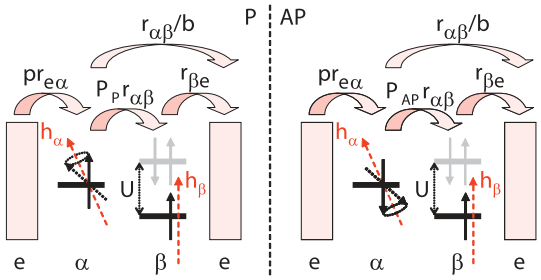

Figure 3.1: Schematic representation of the transport rates and electron spins in the P and AP configurations. The symbols are explained in the text.

In this chapter, we calculate the MC analytically by mapping the bipolaron model onto a model with two 'characteristic sites' with energies chosen out of a random distribution of molecular energy levels, a simplification which was already briefly outlined in Ref. 20. It will be shown that such an approach is sufficient to capture all the characteristics of OMAR in a qualitative way. We will successively discuss the basic ingredients of the bipolaron model, the definition of the two-site version of it, the derivation of the associated set of rate equations resulting in analytical expressions for $J(B)$, and, finally, the generic line shapes and the sign changes of OMAR. We conclude by suggesting possible extensions of the model.

3.2 Two-site bipolaron model

The key ingredient of the bipolaron model is the effect of an applied field on the probability of forming bipolarons (doubly occupied molecular sites). The formation of a bipolaron by hopping to a singly occupied site is only possible when the two electrons involved have a finite singlet component. Thus, two electrons on different sites, originally in a parallel (P) state, will have a lower probability to form a bipolaron than electrons in an antiparallel (AP) state—the notion of parallel and antiparallel refers to the orientation of the spin with respect to the local field axis. The restriction can be (partially) lifted by the presence of different local magnetic fields at the two sites. Then, the bipolaron formation probabilities for the two states ($P_{\mathrm{AP/P}}$) ($P_{\mathrm{AP/P}}$) scale with the time averaged singlet component of the two particle wave function, $P_{\mathrm{AP/P}} = \frac{1}{4}(1 \pm \hat{h}_1 \cdot \hat{h}_2)$, where the plus (minus) sign applies to the AP (P) orientation and $\hat{h}_i$ is a unit vector along the local magnetic field at site i.[20] The magnitude $B_0 \sim 5\,\mathrm{mT}$ observed in experiments supports the conjecture that the random field is the local hyperfine field ($\vec{B}_{\mathrm{hf},i}$) of hydrogen atoms surrounding the respective molecular sites i. At applied fields $B \gg |\vec{B}_{\mathrm{hf}}|$, the local fields are aligned: $\hat{h}_i \parallel \vec{B}$. In the Monte Carlo calculations of Ref. 20, the resulting MC was calculated as a function of temperature T and relevant model parameters, such as the energy difference U between the on-site Coulomb repulsion and the polaronic relaxation within a bipolaron state, the long-range Coulomb interaction V, and the Gaussian energy disorder strength σ.

In the present work, we select two neighboring critical sites, α and β, situated upstream and downstream with respect to the current, respectively, extending the approach of Ref. 20. The two sites are considered to be bottlenecks in the carrier transport

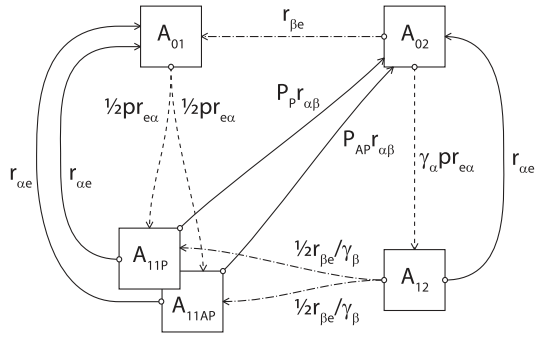

Figure 3.2: Rates to and from the many electron states A_{nm}, with n and m the occupation of site α and β, respectively. Using dashed, solid, and dash dotted arrows for hops from e, α, and β, respectively.

with α at most and β at least singly occupied, thereby strongly affecting the MC. To account for blocking effects to the current, it is crucial to work out the model in terms of many-electron states. Within the aforementioned restrictions and excluding time-reversed states (these are implicitly included in the occupation and rate parameters), we have five of them: $|01\rangle$, $|11_{\mathrm{P}}\rangle$, $|11_{\mathrm{AP}}\rangle$, $|02\rangle$, and $|12\rangle$, where $|nm\rangle$ denotes an $n(m)$-fold occupation at site α (β) and P/AP describes the spin orientation in case both sites are singly occupied. We consider only a downstream flow of electrons [Fig. 3.1]; from upstream in the environment e (not further specified in the model) to α at rate $pr_{e\to\alpha}$ (where p is a measure of the electron density in the environment), from site α to β at rate $P_{\mathrm{P/AP}}r_{\alpha\to\beta}$, and from site β to downstream e at rate $r_{\beta\to e}$. Furthermore, we introduce two routes that can release a blocking situation: (i) from site α bypassing β directly to the downstream environment, at a rate $r_{\alpha\to e} = r_{\alpha\to\beta}/b$, where b is the *branching ratio*, and (ii) a spin-orbit induced spin-flip process between states $|11_{\mathrm{P}}\rangle$ and $|11_{\mathrm{AP}}\rangle$ at a rate $r_{\alpha\to\beta}/a$, where a is the *spin flip coherence* ratio. Increasing a and b tends to make blocking effects more pronounced and thereby increases the MC. In addition, we can also include long-range Coulomb interaction by reducing the rate from the environment to site α with a factor γ_α (≤ 1) if site β is doubly occupied. Likewise, hopping from site β can be enhanced with a factor $1/\gamma_\beta$ (≥ 1) when site α is occupied.

Next, we define occupation probabilities A_{nm} for the respective many-electron states $|nm\rangle$, with $\sum_{nm} A_{nm} = 1$, and construct a set of rate equations from the rates illustrated in Fig. 3.2. In a stable solution, the time derivative of all probabilities should vanish. As an example, $dA_{11_P}/dt = 0$ yields

$$\begin{aligned} 0 = &\frac{1}{2}A_{01}pr_{e\to\alpha} + A_{11_{\mathrm{AP}}}r_{\alpha\to\beta}/a + \frac{1}{2}A_{12}r_{\beta\to e}/\gamma_\beta \\ &- A_{11_{\mathrm{P}}}(P_{\mathrm{P}}r_{\alpha\to\beta} + r_{\alpha\to\beta}/a + r_{\alpha\to\beta}/b), \end{aligned} \tag{3.1}$$

while the other equations can be constructed in a similar way. Solving the set of equations results in analytical expressions for A_{nm}. The current through the system equals the total rate from the upstream environment to α,

$$I/e = \langle (A_{01} + \gamma_\alpha A_{02}) \rangle \, pr_{e\to\alpha}, \tag{3.2}$$

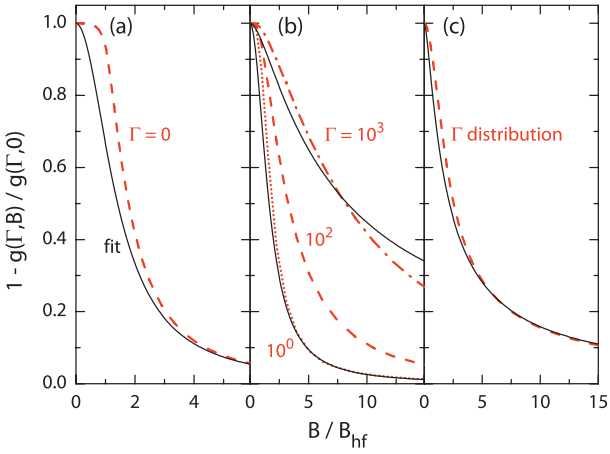

Figure 3.3: Modeled magnetic response for (a) $\Gamma = 0$, (b) $\Gamma = 10^0, 10^2, 10^3$ compared to a Lorentzian and non-Lorentzian fit, and (c) a Gaussian distribution of $\log \Gamma$ values, with average value $\log_{10} \Gamma = 1.4$ and half-width $\Delta \log_{10} \Gamma = 2.1$.

where $\langle \cdots \rangle$ denotes the ensemble average over $\vec{B}_{\mathrm{hf},i}$ and e is the electron charge. The explicit expression for I is lengthy but can be rewritten in a generic form,

$$I = I_\infty + I_B \left\langle 1 - \frac{1}{1 + \Gamma P_\mathrm{P} P_\mathrm{AP}} \right\rangle = I_\infty + I_B g\left(\Gamma, \frac{B}{B_\mathrm{hf}}\right), \tag{3.3}$$

where I_∞, I_B, and Γ are straightforward analytical expressions in terms of the model parameters, and B_hf is the hyperfine field scale. All field dependencies are described by the model function $g(\Gamma, B/B_\mathrm{hf})$; i.e., the line shape is fully described by a single parameter Γ, with $g(\Gamma, \infty) = 0$ and $g(\Gamma, 0) \to 1$ for $\Gamma \gg 1$ and $g(\Gamma, B) \propto \Gamma$ for $\Gamma \ll 1$. Thus, the shape and magnitude (including sign) of the OMAR are, respectively,

$$\begin{aligned} \frac{\mathrm{MC}(B)}{\mathrm{MC}(\infty)} &= 1 - \frac{g(\Gamma, B/B_\mathrm{hf})}{g(\Gamma, 0)}, \\ \mathrm{MC}(\infty) &= -\frac{I_B g(\Gamma, 0)}{I_\infty + I_B g(\Gamma, 0)}. \end{aligned} \tag{3.4}$$

3.3 Results

In order to calculate the line shape, it is required to specify the distribution of hyperfine fields. Assuming a fixed magnitude $|\vec{B}_{\mathrm{hf},i}| = B_\mathrm{hf}$ but a random orientation, it is possible to derive a (rather lengthy) analytical expression for $g(0, B/B_\mathrm{hf})$.[†] As illustrated in Fig. 3.3(a), at large B the function converges to a Lorentzian with width $B_0 = \sqrt{2} B_\mathrm{hf}$ and normalized to 1 at $B = 0$. However, a plateau up to around $B/B_\mathrm{hf} = 1$ is obtained using this averaging procedure. Numerical results for a more realistic average over a three dimensional Gaussian distribution of $\vec{B}_{\mathrm{hf},i}$ (defining $< |\vec{B}_{\mathrm{hf},i}| >= B_\mathrm{hf}$) are collected in

[†] $g(0,s) = \{16s^2[s^2+1][13s^2-3] - [s^2-1]^2[\log((s-1)^2) - \log((s+1)^2)][3\log((s-1)^2)(s^2-1)^2 - 3\log((s+1)^2)(s^2-1)^2 + 8s(3-5s^2)]\}/\{4096s^6\}$, with $s = B/B_\mathrm{hf}$.

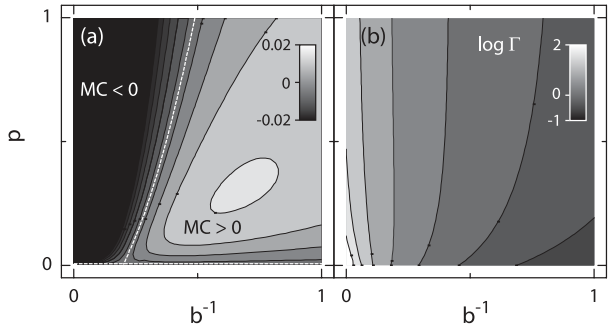

Figure 3.4: (a) Magnetoconductance MC(∞) as a function of b^{-1} and p for $r_{e\to\alpha} = r_{\alpha\to\beta} = 1$, $r_{\beta\to e} = 0.1$, $\gamma_\alpha = \gamma_\beta = 0.5$, and $a^{-1} = 0$. The dashed lines indicate MC= 0, where the transition from negative to positive magnetoconductance occurs. (b) log Γ as a function of b^{-1} and p.

Fig. 3.3(b) for several values of Γ. It is found that MR(B) broadens as a function of Γ and resembles a Lorentzian reasonably well for small Γ, while for large Γ a reasonable agreement with the empirical non-Lorentzian line shape (as seen in many of the experiments) is obtained. Nevertheless, it is not possible to achieve a perfect agreement for large fields in the latter case. In order to link the shape parameter Γ to the model parameters, we first consider analytical results in lowest order of p, i.e., a low electron density,

$$\Gamma = 2/\left[a^{-1} + b^{-1} + 4(ab)^{-1} + 2b^{-2}\right]. \tag{3.5}$$

Thus, it is found that reducing b^{-1}—which corresponds to enhancing bipolaron formation—broadens the MC(B). This means that higher magnetic fields are required to quench the bipolaron formation and to saturate the MC, in agreement with the full Monte Carlo calculations.[20] A similar trend is found for lowering a^{-1}. For general values of p, an example of Γ as a function of both p and b^{-1} (and setting $a^{-1} = 0$) is displayed in Fig. 3.4(b).

In order to calculate the magnitude of OMAR, MC(∞), one can follow two routes. Treating Eq. (3.4) in an exact way requires the numerical evaluation of $g(\Gamma, 0)$. Alternatively, one can average over a discrete number of orientations, rather than integrate over all orientations of $\vec{B}_{\mathrm{hf},i}$ at the two sites. As an example of such a calculation, MC(∞) is plotted as a function of p and b^{-1} in Fig. 3.4(a). Interestingly, it is found that *even this extremely simple model reproduces both positive and negative MC*. As a general trend, at a large branching ratio (small b^{-1}), a negative MC is obtained, as expected according to the 'blocking mechanism'. Actually, one can show analytically that MC(∞) = –1 for $a^{-1} = b^{-1} = 0$, i.e., a fully blocked situation. As will be discussed in more detail below, for certain parameters, the bipolaron model also predicts a positive MC. In the two-site model, this situation can occur once some of the rates r or the density of polarons in the environment p are assumed to be a function of the occupation of the β site. In our model, we chose the first option by introducing γ to modify some of the rates. Doing so, at a smaller branching ratio (large b^{-1}) and for $\gamma_\alpha < 1$, a sign change to a positive MC is witnessed. For $\gamma_\alpha = 1$, only a negative MC is observed, while for decreasing γ_α, so for en-

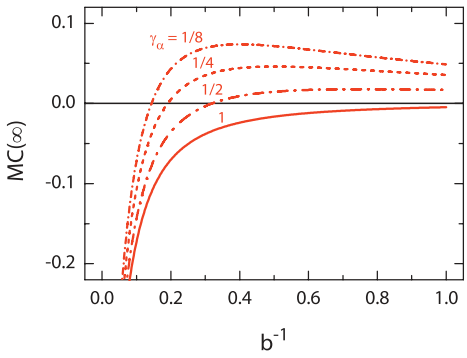

Figure 3.5: Magnetoconductance MC(∞) as a function of b^{-1} with different γ_α for $\gamma_\beta = 1$ and $p = 0.5$, while the other parameters are the same as in Fig. 3.4.

hanced repulsion of a double charge at site β, the positive MC becomes larger [Fig. 3.5]. Within the two-site model, positive MC is a consequence of a reduction of the current by a doubly occupied β site. In organic devices, such a situation can occur when the total polaron density increases at the expense of the bipolaron population at increasing B, as explored further in the full Monte Carlo calculations.[20] Interestingly, the line separating negative and positive MC is given by a simple expression (for $\gamma_\alpha = \gamma_\beta = 0.5$, and arbitrary a),

$$p = \left(b^{-2} r_{\alpha\to\beta}^2 - 4 r_{\beta\to e}^2\right) / \left(2 r_{e\to\alpha} r_{\beta\to e}\right). \tag{3.6}$$

Thus, although the inclusion of spin-flip scattering (finite a) decreases the magnitude of the MC, the sign of MC is totally independent of a. Moreover, we found that Eq. (3.6) is unaffected by details of the $\vec{B}_{\mathrm{hf},i}$ distribution. We note that the magnitude of the positive MC is generally smaller than the negative MC, making the negative MC the more dominant result of the bipolaron mechanism.

Comparing MC(∞) and Γ [Figs. 3.4(a) and 3.4(b), respectively], a one-to-one relation is found to be absent. However, there is some trend that the positive MC has a larger width (Γ). It would be challenging to unambiguously correlate this outcome with experiments. Actually, in recent experiments on Alq_3 devices we measured a trend that upon a transition from positive to negative MC, B_0 is significantly increased.[16] However, care has to be taken in drawing too strong conclusions from experiments on a single system.

Finally, we sketch a number of extensions of the present work that could lead to a closer agreement with the Monte Carlo studies and maybe even provide predictive power with respect to experiments. First of all, the rate parameters within our model as well as p, a, and b should be expressed in terms of the more generic system parameters (U, V, σ, E_F), electrical bias, and temperature (preliminary results and an outlook of this approach will be given in Sect. 8.1). Second, rather than specifying two levels with fixed rate parameters, it might be necessary to model an ensemble of two-level systems with different relative energy alignments. As one of the outcomes, the final line shape would not be defined by a single Γ but rather be described by a distribution of values. Doing so in an *ad hoc* way, we found this to be a promising route. As an ex-

ample, Fig. 3.3(c) displays the line shape resulting from a distribution of Γ. This way, contrary to using a single component [Fig. 3.3(b)], perfect agreement is achieved with the phenomenological non-Lorentzian line shape (as also reproduced by Monte Carlo calculations) and up to large B.

3.4 Conclusion

Concluding, we have introduced a simple two-site bipolaron model that reproduces the main features of OMAR, viz., the occurrence of sign changes and the characteristic line shapes. By producing simple analytical expressions, the approach could be valuable in guiding further numerical (Monte Carlo) and experimental efforts aimed at improving our understanding of this new phenomenon.

Frequency dependence of organic magnetoresistance

4

*In this Chapter, the frequency dependence of organic magnetoresistance (OMAR) is investigated. By this, we aim to identify the processes involved in OMAR by their frequency characteristics. Doing so, we ultimately hope to be able to distinguish between the different models proposed for OMAR, because the processes that are used in the models each occur on different timescales. We use a superposition of an AC and DC magnetic field and show that the measured magnetoconductance decreases when the frequency of the AC component is increased. The decrease is stronger for lower voltages, which is shown to be linked to the presence of a negative capacitance (as measured with admittance spectroscopy). The negative capacitance disappears when the frequency becomes comparable to the inverse transition time of the minority carriers. We show that these results are in agreement with recent interpretations of magnetic field effects in minority carrier mobility being the dominant effect.**

4.1 Introduction

As introduced in Sect. 1.3.3, several models have been proposed for the organic magnetoresistance (OMAR) effect, but the exact origin of the effect is still debated. In organic devices, many processes can occur which could have an effect on OMAR, each with a characteristic timescale. For instance, triplet (T) excitons could play a role in T–T annihilation or in reactions with charges,[55] and these excitons have a typical lifetime of 25 µs in Alq_3.[7] Traps have been suggested to enhance the MC, for instance via space charge effects[15] and by conditioning the devices.[5] Traps in the devices have a typical detrapping time from less than milliseconds up to hours, depending on how deep the traps are. Another typical timescale is the transit time, which is directly linked to the mobilities of the carriers, $\tau = L^2/\mu V$, with L the thickness, μ the mobility, and V the voltage.[49,74] Note that τ is usually different for electrons and holes due to the different mobilities. If we would be able to perform measurements of OMAR on any of these

*In preparation: *Frequency dependence of organic magnetoresistance* W. Wagemans, P. Janssen, E.H.M. van der Heijden, M. Kemerink, and B. Koopmans.

timescales, we might be able to obtain clues about the processes relevant for OMAR, and thus discriminate between the proposed models.

In literature, only a few experimental reports on OMAR are available where the frequency of the applied magnetic field plays a role. Veeraraghaven *et al.* reported no significant change in the response to an AC magnetic field for frequencies up to 100 kHz, for which they used a current density of 10 A m^{-2}.[138] On the other hand a slow step response on the order of seconds was reported by Meruvia *et al.*, which they suggested to be caused by the magnetic field acting on the trapping times.[82] Finally, Majumdar *et al.* recently showed that the OMAR they measure increases when the rate at which B is swept is decreased, which they conjecture could be caused by traps.[69]

In this chapter we will show that the measured OMAR is sensitive to the frequency of the AC-component of the applied magnetic field. By comparing the frequency-dependent OMAR measurements with admittance spectroscopy, we relate the disappearance of OMAR to the transit times of the minority carriers. Finally, we discuss the consequences of these observations for the models suggested for OMAR.

4.2 Methods

We present experimental results on tris-(8-hydroxyquinoline) aluminum (Alq_3) based devices, but we note that we observed similar effects with poly[2-methoxy-5-(3',7'-dimethyloctyloxy)-1,4-phenylene vinylene] (MDMO-PPV). The devices have the structure ITO/PEDOT:PSS(60 nm)/Alq_3(100 nm)/LiF(1 nm)/Al(100 nm). See Sect. 2.2 for details on the used materials and fabrication. Magnetic measurements were performed with an air coil through which a current with both an AC and DC component was sent. The AC response was measured with a lock-in amplifier over a resistor in series with the sample, while a constant voltage was applied, see also Sect. 2.4.[142] Admittance spectroscopy measurements were performed with a Solartron SI 1260 impedance analyzer.

4.3 Results

We measured the frequency dependence of the MC at different voltages, starting from a voltage just above the onset of OMAR. Plotted in Fig. 4.1(a) is the change in current through the sample due to a change in magnetic field (dI/dB), divided by the DC current and normalized at 1 Hz. dI/dB is the derivative of the current with respect to the magnetic field [inset Fig. 4.1(a)], which, when integrated, gives a typical OMAR curve (Sect. 2.4).[142] Here, however, we do not measure a full field sweep, but divide the signal at a fixed B by the current to get a measure for the MC, dMC/dB. It was validated that the shape of the curves does not change with frequency, justifying this approach. To remove any extra signal from induction, picked up by the wires at higher frequencies, we measure the difference in signal at 2 mT and −2 mT, where dI/dB has an opposite sign.

For all measured voltages, the MC decreases with increasing frequency, see Fig. 4.1(a). At low voltages, the MC decreases faster than at higher voltages. The voltage dependence of the MC at fixed frequencies, extracted from Fig. 4.1(a), is shown in Fig. 4.1(b). At low frequencies, a typical MC(V) curve is obtained, which first increases with increasing voltage, has a maximum and then slowly decreases. For increasing frequency, the MC(V) curve collapses, with the strongest reduction at low voltages. Also plotted is

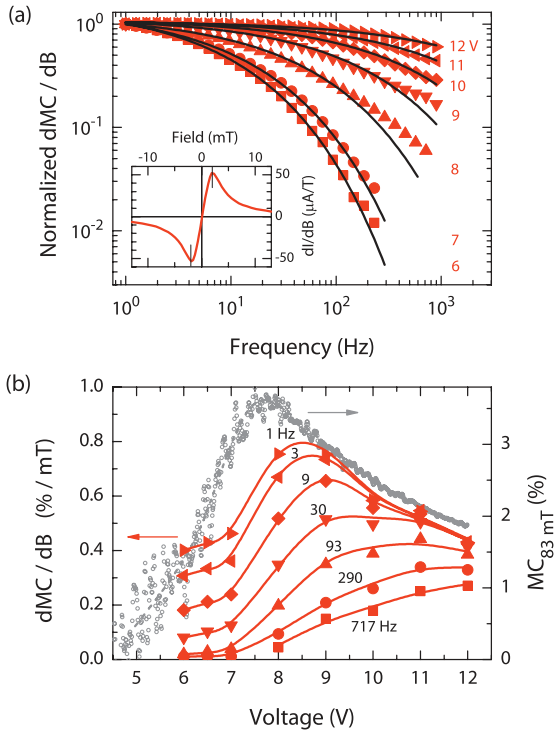

Figure 4.1: (a) dMC/dB, normalized at 1 Hz, as a function of frequency for different voltages, using dB = 0.5 mT and B = ±2 mT. The lines are a fit to a stretched exponential. Inset: dI/dB at 10 V, 120 Hz, corrected for offset. (b) dMC/dB as a function of voltage for different frequencies (left axis) and MC as a function of voltage for B = 83 mT, measured with a permanent magnet (small symbols, right axis).

the MC measured using a permanent magnet [142] (dashed line, right axis), which can be considered as a measurement at $f \approx 0$ Hz. This curve fits the extrapolation of the trend in the curves from 717 to 1 Hz, except for the two lowest voltages.

In addition to the response of the current to an AC magnetic field, we measured the response to an AC voltage, which is the admittance,

$$Y = \mathrm{d}I/\mathrm{d}V = G + i\omega C, \tag{4.1}$$

where the real part, G, is the conductance, and the complex, out-of-phase, part is the angular frequency $\omega = 2\pi f$ times the capacitance C. Below 7 V, a decreasing capacitance as a function of frequency is observed, while for $V \geq 7$ V, the capacitance starts negative and then converges to the low voltage signal, Fig. 4.2(a). For increasing voltage, this negative contribution to the capacitance is more pronounced.

Interestingly, the absence of a negative contribution to the capacitance seems to be correlated to the suppression of the MC. To get a quantitative measure, we fit the frequency dependence of the MC with a stretched exponential, $\propto \exp[-(f/f_0)^d]$, where f_0 is a characteristic frequency and $d = 0.46$ is a stretching parameter that is kept the same for all curves [lines in Fig. 4.1(a)]. In Fig. 4.3, both f_0 and the frequencies where

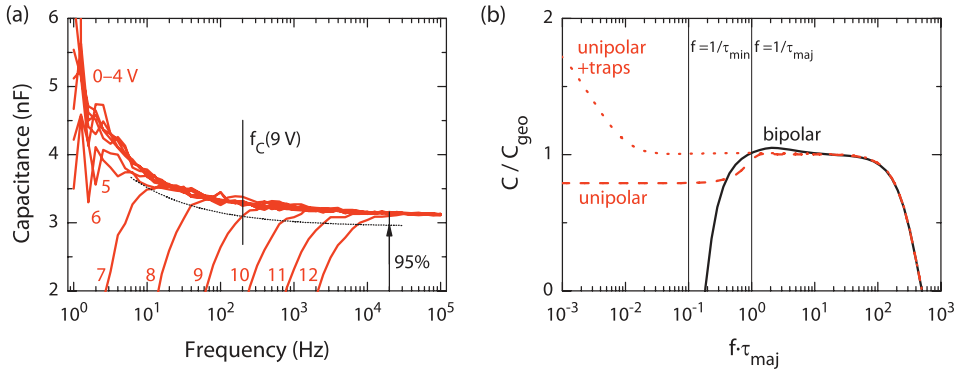

Figure 4.2: (a) Capacitance as a function of frequency of the AC voltage (50 mV) for different DC voltages. The frequency where C is 95% of the low voltage value at 9 V is indicated. The choice of 95% is to allow a better defined value than for 100%. (b) Simulation of the capacitance of a single-carrier device with (dotted line) and without (dashed line) traps, and of a double-carrier device (solid line). Frequency scaled with transit time τ of majority carriers. ($\mu_{min} = 0.1\mu_{maj}$).

the capacitance is 95% of its low voltage value, f_C, are plotted as a function of voltage. A clear correlation between the two frequencies is observed and both curves are approximately showing an exponential increase with voltage. We have looked at the frequency characteristics of the equivalent circuit of the sample and the series resistor. They show no significant changes for the frequencies studied. We thus conclude that the correlation between f_0 and f_C is a genuine effect.

4.4 Discussion

First, we will discuss the observed trends in the capacitance C, which is a measure for the amount of charge that can be stored in the device. In an ideal single-carrier device, at $f \gg 1/\tau$ the dielectric properties of the organic material are probed, giving the geometric capacitance C_{geo}. At $f \ll 1/\tau$, the (majority) charges in the device easily follow the voltage modulation and due to charge relaxation $C = {}^3/_4\, C_{geo}$.[48] The transition between these two regimes occurs around $f = 1/\tau_{maj}$, as illustrated by simulations of a prototype device in Fig. 4.2(b) (dashed line). The strong downturn at high frequencies due to the frequency dependence of the complex permittivity is not observed in the frequency range of our measurements. When traps are present in the device, they increase the ability of the device to store charges, resulting in an increased capacitance, which decreases as the frequency becomes larger than the inverse trapping time, eliminating the contribution from the traps [Fig. 4.2(b), dotted line]. Depending on the amount of traps, the step observed in the single-carrier case is obscured, as is the case in the measured capacitance for $V \leq 6$ V [Fig. 4.2(a)]. In a double-carrier device, due to cancelation of the space charge by the presence of both positive and negative carriers, a much larger amount of charge can be stored in the device, resulting in a large capacitance, which, due to a lag in signal, is negative.[48] At a certain frequency, the response of the slowest (minority) carriers can no longer follow the voltage modulation and C follows the single-carrier case [Fig. 4.2(b), solid line]. This frequency is directly related to their transit time τ_{min}.[49,74] Thus, interpreting the measured capacitance [Fig. 4.2(a)], start-

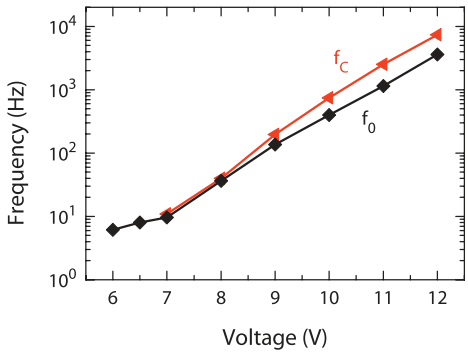

Figure 4.3: Characteristic frequencies of the decrease of MC (f_0, diamonds) and of the negative capacitance (f_C, triangles) as a function of voltage. Obtained from fitting the dMC/dB data in Fig. 4.1(a) and the point where the negative capacitance is 95% of its low voltage value in Fig. 4.2, respectively.

ing from 6–7 V, minority carriers (holes) are efficiently injected, and their contribution is present up to increasing frequencies for increasing voltage.

Based on the foregoing analysis, the correlation between f_0 and f_C implies that beyond frequencies where the AC response of the minority carriers is diminished, the MC is significantly reduced. This correlation between the voltage modulation and magnetic field modulation is not trivial. In the first case, the electric field is changed, $E(t)$, while in the second case the mobility or recombination mobility is most likely changed by the change of the magnetic field, $\mu[B(t)]$. To illustrate the different behavior, for a single-carrier device, a change in E requires a change in the charge distribution in the device, while only a change in μ does not. In a double-carrier device, with injection barriers and recombination, the situation is not so clear, but a different situation is expected.

We will discuss the two different cases: the magnetic field acting on the majority mobility or the recombination mobility, and the magnetic field acting on the minority mobility. First, let's assume that the magnetic field acts on the majority mobility ($\mathrm{d}\mu_{\mathrm{maj}}/\mathrm{d}B \neq 0$) or the recombination mobility ($\mathrm{d}\mu_{\mathrm{r}}/\mathrm{d}B \neq 0$). In a double-carrier device with recombination, if any of these two mobilities changes, the charge balance in the device will change, requiring charges to be injected or extracted. The frequency dependence of this injection and extraction is described by the admittance. At low frequencies, both minority and majority carriers can respond to the changes, canceling each others space charge and thus allowing large changes in charge density and consequently in current (hence, also a large negative capacitance is observed). At higher frequencies, where the minority carriers can no longer keep up with the changes, only the majority carriers will respond. Now, the minority carriers cannot cancel the resulting space charge, giving a much smaller, *but finite*, response in the current and thus the observed MC.

Second, in the case of the magnetic field only acting on the mobility of the minority carriers ($\mathrm{d}\mu_{\mathrm{min}}/\mathrm{d}B \neq 0$), on the other hand, a similar argument as above results in the change in the current *going to zero* at high frequencies. This interpretation is in agreement with recent results. From experiments on OMAR in single carrier devices,

it is known that the magnetic field acts most strongly on the minority carriers.[143] It has been shown that even in double-carrier devices, the magnetic field effects in the minority mobility dominate the total magnetic response of the current, even though the majority mobility is much larger.[15,16] In addition, via the space charge, a change in minority mobility gives a change in the current with an opposite sign.[15] In the bipolaron model, a negative MC is the most dominant effect,[20,141] in agreement with experiments on single-carrier devices where the MC is always negative.[90,143] The observed positive MC is then the opposite response of the majority carriers to the negative effects of the minority carriers. Below the onset of minority carrier injection, only the effects in the majority carriers are expected, with a negative MC. As we do not observe any (negative) MC at low voltages, below the onset of hole injection, we might conclude that the magnetic field effects in the electrons (majority carriers) are negligible small. Therefore, modulating the magnetic field at frequencies above the transit time of the minority carriers, results in a quenching of the total MC.

Although both scenarios give a good qualitative explanation of the observed effects, other origins or more complex interactions cannot be excluded. Therefore, a conclusive prediction on the applicable model cannot yet be made. However, by performing device simulations a more decisive conclusion might be drawn. Such simulation are currently being performed to get an idea of how changes in one of the mobilities would exactly be reflected in the current, also taking into account effects resulting from for instance traps and injection barriers.

4.5 Conclusion

In conclusion, we have shown frequency dependent OMAR measurements, using a superposition of a DC and an AC magnetic field. We observed a decrease of MC with increasing frequency. The decrease is stronger for lower voltages, which is shown to be linked to the presence of a negative capacitance that disappears when the frequency becomes comparable to the inverse transition time of the minority carriers. We show that this interpretation is in agreement with recent results. However, device simulations need to be performed to allow us to discriminate between different models.

Angle dependent spin–spin interactions in organic magnetoresistance

5

*The dependence of organic magnetoresistance (OMAR) on the orientation of the magnetic field has been investigated. In contrast to previous claims, a clear and systematic, though small, change in magnitude is observed when the orientation of the field is changed with respect to the sample. The characteristic field scale of the effect remains approximately constant. To explain these effects, spin–spin interactions have been included in the models previously suggested for OMAR, in combination with either an anisotropy of the orientation of the spin pairs or an anisotropy in the hyperfine fields. The essential spin–spin interaction is dipole coupling, but, depending on the assumptions, exchange interaction also has to be included.**

5.1 Introduction

In organic devices, considerable changes in the current have been observed when applying a magnetic field, an effect called organic magnetoresistance (OMAR), see Sect. 1.3.2. OMAR is generally believed to originate from spin correlations of interacting charge carriers. The spin character of such pairs is mixed by the random hyperfine fields, which can be suppressed by an external magnetic field, resulting in a typical field scale of the effect of a few millitesla. Gaining a better understanding of the physics of OMAR will improve knowledge of (spin) transport in organic semiconductors and could help realizing possible applications, for instance in adding the possibility of sensing magnetic fields to cheap organic electronic devices.

So far, in literature, it has been claimed that OMAR is independent of the orientation of the applied magnetic field.[11,43] Indeed, the effect is not just observed for a specific angle between the magnetic field and the current (like the Hall effect). The models suggested for OMAR (Sect. 1.3.3), like the electron–hole (e–h) pair model[106] and the bipolaron model,[20] do not predict any angle dependence of OMAR.

In this paper we report on angle-dependent measurements of OMAR. We show that

*In Preparation: *Angle dependent spin–spin interactions in organic magnetoresistance* W. Wagemans, A.J. Schellekens, M. Kemper, F.L. Bloom, and B. Koopmans.

changing the orientation of the applied magnetic field with respect to the sample results in a small but systematic change in the magnitude of OMAR. We show that anisotropic spin–spin interactions are a likely candidate to explain the observed effects. Thereby, we provide a new handle to electrically study spin–spin interactions in disordered organic materials. A related effect has previously been found in photoluminescence measurements on organic crystals, where the authors also suggest an angle dependence due to spin–spin interactions. [50]

5.2 Experimental

We performed our experiments on typical OLED-like devices. In discussing our results we will focus on devices with tris-(8-hydroxyquinoline) aluminum (Alq_3) as the active layer. We note that we also observed an angle dependence in devices with poly[2-methoxy-5-(3',7'-dimethyloctyloxy)-1,4-phenylene vinylene] (MDMO-PPV), but due to the low signal to noise ratio it was not possible to perform a similar in-depth study as presented here for Alq_3. The devices consist of a glass substrate with a patterned indium tin oxide electrode on which poly(3,4-ethylenedioxythiophene):poly(styrenesulfonate) (PEDOT:PSS) is spin coated (60 nm). Then, Alq_3 (120 nm) is evaporated in a high vacuum system inside a nitrogen filled glove box, after which a top electrode is evaporated consisting of LiF(1 nm)/Al(100 nm). The created devices (active area 3 mm × 3 mm) are transported to a different glove box in which they are electrically measured, while a magnetic field can be applied. For detailed measurements and to suppress the drift in current that can be present, we use an additional AC modulation of the magnetic field to measure the derivative of the current I to the magnetic field B, $\mathrm{d}I/\mathrm{d}B$, which is then integrated with respect to the magnetic field to get $I(B)$, see Sect. 2.4. From $I(B)$, the magnetoconductance is calculated with $\mathrm{MC} = [I(B) - I(0)]/I(0)$.

5.3 Results

A clear difference in MC is observed between parallel ($\theta = 0°$) and perpendicular ($\theta = 90°$) alignment of the magnetic field with respect to the sample normal, see Fig. 5.1(a). The MC for the perpendicular case is larger than the parallel case; the difference is 4.3% of the MC at 40 mT. This difference is only 0.14% of the total current, showing that, in order to observe these effects, both very stable samples and a sensitive measurement technique are required. The inset of Fig. 5.1(a) shows the MC as a function of voltage, $\mathrm{MC}(V)$, as measured with a permanent magnet of 83 mT, see Sect. 2.3. [142] $\mathrm{MC}(V)$ shows a typical behavior where the MC first increases with voltage, has a maximum and then slowly decreases.

The MC for intermediate angles shows an oscillation as a function of θ on top of a slowly increasing signal, see Fig. 5.1(b). Vertically plotted is MC_∞, which was obtained from fitting the $\mathrm{MC}(B)$ curves with a typical 'non-Lorentzian' that is commonly seen in OMAR measurements: [79] $\mathrm{MC}(B) = \mathrm{MC}_\infty B^2/(|B| + B_0)^2$, where MC_∞ is the MC at infinite magnetic field and B_0 is the half width at quarter maximum. Within the accuracy of the fits, no change in B_0 is observed. The data can be accurately fitted with a $\cos^2\theta$ dependence plus a linear contribution. The slow increase in signal is due to slight conditioning. [5]

Using a different method, the $\cos^2\theta$ dependence is confirmed. While applying a

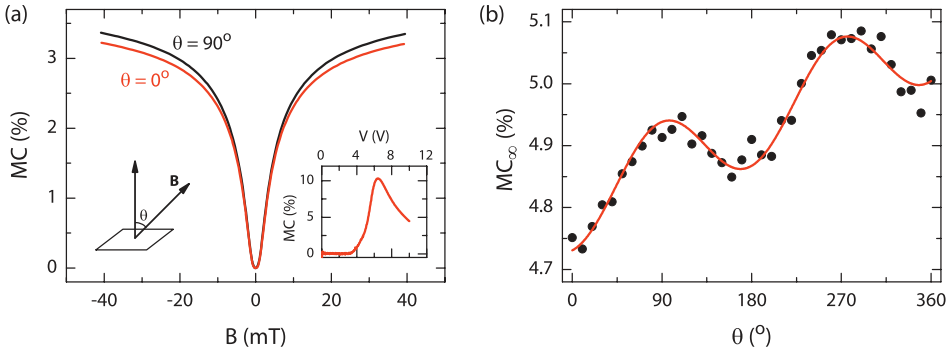

Figure 5.1: (a) Two MC(B) curves measured with dI/dB at 12 V with dB = 0.5 mT at 27 Hz for $\theta = 0°$ and $\theta = 90°$, with θ as indicated. The inset shows the MC as a function of voltage at 83 mT. (b) MC_∞, obtained from fitting with a non-Lorentzian, as a function of angle. The data is fitted with a $\cos^2\theta$ contribution plus a linear contribution.

constant voltage and monitoring the current versus time, the magnetic field is switched on and off, after which the sample is slowly rotated while the field is on. A typical measurement at 500 mT is shown in Fig. 5.2(a). The current initially decreases rapidly, then the magnetic field is switched off and on four times, after which the sample is slowly rotated from 0° to 180° and back again 13 times. Finally, the field is switched off and on once more. The difference in switching behavior for switching the magnetic field on and off is caused by the impedance characteristics of the coil and the MC(B) curves having a much larger slope at small fields. From the large steps, the MC at the applied field is calculated. Assuming a linear rotation in time, the angle dependence of the MC is extracted from the rotation of the sample, see the inset in Fig. 5.2(a). Again, this dependence can be fitted with a $\cos^2\theta$ dependence. The observation of an angle dependence with this method, i.e., measuring $I(\theta)$ at fixed B and V, unambiguously shows that possible induction effects from the AC magnetic field used for the dI/dB measurements are not responsible for the observed effects.

The magnetic-field dependence of the change in current between parallel and perpendicular orientation can be directly measured using the method described above. For this, we calculate $\delta I = (I_\perp - I_\parallel)/I_\parallel$ for measurements performed at different fields, see Fig. 5.2(b). The largest change is observed at high magnetic field, where the effect saturates. Interestingly, $\delta I(B)$ has the same shape as MC(B), showing that the width remains approximately constant and the rotation only acts to modulate the magnitude of the MC. Furthermore, the shape of the $\delta I(B)$ curve excludes field inhomogeneities as a source of the angle dependence, as these would give the largest effects at low fields, where the slope of MC(B) is largest.

In addition to the magnetic-field dependence, also the voltage dependence is investigated. For different voltages, a measurement like in Fig. 5.2(a) was performed to obtain the MC and δI at 250 mT. It was not possible to determine the angle dependence for voltages below 7.5 V as the noise in the signal exceeded the change in signal from rotating the sample, so only the declining slope of the MC(V), as plotted in the inset in Fig. 5.1(a), was measured. Both MC(V) and δI show the same declining trend,

which results in a constant ratio $\delta I/\mathrm{MC}$, see Fig. 5.2(c), left axis. In the same figure the current as a function of voltage is plotted. While the ratio remains constant in this voltage range, the current increases by 2.5 orders of magnitude. From these observations we conclude that the angle dependence is an intrinsic property of OMAR and is not an independent effect or a measurement artifact.

5.4 Discussion

As the angle dependence seems to be a modulation of the OMAR effect, we have to look at the mechanisms suggested for OMAR to find a possible explanation. In all suggested models, the random hyperfine fields mix spin pairs, which either have like charge (bipolarons) or opposite charge (e–h pairs or excitons), see Sect. 1.3.3. Such spin pairs can have either a singlet (S) or triplet (T) character with total spin 0 or 1, respectively. The orientation of the spin of the triplets is determined by the magnetic field, for $\mathrm{T}_{+(-)}$ they are aligned (anti-)parallel to the field and for T_0 perpendicular. In the models, at low fields, the hyperfine field mixes S and *all* T states, while at high field *only* S and T_0 are mixed, resulting in the typical OMAR curves.

The strength of the mixing between S and T_0 is determined by their energy difference compared to the hyperfine field, see Fig. 5.3. For angle dependence at high fields, two effects can be considered as illustrated in Fig. 5.3 by the red arrows. By changing the angle, either the magnitude of the hyperfine field B_{hf} is changed, or the energy difference between S and T_0 is changed. These changes result from either an anisotropy in the hyperfine fields or an anisotropy in the energy difference between S and T_0. Note that for an effect resulting from a change in the magnitude of B_{hf}, an energy difference between S and T_0 needs to be present. An energy difference between S and T_0 can originate from spin–spin interactions in the pairs, like exchange coupling or dipole coupling. A dipole coupling will induce an energy difference which reduces the total mixing, in turn reducing the total magnitude of OMAR. So far, these spin–spin interactions were neglected in the models.

To understand the influence of dipole coupling, first, we will discuss it based on a semi-classical picture. This fails at some details that require a quantum mechanical approach, which will be discussed later. In a semi-classical picture, we can imagine the two spins of S to be pointing in opposite directions, while they are pointing in the same direction in T_0, see Fig. 5.4. The dipole energy of two spins pointing in the same direction is larger when they are head to tail than when they are next to each other, and vice versa. This means that for S and T_0 the angle between the magnetic field and the displacement vector **R** (as defined in Fig. 5.4) determines the strength of the dipole coupling between the two spins. Figures 5.4(a) and (b) give a schematic picture of S and T_0 with the field and the displacement vector either parallel or perpendicular, respectively. The spins perform a precession in the magnetic field, as indicated by the circles. One third of a full rotation is indicated by the shaded arrows. For **B** and **R** parallel [Fig. 5.4(a)], the spins of S have the same (large) dipole coupling throughout the precession. The dipole coupling of T_0 also remains constant, but is smaller. For **B** and **R** perpendicular [Fig. 5.4(b)], the spins of S and T_0 both have a varying coupling during their precession. This shows that rotating the field with respect to the displacement vector results in a different (average) dipole coupling strength. If we now assume a preferential orientation between the spin

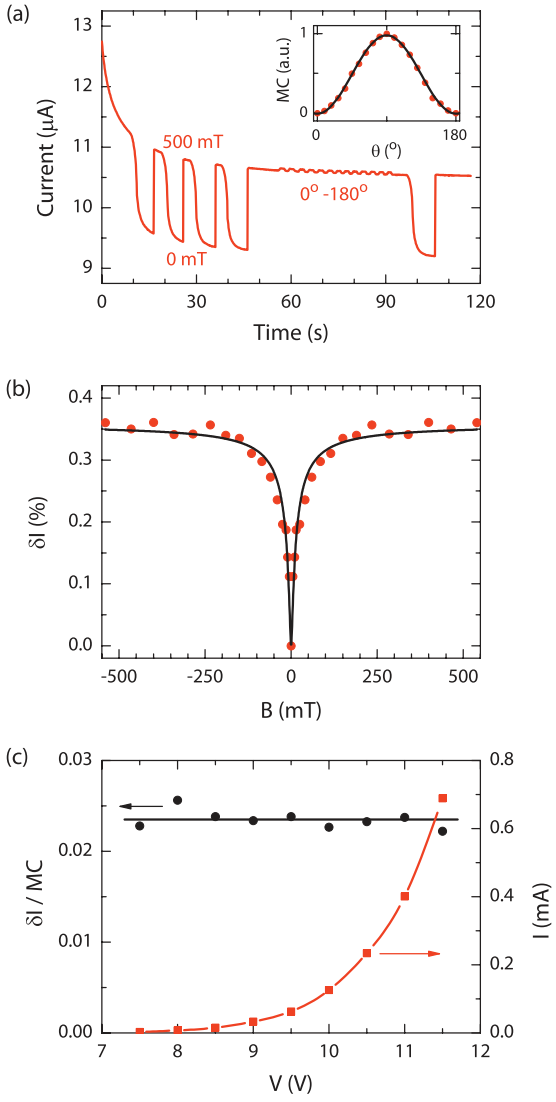

Figure 5.2: (a) Current versus time at 15 V, while switching the magnetic field off and on and rotating the sample. The inset shows the angle dependence obtained from the rotation. (b) Change in current between parallel and perpendicular orientation as a function of field. The data is mirrored for negative fields. The measurement has been performed at 15 V with Alq_3(240 nm)/Ba(10 nm)/Al(100 nm). (c) Ratio δI/MC (left axis, circles) and current (right axis, squares) as a function of voltage at 250 mT.

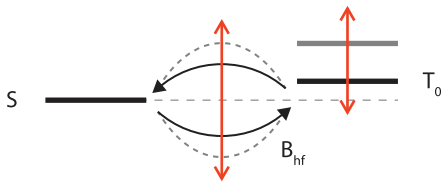

Figure 5.3: Energies of S and T_0. The vertical red arrows indicate a change in the magnitude of the hyperfine field and in the relative energy difference between S and T_0.

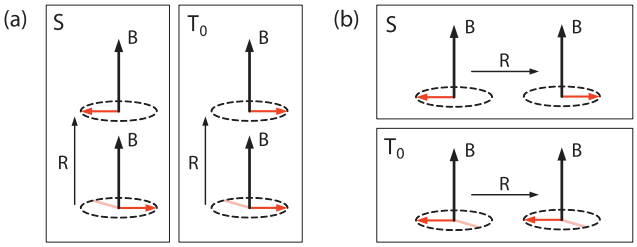

Figure 5.4: Spin pair, in S and T_0 configuration, precessing in a magnetic field **B**, with **B** and the displacement vector **R** either (a) parallel or (b) perpendicular.

pairs in a device, i.e., an anisotropy in **R**, the introduction of a finite dipole coupling will directly give an angle dependence. On the other hand, an anisotropy in the hyperfine fields, in combination with a non-zero isotropic energy splitting of S and T_0 at high fields, also results in different mixing depending on the orientation of the external field. The possible link of the mechanisms causing anisotropy with the devices structure will be discussed after investigating their effects in more detail.

To get an idea about the magnitude of the angle dependence and which orientation is more favorable for OMAR, a more detailed analysis is needed. To study the effect of dipole coupling for the bipolaron and e–h models, it is necessary to use a density matrix description of the spin system. For the equation of motion of the density matrix $\boldsymbol{\rho}$, we use the stochastic Liouville equation:[60]

$$\frac{\partial \boldsymbol{\rho}}{\partial t} = -\frac{i}{\hbar}[\mathbf{H}(t), \boldsymbol{\rho}(t)] - \frac{1}{2}\{\Lambda, \boldsymbol{\rho}(t)\} + \Gamma = 0. \tag{5.1}$$

The first term is the Liouville term describing the evolution of the density matrix under the influence of the Hamiltonian of the system **H**; here, the square brackets denote the commutator. The second term is a 'sink' term that spin-selectively removes particles from the system, using the projection operator Λ; here, the curly brackets denote the anti-commutator. The last term Γ is a source term that adds particles and is independent of the current state of the system. As a basis we use the eigenstates of the total spin operator $\mathbf{S}^2_{\text{tot}}$.

For simplicity, we choose to only discuss the implementation of Eq. (5.1) for the e–h model, but we stress that *completely equivalent results are obtained with the bipolaron model*. Starting from free carriers, e–h pairs are created with a rate r, resulting in $\frac{3}{4}r$ triplets and $\frac{1}{4}r$ triplets, as illustrated in Fig. 1.14 on p. 24. These can dissociate back into free carriers with rates q_{T} and q_{S}, and recombine to the ground state with rates k_{T}

and k_S.[106] S and T can be mixed by a hyperfine contribution to the Hamiltonian. For Eq. (5.1) this results in $\Lambda_{\mu,\nu} = (k_S+q_S)\rho_{\mu,\nu}(\delta_{0,\nu}+\delta_{\mu,0})+\sum_{n=1}^{3}(k_T+q_T)\rho_{\mu,\nu}(\delta_{n,\nu}+\delta_{\mu,n})$ and $\Gamma_{\mu,\nu} = \frac{1}{4}r\delta_{\mu,\nu}$, where $\delta_{\mu,\nu}$ is the delta function, $n = 0$ refers to the singlet, and n =1–3 to the triplets. The singlets and triplets are mixed by a hyperfine contribution to the Hamiltonian:

$$\mathbf{H}_{\mathrm{hf}} = g\mu_B\left[\mathbf{B}_{\mathrm{hf},1}\cdot\mathbf{S}_1 + \mathbf{B}_{\mathrm{hf},2}\cdot\mathbf{S}_2\right], \tag{5.2}$$

where μ_B is the Bohr magneton and g is the g-factor of a polaron. The triplets are split in energy by a Zeeman term:

$$\mathbf{H}_Z = g\mu_B\mathbf{B}\cdot(\mathbf{S}_1+\mathbf{S}_2). \tag{5.3}$$

Now, with $\boldsymbol{\rho}$ obtained from solving Eq. (5.1), the recombination probability is:

$$P = \frac{k_S\rho_{0,0}+\sum_{n=1}^{3}k_T\rho_{n,n}}{(k_S+q_S)\rho_{0,0}+\sum_{n=1}^{3}(k_T+q_T)\rho_{n,n}}. \tag{5.4}$$

In the e–h model, Prigodin *et al.* introduced the magnetic-field dependence of the current via the recombination mobility μ_r.[106] The authors show that in the bipolar space-charge limited regime, the current is proportional to $\mu_r^{-1/2}$ and that μ_r is proportional to P. This results in $\mathrm{MC} = [P(B)^{-1/2} - P(0)^{-1/2}]/P(0)^{-1/2}$.

To investigate the effects of spin–spin interactions, dipole coupling and exchange coupling are added. The dipole coupling term that is added to the Hamiltonian is:[100]

$$\mathbf{H}_{\mathrm{dip}} = D\left[\mathbf{S}_1\cdot\mathbf{S}_2 - 3\left(\mathbf{S}_1\cdot\mathbf{R}/R\right)\left(\mathbf{S}_2\cdot\mathbf{R}/R\right)\right], \tag{5.5}$$

where $\mathbf{S}_1$ and $\mathbf{S}_2$ are the spin operators of the two spins, and D is the dipole coupling strength: $D = \mu_0 g^2\mu_B^2/(4\pi\hbar R^3)$, where μ_0 is the permeability of free space and $\hbar$ is Planck's constant. For a typical displacement of 1.5 nm, the dipole interaction strength is approximately 1 mT.[100] We note that this is a point dipole approximation, ignoring the three dimensional structure of the molecular orbitals. The exchange term that is added to the Hamiltonian is:

$$\mathbf{H}_{\mathrm{ex}} = -J\left(\frac{1}{2} + 2\mathbf{S}_1\cdot\mathbf{S}_2\right), \tag{5.6}$$

with $J = J_0 e^{-2\frac{R}{R_0}}$, where J_0 and R_0 are determined by the inherent strength of the exchange interaction. At large fields, where only S–T_0 mixing is relevant due to Zeeman splitting, the absolute energy difference between S and T_0 is $\frac{1}{2}|D(1-3\cos^2\alpha) - 4J|$, where α is the angle between the applied field and the displacement vector. This yields an angle-dependent mixing between the S and T_0 states and thus a difference in MC at large fields.

Now, we can calculate MC(B) for a parallel and perpendicular alignment of **B** and **R**, see Fig. 5.5(a). For this, we average over a Gaussian distribution of the x, y and z components of the hyperfine fields, each with an average value B_{hf}.[121] The MC curves show a typical OMAR shape and, most notably, $\alpha = 90°$ shows a larger MC, while the width remains nearly unchanged. We note that this is the first time that full line shapes have been calculated instead of only investigating zero and infinite magnetic field. The most prominent effect of the dipole coupling is to change the magnitude. This is in

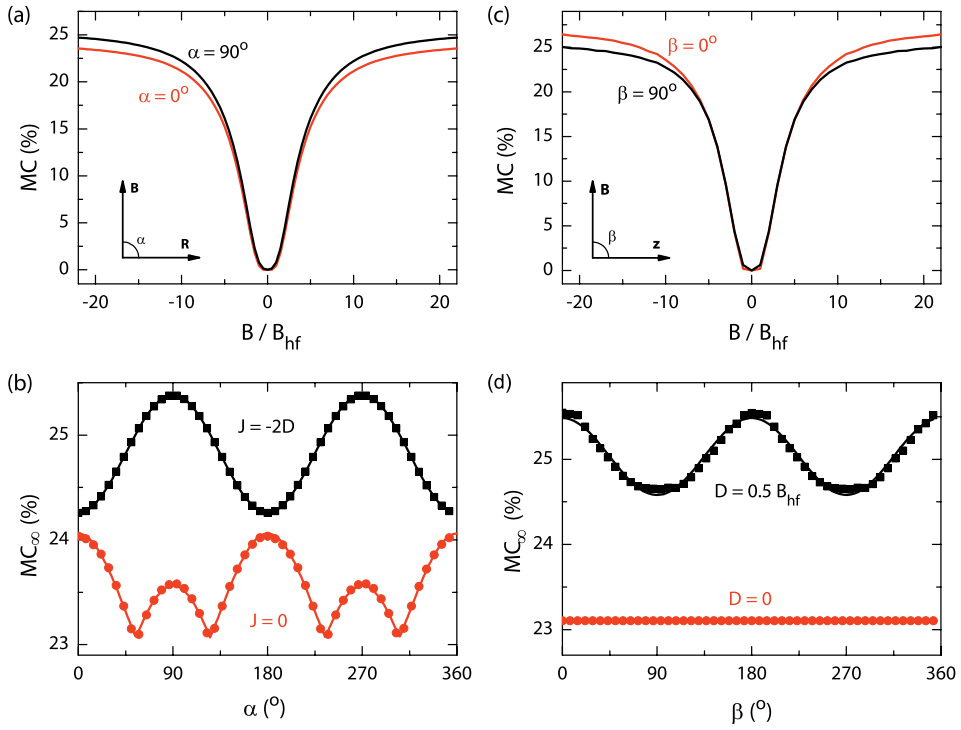

Figure 5.5: Simulated MC for the e–h model with (a,b) anisotropic **R** and (c,d) anisotropic B_{hf}, with $q_{\mathrm{S}} = q_{\mathrm{T}} = 1$, $k_{\mathrm{S}} = 10$, and $k_{\mathrm{T}} = 0$. (a) MC for two orientations of B with $D = 0.05B_{\mathrm{hf}}$ and $J = -0.1B_{\mathrm{hf}}$ (b) Angle dependence with and without exchange coupling. (c) MC for two orientations of B with $D = 0.5B_{\mathrm{hf}}$ and $B_{\mathrm{hf},z} = \frac{3}{4}B_{\mathrm{hf}}$. (d) Angle dependence with and without dipole coupling. (b,d) fitted with $|c_1 \cos^2 \alpha - c_2|$.

agreement with the conclusion from the experiments that the width of the MC curves is not affected. However, when D becomes comparable to B_{hf}, a small broadening is noticeable (not shown). At much larger D, two separate features at positive and negative field are even predicted, due to level crossings. As no such features or broadening is observed, we conclude that D is smaller than B_{hf}.

In Fig. 5.5(b), the MC at infinite magnetic field is plotted as a function of angle. First, we consider the case without exchange coupling ($J = 0$). Unlike the experiments, a curve with four maxima is observed. These maxima are caused by the absolute value in the energy difference between S and T_0 being $\frac{1}{2}D|3\cos^2\alpha - 1|$. An angle dependence corresponding with experiments is obtained when also including a small exchange coupling ($J \neq 0$). In OMAR models, the exchange has so far been ignored because, being exponential with distance, it may be expected to either quench the effect or to be negligible. The exchange coupling plays a more important role in the angle dependence; the energy difference between S and T_0 now is $\frac{1}{2}|D(1 - 3\cos^2\alpha) - 4J|$. So, if $J \leq -\frac{1}{2}D$, the angle dependence will show a $\cos^2\alpha$ behavior, see Fig. 5.5(b), otherwise, more maxima are observed. A maximum angle dependence is thus observed for $J = -\frac{1}{2}D$. Similar behavior has been measured and predicted before for delayed fluorescence in organic

crystals,[50] where the angle dependence was independent from the crystal axes.

Next, we investigate the role of an anisotropy of the hyperfine field. For this, the z component of the hyperfine fields is reduced with respect to the x and y components, and we average over 100 000 random **R** and hyperfine combinations. Also in this case, a dependence is predicted on the angle between **B** and the z axis (β), see Fig. 5.5(c), with the largest MC for **B** aligned with the z axis ($\beta = 0$), which is the axis with the reduced hyperfine field. This can also be seen from the MC at infinite field as a function of angle, see Fig. 5.5(d). We confirm that no angle dependence is observed when $D = 0$ [Fig. 5.5(d)], as there is no splitting to probe the anisotropic hyperfine fields.

Comparing the simulated angle dependence of the two different anisotropies with the measurements, in the case of anisotropic **R**, we find $\theta = \alpha$, which corresponds to **R** aligning with the direction of the electric field. This is not unexpected, as the electric field determines the direction in which the polarons meet. On the other hand, this direction is also the growth direction of the organic layer. So, a preferential **R** could also originate from local ordering of molecules due to preferential growth or from current paths selecting molecules with favorable alignment, both giving a cylindrical symmetry perpendicular to the sample. On the other hand, in the case of anisotropic B_{hf}, we find $\theta = \beta + 90°$, which corresponds to the direction of reduced hyperfine field aligning perpendicular to the direction of the electric field. The hyperfine fields originate from the coupling of the spins of the polarons to the hydrogen nuclei. For this there are two contributions, an isotropic contact term and an anisotropic dipole–dipole coupling term. Because of the large number of hydrogen nuclei, the coupling is described by a classical hyperfine field, neglecting the anisotropic part.[121] However, for a relatively planar spin density distribution, like on a ligand of Alq_3, a strong anisotropic contribution can be expected. In such a planar configuration, the anisotropic coupling constant for the axis perpendicular to the plane is smaller than for those in the plane.[63] In our experiments, this would correspond to growth of Alq_3 with the ligand preferentially perpendicular to the surface. Moreover, the specific alignment of ligands is crucial for determining the hopping rate, thereby possibly selecting molecules with a preferential orientation. However, different orientations could be optimal for electrons and holes,[64] making it uncertain what kind of orientation is expected in our samples. Note that in this case, no exchange coupling is needed to get the correct angle dependence, but a finite dipole coupling between the charges is still essential.

Even our basic model manages to describe the angle dependence well. So far, we only average over the random hyperfine fields, using constant dipole coupling, exchange coupling and transition rates. It is, however, very likely that the values of these parameters are distributed over a certain range, which could lead to changes in the shape of the MC(B) curve, its magnitude and the angle dependence. Moreover, a 'selection mechanism' might be at work where many pairs contribute to the MC, but only a part of these have the right combination of parameters to show a noticeable angle dependence.

Unfortunately, with these experiments, it is not possible to distinguish between the bipolaron and e–h model. One possible difference between the models could be that we expect a much broader spread in separation distances for the e–h pairs than for bipolarons, as for bipolarons the critical step occurs for nearest neighbors, while for e–h pairs a range of distances is possible. To distinguish between the models and to

further elucidate the individual role of exchange and dipole coupling, materials engineering could be used to change the separation distances of the spin pairs or alter the coupling strengths in a different way. Another interesting condition for studying angle dependence is around a sign change in MC, as it has been suggested to be related to a transition from a bipolaron to an e–h model dominated regime,[143] although, a small signal to noise ratio might be limiting in this range.

5.5 Conclusion

In conclusion, experiments show a clear dependence of the magnitude of OMAR on the orientation of the magnetic field, while the width of the MC(B) curve hardly changes. To explain these effects, spin–spin interactions have to be included in the models, in combination with an anisotropy of either the displacement vector between sites or the hyperfine fields.

Spin diffusion in organic semiconductors 6

In the previous chapters, we have shown that spins in an organic material interact with the random hyperfine fields of hydrogen nuclei. Not only do these interactions play a key role in organic magnetoresistance, the interactions will also have a detrimental effect on the spin polarized transport through an organic layer.

*In this chapter, we present a theory for spin diffusion in disordered organic semiconductors, based on incoherent hopping of a charge carrier and coherent precession of its spin in an effective magnetic field, composed of the random hyperfine field and an applied magnetic field. From Monte Carlo simulations and an analysis of the waiting-time distribution of the carrier we predict a surprisingly weak temperature dependence, but a considerable magnetic-field dependence of the spin-diffusion length. Using a simple device model, we show that both predictions are in agreement with experiments on organic spin valves.**

6.1 Introduction

The study of electron-spin transport through non-magnetic spacer materials in between ferromagnetic electrodes is an extremely active field, because of the rich physics involved and the important applications in the area of magnetic sensors.[146] If the spin-diffusion length is larger than or comparable to the distance between the electrodes, the current through such structures depends strongly on the mutual orientation of the magnetization directions of the electrodes, which is called the spin-valve effect, leading to 'Giant Magnetoresistance' (GMR),[6,13] see also Sect. 1.2.

Traditionally, non-magnetic metals are used as the spacer-layer material in these structures. Spintronic devices utilizing spin injection and transport through a *semiconducting* spacer layer offer additional functionalities, such as spin transistors and the possibility to realize quantum computation logic. Consequently, much effort is put into

*Published as: *Theory for Spin Diffusion in Disordered Organic Semiconductors* P.A. Bobbert, W. Wagemans, F.W.A. van Oost, B. Koopmans, and M. Wohlgenannt, Phys. Rev. Lett. 102 (15), **156604** (2009), and as part of its supplementary information. W.W. mostly contributed to Sect. 6.4.

finding suitable materials. Spin relaxation in the inorganic materials traditionally used in these structures, containing relatively heavy atoms, is mainly caused by spin-orbit coupling.[104] Organic semiconductors (OS) are a very interesting alternative because of the enormous versatility of organic chemistry and because the light atoms from which they are composed cause very little spin-orbit coupling,[109] see also Sect. 1.3. Recent years have seen the first demonstrations of GMR devices[34,35,40,68,103,144,149] as well as magnetic tunnel junctions[114] using OS as spacer layer. Here we will investigate the former type of devices. The experiments reported so far have shown that when the thickness of the OS spacer layer increases, the GMR effect in these devices disappears on a typical length scale of the order of 10–100 nm. Two very important and still unanswered questions, addressed in this Chapter, are: what is the cause of the remaining spin relaxation and what factors determine the spin-diffusion length?

6.2 Model

Recent research on magnetic-field effects of the resistance and luminescence of OS has led to the conclusion that the hydrogen hyperfine fields are involved, influencing reactions between spin-carrying radicals (polarons, triplet excitons).[20,39,62,106] The accurate prediction of magnetoresistance line shapes assuming coupling of the spin to these hyperfine fields[20] strongly suggests that this coupling is the main source of spin relaxation in OS. In this Chapter, we take this as our working hypothesis. Since typically many (~10 or more) hydrogen nuclear spins couple to the spin of a charge carrier in OS, we can replace the hyperfine coupling by a classical, quasi-static, and random field, distributed according to a three-dimensional Gaussian,[121] with standard deviation $B_{\rm hf}$. In addition, we model charge transport in disordered OS by hopping of carriers between localized sites with random site energies, distributed according to a Gaussian density of states (GDOS) with standard deviation σ.[9] Hence, we describe spin diffusion in these materials by a combination of *incoherent* hopping of a carrier in a GDOS together with *coherent* precession of its spin $\mathbf{S}(t)$ around a local effective magnetic field, see Fig. 6.1a. At each hopping site i this effective field is $\mathbf{B}_i = \mathbf{B}_{{\rm hf},i} + \mathbf{B}$, where $\mathbf{B}_{{\rm hf},i}$ is the random hyperfine field at this site and $\mathbf{B} = B\hat{\mathbf{z}}$ the externally applied magnetic field, e.g. the field to which a GMR device should respond. With typically $B_{\rm hf} \approx 5\,{\rm mT}$ the hyperfine precession frequency is $\omega_{\rm hf} = \gamma B_{\rm hf} \approx 10^{-8}\,{\rm s}^{-1}$ (γ is the gyromagnetic ratio).

We consider the situation that a carrier with unit charge e (electron or hole) and spin fully polarized in the z-direction is injected by an electrode into the organic material at $x = 0$ and moves to the opposite electrode under the influence of an electric field $\mathbf{E} = E\hat{\mathbf{x}}$. We assume that nearest-neighbor hopping takes place by thermally assisted tunneling[83] from site i to j with a rate $\omega_{ij} = \omega_{\rm hop} \exp[-(\varepsilon_j - \varepsilon_i)/k_{\rm B}T]$ for $\varepsilon_j \geq \varepsilon_i$ and $\omega_{ij} = \omega_{\rm hop}$ for $\varepsilon_j < \varepsilon_i$, where T is temperature, $k_{\rm B}$ is Boltzmann's constant, and ε_i and ε_j are the on-site energies of sites i and j, with a contribution due to the electric field added. The prefactor $\omega_{\rm hop}$ contains a phonon attempt frequency as well as a factor related to a wave-function overlap. For hopping in disordered OS at not too low temperatures it is a good approximation to include only nearest-neighbor hopping.[102] Furthermore, it has been shown that positional disorder is much less important than energetic disorder,[9] so for simplicity we neglect positional disorder and take a fixed nearest-neighbor distance a.

Clearly, the ratio $r \equiv \omega_{hop}/\omega_{hf}$ is an important parameter. If r is large, the influence of the hyperfine field is small and large spin-diffusion lengths can be expected, while the opposite holds if r is small. For derivatives of the familiar π-conjugated polymer poly-(*para*-phenylene vinylene) (PPV) we obtain an estimate of 10^9–10^{11} s^{-1} for ω_{hop}.[102] Hence, for this class of organic semiconductors r is of the order of 10–1000, but the large variation even within this class shows that very different values can be expected for different organic semiconductors.

6.3 Spin diffusion

It is instructive to first consider a one-dimensional (1D) chain of sites for the case $E \gg \sigma/ea$, when all hops are down-field with the same rate ω_{hop}, leading to equal average waiting times $1/\omega_{hop}$ at each site. By solving the time-dependent Schrödinger equation for the spinor in the effective magnetic field and performing an average over the random hyperfine fields (in cylindrical coordinates ρ, ζ), one can easily derive the following expression for the relative preservation, λ, of spin polarization, p, during the waiting time of the carrier at a site (see supplementary material of Ref. 22 for details),

$$\begin{aligned}\lambda &= \frac{1}{\sqrt{2\pi}} \int_0^\infty \rho d\rho \int_{-\infty}^{\infty} d\zeta \, \exp\left(-\frac{\rho^2+\zeta^2}{2}\right) \frac{r^2+(\zeta+b)^2}{r^2+\rho^2+(\zeta+b)^2}, \\ &\approx \exp\left\{-\left[1/\ln(3) + r^2/2 + b^2/2\right]^{-1}\right\},\end{aligned} \tag{6.1}$$

with $b \equiv B/B_{hf}$. This leads to an exponentially decaying polarization $p(x) = \exp(-x/l_s)$, with a spin-diffusion length $l_s = -a/\ln\lambda \approx a[1/\ln(3) + r^2/2 + b^2/2]$. The increase of l_s with increasing b and r can be readily understood qualitatively: with increasing b, the Zeeman coupling becomes increasingly dominant over the hyperfine coupling and the carrier spin becomes effectively pinned. The quadratic increase with r results from 'motional narrowing', well-known in magnetic-resonance spectroscopy.[12]

For the three-dimensional (3D) situation we performed Monte Carlo simulations for hopping of a single carrier in a homogeneous electric field of arbitrary magnitude on a cubic lattice of sites ($N \times 50 \times 50$, where N is adapted to the specific situation), while *simultaneously* solving the time-dependent Schrödinger equation for its spinor (see supplementary material of Ref. 22 for details). The random site-energies and hyperfine fields are drawn from their corresponding Gaussian distributions. Sufficiently far from the injecting layer, $p(x)$ decreases exponentially, from which we extract l_s. We averaged over several thousands of energetic and hyperfine disorder configurations, making sure that the error bar in the plots discussed below is smaller than the symbol sizes shown.

In Fig. 6.1(b) we show l_s as a function of E for different reduced disorder strengths $\hat{\sigma} \equiv \sigma/k_B T$, for $r = 1000$ and $B = 0$. The arrow at the right axis shows the value obtained for the 1D model discussed above, which is quite close to the present results at large E. For other values of $r \gg 1$ (fast hopping) we find a similar dependence on E as shown in Fig. 6.1(b). For $r \leq 1$ (slow hopping) we find $l_s \sim a$, indicating that for this case no significant spin-diffusion length is found. The relevant case for the experiments carried out up to now corresponds to $E \ll \sigma/ea$,[34,35,40,68,103,144,149] so from now on we will focus on this case. We note that whereas l_s decreases steeply for $E \to 0$, it remains

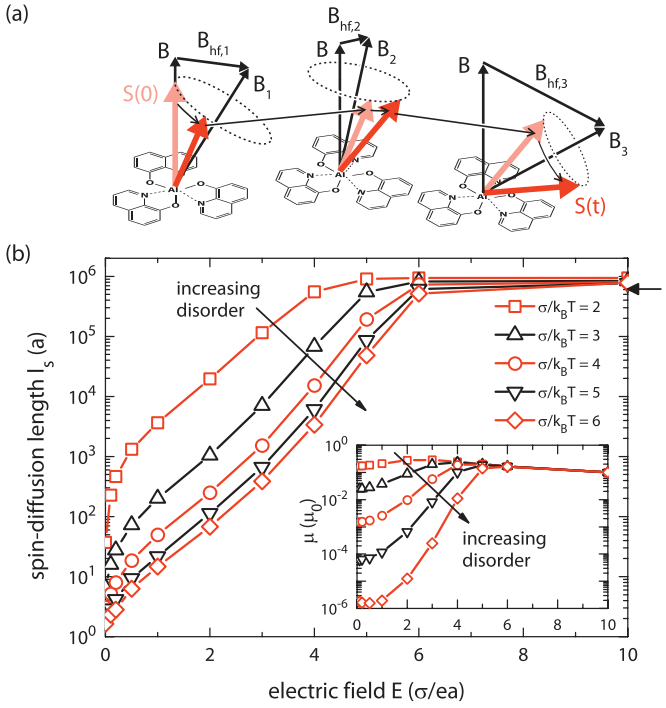

Figure 6.1: (a) Mechanism for spin diffusion, in this case for the molecular semiconductor Alq_3. (b) Spin-diffusion length l_s [as multiples of the lattice constant] vs. electric field E at zero magnetic field, for $r \equiv \omega_{hop}/\omega_{hf} = 1000$ and different $\hat{\sigma} \equiv \sigma/k_B T$. The arrow at the right axis indicates the result for a one-dimensional chain at large E. Inset: corresponding mobility μ vs. E, in units of $\mu_0 \equiv ea^2\omega_{hop}/\sigma$.

non-zero at $E = 0$.

The inset in Fig. 6.1(b) shows the carrier mobility μ as a function of E (for comparison: the unit μ_0 is of the order of 10^{-7}-10^{-5} m^2/Vs for the PPV derivatives studied in Ref. 102). A strikingly different trend with increasing $\hat{\sigma}$ is observed for l_s compared to μ at small and intermediate E: while μ keeps on decreasing very rapidly with increasing $\hat{\sigma}$, l_s depends rather weakly on $\hat{\sigma}$ and even appears to saturate for large $\hat{\sigma}$. In order to provide an explanation for the weak dependence of l_s on $\hat{\sigma}$ we show in Fig. 6.2a the distribution $P(\tau)$ of waiting times $\tau^\dagger$ of the carrier while hopping through the lattice, at $E = 0$ and different $\hat{\sigma}$. The curves appear to saturate for large $\hat{\sigma}$. By considering hops upwards in energy from a Boltzmann distribution in the GDOS one can in fact prove[21] that $P(\tau)$ converges for large τ to a universal algebraic distribution $P(\tau) \sim \tau^{-3/2}$ in the limit $\hat{\sigma} \to \infty$, see the dashed line in Fig. 6.2(a). We note that $P(\tau)$ for a GDOS has been studied before,[52] but for too small disorder strengths ($\hat{\sigma} \leq 4$) to observe this universal behavior.

The quite different dependencies of l_s and μ on $\hat{\sigma}$ can now be understood as follows.

[†] The concept of a waiting-time distribution was originally introduced in the field of dispersive transport; see Ref. 117.

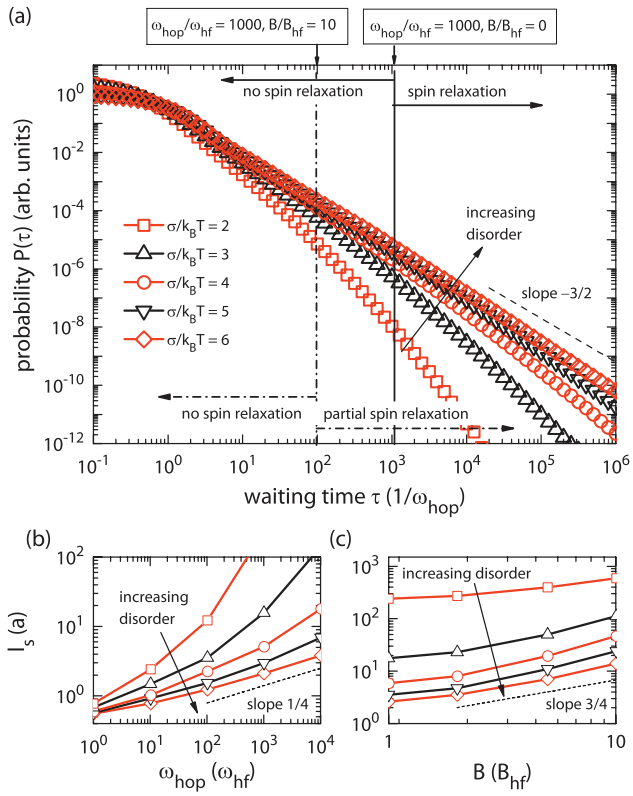

Figure 6.2: (a) Waiting-time distributions (equally normalized) at $E = 0$ for different $\hat{\sigma} \equiv \sigma/k_B T$. Solid and dash-dotted lines and arrows: see the main text. (b) l_s at $E = 0.1\sigma/ea$ as a function of ω_{hop} at $B = 0$ and (c) as a function of magnetic field B for $r \equiv \omega_{hop}/\omega_{hf} = 1000$. The dashed lines in (a–c) indicate the expected power laws.

With increasing $\hat{\sigma}$ the tail of the distribution $P(\tau)$ contains an increasing amount of sites with very large τ, leading to a strong decrease of the mobility, since these sites cause a very long delay in the motion of the carrier. Regarding the spin diffusion, however, the situation is distinctly different. Let us, for example, consider the case $r = 1000$ and $B = 0$. At sites i with τ_i to the left of the solid line in Fig. 6.2(a), such that $r_i \equiv 1/\omega_{hf}\tau_i \gg 1$, essentially no polarization loss occurs [cf. Eq. (6.1) with r replaced by r_i]. At sites with τ_i to the right of this line, such that $r_i \ll 1$, almost immediate polarization loss occurs, but this effect is essentially the same for all these sites. For large $\hat{\sigma}$ the fraction of the latter sites, obtained by integrating $P(\tau)$ from the solid line to the right, converges to $\sim 1/r^{1/2}$. This means that on average the spin polarization disappears in $\sim r^{1/2}$ hops. Since at small E diffusion of carriers is dominant over drift one expects $l_s \sim (r^{1/2})^{1/2} \sim r^{1/4}$. The dashed line in Fig. 6.2(b) indicates this expected power law, to which the results indeed converge (for numerical reasons we took a small but finite E). We studied $P(\tau)$ as a function of E and found a similar convergence to a universal distribution with increasing $\hat{\sigma}$, where the power-law behavior gradually changes to an exponential behavior

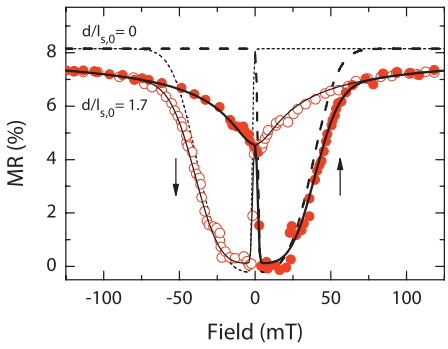

Figure 6.3: Full curves: fit of the model discussed in the main text to the experimental magnetoresistance (MR) traces taken from Fig. 3(b) of Ref. 149 (symbols). Dashed curves: results neglecting spin relaxation. Thick/thin lines: up/down field-sweep, also indicated by the arrows.

$P(\tau) \sim \exp(-\omega_{\rm hop}\tau)$ with increasing E.

In Fig. 6.2(c) we plot $l_{\rm s}$ at small E as a function of magnetic field B, for $r = 1000$. For $B > B_{\rm hf}$ we observe an important B-dependence, which again converges to a power law for increasing $\hat{\sigma}$. The analysis now goes as follows. Let us, for example, take $b = B/B_{\rm hf} = 10$. From Eq. (6.1) (again replacing r by $r_i \equiv 1/\omega_{\rm hf}\tau_i$) it follows that if $r_i \gg b$, i.e. to the left of the dash-dotted line in Fig. 6.2a, basically no polarization loss takes place. To the right of this line *partial* polarization loss takes place with $1 - \lambda \sim 1/b^2$, which is a consequence of the pinning effect of the Zeeman term discussed above. A similar argument as above now leads to the expectation $l_{\rm s} \sim b^{3/4}$ in the diffusive regime, which is seen to be very well obeyed. Together with the above power-law dependence on r this allows us to estimate $l_{\rm s}$ for general values of $r \gg 1$ and b for the case of large $\hat{\sigma}$ and small E.

6.4 Modeling a spin valve

We now undertake a comparison between our theory and experimental results, as far as they are available at the moment (see Sect. 1.3.1). We have no information about the hopping frequencies of the OS used in the spin valves of Refs. 35, 149, and 68: sexithienyl, tris-(8-hydroxyquinoline) aluminum (Alq_3), and poly-3-hexylthiophene, respectively. Since the mobilities in these materials are higher than those of the PPV-derivatives investigated in Ref. 102, we expect that the hopping frequencies are such that $r > 1000$. A calculated value of $\sigma = 0.26$ eV for the energetic disorder of electrons in Alq_3 [88] leads to $\hat{\sigma} \approx 10$ at room temperature, which is clearly in the strong-disorder limit. We can conclude that with a typical value $a \approx 1$ nm the spin-diffusion lengths of about 10–100 nm found in Refs. 35,68,149 and recently confirmed with muon spin-resonance studies [40] are compatible with our results.

Very interestingly, inspection of the experimental GMR traces in Refs. 149 and 68, both using $La_{0.67}Sr_{0.33}MnO_3$ (LSMO) and Co as electrodes, reveals that in the up and down field-sweeps the resistance as a function of B changes considerably already *before* the magnetization of the soft layer (with the weaker coercive field) is reversed (in Sect. 1.2 a basic introduction of GMR traces is given). This may point at a source of

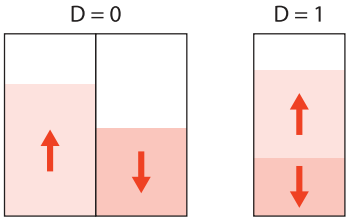

Figure 6.4: Filling of the intermediate reservoir with either separate baths for spin up and spin down ($D = 0$) or one shared bath ($D = 1$).

magnetoresistance other than the switching of the ferromagnetic layers and we propose that this is the magnetic-field dependence of the spin-diffusion length predicted by our theory. To illustrate its effect on the GMR traces, we simulated such traces using a simple phenomenological model, which will be described in more detail in the next section. We fitted the resulting GMR traces to experimental data of Ref. 149, see Fig. 6.3. The fitting procedure, which will be described in Sect. 6.4.2, yields a ratio of the spin-diffusion length and the device thickness at zero field, $l_{s,0} \approx 1.7d$, and $B_{hf} \approx 5.7$ mT, the latter being indeed a typical value for the random hyperfine field. The fact that the curve for $d/l_{s,0} = 0$, which describes the case without spin relaxation, deviates strongly from the experimental data demonstrates that the MR before zero field cannot be explained assuming an injected spin polarization proportional to the measured electrode magnetization.

6.4.1 Phenomenological device model

In order to relate the spin-diffusion length l_s, and in particular its magnetic-field dependence, to the magnetoresistance (MR) traces measured in experiments, we employ a phenomenological approach. For a very simple system we derive an explicit expression for the MR versus applied magnetic field in the presence of spin relaxation within the spacer layer. Rather than using this explicit, model-dependent expression, we suggest a more general equation. We verified that results for different models and under different conditions can indeed be mapped onto the general equation, when introducing a model-dependent adjustment parameter.

As to the specific case treated here, we consider a system of two electrodes with spin polarizations P_1 and P_2, with an intermediate reservoir (representing the organic spacer layer), and restrict ourselves to a low temperature case, where charge carriers only hop from electrode 1, via the reservoir, to electrode 2, while backward hops are neglected. Then, from the first electrode spin-up and spin-down carriers can hop into electronic states in the reservoir, of which the occupation by spin-up and spin-down carriers is given by N_{up} and N_{do}, respectively. In the reservoir, spins are mixed at a rate α. For the reservoir two assumptions can be made: either spin-up and spin-down carriers have separate baths ($D = 0$), or they share the same bath ($D = 1$), see Fig. 6.4, the latter meaning that $N_{up} + N_{do}$ cannot be larger than one (double occupancy of sites in the reservoir is excluded). Finally, carriers can hop from the reservoir to electrode 2. The spin-integrated density of states in both electrodes, as well as the transition rates from electrode 1 and to electrode 2, are assumed to be equal and for simplicity they are

taken as unity. For arbitrary value of D, we then find two rate equations,

$$\begin{aligned}\frac{\mathrm{d}N_{\mathrm{up}}}{\mathrm{d}t} =& \frac{1}{2}\left(1+P_1\right)\left(1-DN_{\mathrm{do}}-N_{\mathrm{up}}\right)+\\ & \alpha\left(N_{\mathrm{do}}-N_{\mathrm{up}}\right)-\frac{1}{2}\left(1+mP_2\right)N_{\mathrm{up}}=0,\\ \frac{\mathrm{d}N_{\mathrm{do}}}{\mathrm{d}t} =& \frac{1}{2}\left(1-P_1\right)\left(1-N_{\mathrm{do}}-DN_{\mathrm{up}}\right)+\\ & \alpha\left(N_{\mathrm{up}}-N_{\mathrm{do}}\right)-\frac{1}{2}\left(1-mP_2\right)N_{\mathrm{do}}=0,\end{aligned} \tag{6.2}$$

where m indicates whether the magnetization of the electrodes are parallel (+1) or anti-parallel (−1). By solving N_{up} and N_{do} from this set of equations the current through the system is found,

$$\begin{aligned}J_{D=1} =& \frac{P_2^2-4\alpha-1}{P_2^2+2mP_1P_2-12\alpha-3},\\ J_{D=0} =& \frac{P_1^2+P_2^2-4\alpha-2}{P_1^2+2mP_2P_1+P_2^2-8\alpha-4},\end{aligned} \tag{6.3}$$

where the assumption is made that the polarizations of the electrodes are always either parallel or anti-parallel ($m^2=1$).

In order to get a simple expression useful for fitting MR data, we expand Eq. (6.3) in the two lowest orders of P_1 and P_2,

$$\begin{aligned}J_{\mathrm{simple},D=1} =& \frac{1}{3}-\frac{2}{9}\left(P_1P_2m-P_2^2\right)\frac{1}{4\alpha+1},\\ J_{\mathrm{simple},D=0} =& \frac{1}{2}-\frac{1}{4}\left(P_1P_2m-\frac{1}{2}P_1^2-\frac{1}{2}P_2^2\right)\frac{1}{2\alpha+1}.\end{aligned} \tag{6.4}$$

This result is compatible with a more general expression for the current,

$$J_{\mathrm{general}} = \mathrm{const.} + \left(Am-B\right)\exp\left(-\frac{d}{l_{\mathrm{s}}}\right), \tag{6.5}$$

with parameters A and B giving information about the spin polarization at the injection and collection step. Also, we see that the ratio B/A depends on details of the implementation, in this specific case the value of D. In order to match our experimental situation with an MR that decays exponentially as a function of spacer layer thickness d, the denominator in Eq. (6.4), including the α-dependence, is replaced by the exponential factor. Note that this is a very pragmatic step, replacing spin relaxation in the time domain (described by α), by a decaying spin density in real space, where l_{s} corresponds to the experimentally or theoretically determined spin-diffusion length. It is not difficult to derive explicit expressions for modifications of the model, e.g. including backward hopping at finite temperatures, or considering several intermediate reservoirs in series. For all cases we investigated, we found the final structure of the solution to be identical to Eq. (6.5).

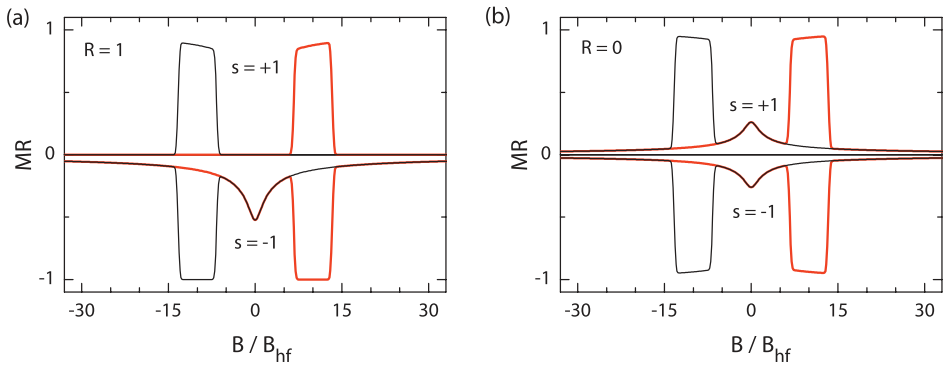

Figure 6.5: MR(B) curves simulated with Eq. (6.6). (a) Using $R = 1$, forward (thick, red) and backward (thin, black) are plotted for both $s = +1$ and $s = -1$. (b) Similar plots, but using $R = 0$. For all curves we use $d/l_{s,0} = 0.7$.

6.4.2 Fitting of the experimental data to the model

To illustrate the effect of a magnetic-field dependent spin-diffusion length on the MR traces, we simulate such traces for spin valves using the phenomenological model derived in the previous section. The general expression for the current [Eq. (6.5)] is rewritten to an expression for the MR (assuming MR ≈ −MC, with MC the magnetoconductance),

$$\mathrm{MR}(B) = \mathrm{MR}_{\max} \cdot \frac{1}{2}[R - sm(B)] \exp[-d/l_s(B)] + \mathrm{MR}_0, \tag{6.6}$$

with $\mathrm{MR}_{\max}$ the MR when neglecting spin relaxation, d the thickness of the organic spacer, and $\mathrm{MR}_0 = \mathrm{MR}_{\max} \cdot \frac{1}{2}(s - R)$ a vertical shift. $R = B/A$ is a model dependent parameter, including details of the device like the ratio of the polarizations of the electrodes; the case $R = 1$ represents the common case of no spin accumulation for equal polarizations, while $R = 0$ gives direct tunneling between electrodes without carriers accumulating in an intermediate reservoir, i.e. a simple Jullière approximation. For $s = +1$ (-1) these polarizations have equal (opposite) sign in parallel alignment of the magnetization of the electrodes. The magnetic switching characteristics of the electrodes are captured by $m(B)$, with $m = +1$ (-1) describing parallel (anti-parallel) magnetic orientation. The magnetic-field dependence of the spin-diffusion length l_s is described by

$$l_s(B) = l_{s,0}\left[\sqrt{1 + (B/B_0)^2}\right]^{3/4}, \tag{6.7}$$

with $B_0 = 2.3B_{\mathrm{hf}}$, as fitted to the predictions of our theory in the diffusive regime ($E \ll \sigma/ea$), see Fig. 6.6(a). The value of $l_{s,0}$ depends on the precise value of $\omega_{\mathrm{hop}}/\omega_{\mathrm{hf}}$, which is unknown in the experiments. Therefore, $l_{s,0}$ is treated as a parameter.

In Figure 6.5 we show MR(B) curves simulated with Eq. (6.6) for different values of R and s. These curves give a better impression of the model than the fit in Fig. 6.3, where part of the features are obscured by the broad switching behavior. For $s = +1$ and $s = -1$ a positive and a negative MR are obtained, respectively. For $R = 1$, no change

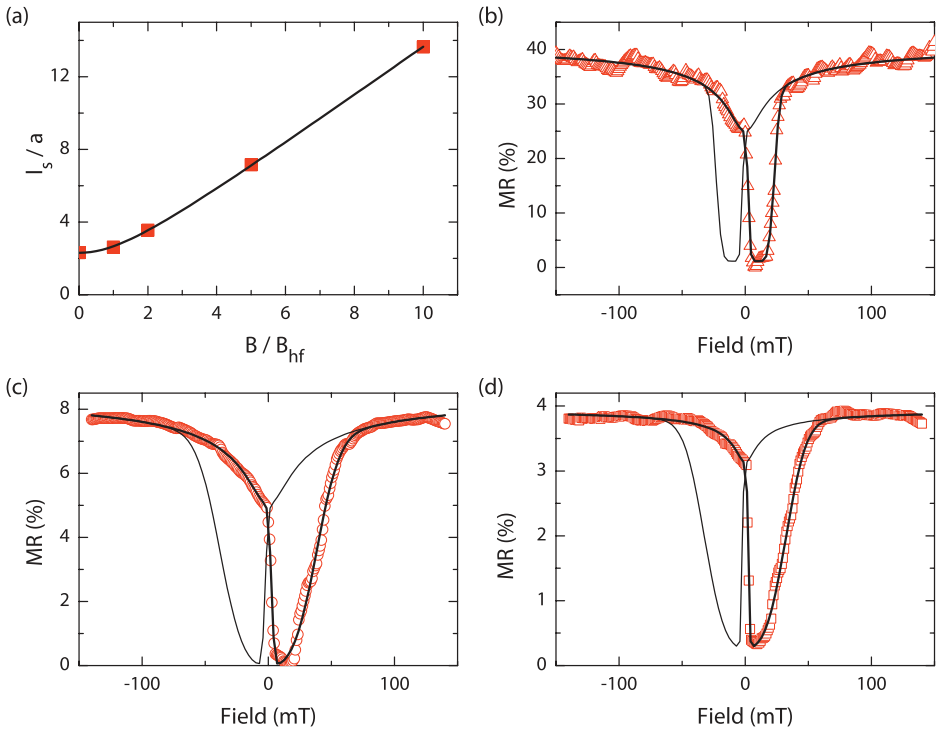

Figure 6.6: (a) Fit to Eq. (6.7) (line) of the magnetic-field dependence of the spin-diffusion length to the Monte-Carlo results (symbols) for $Eea/\sigma = 0.1$, $\hat{\sigma} = 6$ (strong disorder) and $\omega_{\mathrm{hop}}/\omega_{\mathrm{hf}} = 1000$ (fast hopping). Resulting in $B_0 = 2.3B_{\mathrm{hf}}$ and $l_{\mathrm{s},0} = 2.3a$. (b–d) MR traces from Ref. 149, fitted with Eq. (6.6), with $R = 1$. (b) fit to Fig. 2(a) (130 nm, low bias), yielding $l_{\mathrm{s},0} \approx 1.9d$ and $B_{\mathrm{hf}} \approx 4.7$ mT, (c) fit to Fig. 3(b) top-right (160 nm, 2.3 mV), yielding $l_{\mathrm{s},0} \approx 1.9d$ and $B_{\mathrm{hf}} \approx 6.0$ mT, and (d) fit to Fig 3(b) bottom-left (160 nm, −400 mV), yielding $l_{\mathrm{s},0} \approx 4d$ and $B_{\mathrm{hf}} \approx 3$ mT.

due to the hyperfine fields is present in the case of parallel alignment of the magnetization directions [Fig. 6.5(a)], while for $R = 0$, the change is symmetric [Fig. 6.5(b)]. For intermediate values of R, a mixture of these two cases can be found.

Using Eq. (6.6) we fitted all the MR traces in Ref. 149 and in its supplementary information. Several fits are shown in Figs. 6.3 and 6.6(b–d). The backward sweep of the results in Ref. 149 is mirrored and averaged with the forward sweep. For $m(B)$, we used a product of two error functions centered at the coercive field to match the rounded switching of the respective electrodes, as observed in the Magneto-Optical Kerr Effect (MOKE) data of Ref. 149. The coercive fields of the LSMO electrode obtained from the fits of the MR traces are close to the values from the MOKE data. The values for the Co electrode are larger, but this is not unexpected as Co on Alq_3 can show varying values. For a system displaying an opposite spin polarization for the parallel alignment of the magnetization directions $s = -1$, as is the case here, R mostly determines the slope in the narrow B-region where the electrodes have opposite magnetization, i.e. where the soft magnetic electrode has already switched, but the other electrode not yet. Because of the strongly rounded switching of the Co electrode, the value for R is therefore hard

to determine, *but this hardly affects the quality of the fits*. For the sake of simplicity, in Figs. 6.3 and 6.6(b–d) a value of $R = 1$ is chosen, but treating it as a free parameter gives almost identical results. We note that the latter is certainly *not* the case in systems with 'ordinary' spin polarizations ($s = 1$), in which the detailed shape of the MR trace at negative fields, before switching of the soft electrode, strongly depends on the value of R. Fig. 6.3 shows that this predicted $l_s(B)$ accurately reproduces the shape of MR(B) in the region before switching of the soft layer, with a minimum number of parameters.

Our theory predicts a rather weak dependence of l_s on the relative disorder strength $\sigma/k_B T$ and hence on temperature, in agreement with experiments.[34,144,149] In the experiments with LSMO as one of the electrodes the GMR effect decreases significantly above $T \approx 100$ K, but this can be fully attributed to a reduction of the spin polarization of the injected current.[34,144] Finally, it is important to note that in the experiments the GMR effect rapidly disappears with growing bias voltage[34,144,149] on a voltage scale (~1 V) that corresponds in our theory to electric fields for which $eEa/\sigma \ll 1$. At such fields, l_s has saturated to its value at $E = 0$. Therefore, our view is that the measured bias-voltage dependence is not caused by a dependence of l_s on the electric field. This view is supported by experiments that find an asymmetric behavior in the bias dependence of organic spin valves depending on which of the two unequal electrode materials is positively biased.[144,149] Several possible explanations for the steep decrease of spin-valve efficiency with increasing bias have been suggested,[144] but it is clear that this issue requires much further study. If efficient spin injection can be realized with high biases such that $eEa/\sigma > 1$, our theory predicts greatly enhanced spin-diffusion lengths of the order of several hundreds of nanometers, up to even millimeters [see Fig. 6.1(a)].

6.5 Conclusion

Concluding, we have presented a theory for spin diffusion in disordered organic semiconductors with hyperfine coupling, based on a combination of incoherent carrier hopping and coherent spin precession in a random effective magnetic field. We obtain spin-diffusion lengths of the correct magnitude that depend rather weakly on temperature, but considerably on the applied magnetic field, in agreement with experiments on spin valves.

7 Angle dependent spin-diffusion length

For a spin valve to show a magnetic response, one of the critical conditions is that the thickness should be less than or comparable to the spin-diffusion length in the spacer layer. In Ch. 6, we introduced a model for spin diffusion in organic semiconductors. In addition to measuring magnetoresistance in an (organic) spin valve, a more rigorous test of spin transport through the spacer layer can be achieved by manipulation of the spins during transport. This can be done by applying a magnetic field under an angle with the spin polarization, causing a coherent precession of the spins, resulting in a modulation of the spin valve signal as a function of field strength. This so called Hanle effect has been extensively studied in many inorganic materials. In this Chapter, we extend the model from Ch. 6 and discuss the Hanle effect in disordered organic materials. We find results that differ significantly from high mobility (inorganic) semiconductors, due to the specific waiting-time distribution resulting from the disorder. Using the obtained angle and field dependence of the spin-diffusion length, we discuss the conditions for a successful Hanle experiment in organic semiconductors.[*]

7.1 Introduction

Organic semiconductors are believed to be very interesting candidates for spintronics applications because of the predicted long spin lifetimes, see Sect. 1.3. In absence of significant spin–orbit coupling due to the low weight atoms, the main source of spin scattering is believed to be the random hyperfine fields.[22,92] In recent years, several reports have appeared on spin valves with an organic spacer layer, see Sect. 1.3.1. In a spin valve, spin polarized carriers are injected by a ferromagnetic electrode, transported through the layer and detected by another ferromagnetic electrode. One important requirement to see a magnetoresistance (MR) signal, i.e., different resistance for parallel and anti-parallel alignment of the magnetization of the electrodes, is that the spin-diffusion length is comparable to or larger than the spacer thickness. Although ex-

[*] In Preparation: *The effect of magnetic field orientation on the spin-diffusion length in organic semiconductors* W. Wagemans, F.W.A. van Oost, S. Wouters, A.J. Schellekens, P.A. Bobbert, and B. Koopmans.

periments show the expected shape of the MR curves, doubt still exists whether they are really the result from spin transport through the full layer, or from tunneling through thin regions.[139] Next to showing spin valve behavior, a more rigorous test for spin transport through the (organic) layer can be performed by manipulating the spins during transport. One common way to do this is by applying a magnetic field perpendicular to the polarization direction, causing precession of the spins. Due to this precession, in combination with dephasing, the signal of the spin valve is modulated, which is called the Hanle effect.[30,58,60,66] This effect would be absent in the case of direct tunneling.

Previously, we developed a model for spin diffusion in disordered organic semiconductors,[22] see Ch. 6. Because of the energetic disorder, the carriers are incoherently hopping through the device while their spins perform a coherent precession in an effective magnetic field, which is the sum of the externally applied field and random hyperfine fields from the hydrogen nuclei. We showed a strong dependence of the spin-diffusion length on the strength of the applied magnetic field. At low fields, the spin polarization is quickly reduced by the precession in the random hyperfine fields [Fig. 7.1(a)], resulting in a relatively short spin-diffusion length. When a large external field is applied parallel to the polarization direction, the spin precesses around approximately the same field at all sites and the spin-diffusion length is greatly enhanced. This magnetic-field dependent spin-diffusion length results in a modification of the typical (magneto)resistance versus magnetic field curves, where the magnetoresistance is reduced around zero field. We showed that our model can be successfully used to fit experimental magnetoresistance curves, see Fig. 6.6.

So far, we only investigated the spin transport with the external field applied parallel to the spin polarization (Ch. 6), as is the case in normal spin valve operation. Here, we describe an extension of the work, investigating the effect of applying the external field under an angle, like in a Hanle experiment. We will show that due to the random hopping caused by disorder, the oscillatory behavior typical for a Hanle experiment is suppressed by the fast loss of spin coherence. We will use these results to make predictions about Hanle measurements and spin valve operation.

7.2 Model

We study the average spin polarization of charges hopping through a landscape of localized sites under influence of an electric field. In disordered organic semiconductors, the site energies are random and follow a Gaussian density of states with a standard deviation σ.[9] Transport occurs via hopping between nearest-neighbor sites (from site i to j) with a rate[83]

$$\omega_{ij} = \begin{cases} \omega_{\text{hop}} \exp[-(\varepsilon_j - \varepsilon_i)/k_{\text{B}}T] & \text{for } \varepsilon_j \geq \varepsilon_i \\ \omega_{\text{hop}} & \text{for } \varepsilon_j < \varepsilon_i, \end{cases} \tag{7.1}$$

with T the temperature, k_{B} Boltzmann's constant, and ε_i and ε_j the on-site energies of sites i and j—with a contribution due to the electric field E added—, and ω_{hop} a prefactor containing both a phonon attempt frequency and a factor related to a wave-function overlap. The electric field is applied along the x-axis and moves the charges from the injecting electrode at $x = 0$ to the opposite electrode at $x = L$. For studying the spin

transport, the injected charges are fully spin polarized along the z-axis ($P = 1$). At each hopping site i, the spins interact with an effective magnetic field $\mathbf{B}_i = \mathbf{B}_{\mathrm{hf},i} + \mathbf{B}$, where $\mathbf{B}_{\mathrm{hf},i}$ is the random hyperfine field at the site and $\mathbf{B} = B[\sin(\theta)\hat{\mathbf{x}} + \cos(\theta)\hat{\mathbf{z}}]$ the externally applied magnetic field, which has an angle θ with the z-axis [Fig. 7.1(c)]. For the hyperfine field we assume a random field, distributed according to a three-dimensional Gaussian,[121] with standard deviation B_{hf}. In Fig. 7.1(a) and (b), we illustrate the case of $B_{\mathrm{hf}} \neq 0$ and $B = 0$—the spins precess around a different hyperfine field at each site—, and the case of $B \neq 0$, $\theta = 90°$ and $B_{\mathrm{hf}} = 0$—the spins perform a coherent precession around the external field between hops—, respectively. Clearly, both cases give a different spin signal at a distance from the electrode, as we will show in the next sections.

To study the angle dependence of the spin transport, we performed Monte Carlo simulations using a cubic grid of sites ($L/a \times 50 \times 50$), with a fixed nearest-neighbor distance a and periodic boundary conditions in the y and z direction. The sites are prepared by drawing their site energies and hyperfine fields from the corresponding distributions. After a fully polarized charge is injected, the time-dependent Schrödinger equation for its spinor is solved in between hopping events.[22] The spin precession frequency is $\omega_{\mathrm{hf}} = \gamma B_{\mathrm{hf}} \approx 10^8\ \mathrm{s}^{-1}$, with γ the gyromagnetic ratio. To link the spin transport to the charge transport, we define the ratio $r \equiv \omega_{\mathrm{hop}}/\omega_{\mathrm{hf}}$, which is on the order of 10–1000 for typical polymers.[22] In order not to loose the spin polarization within just a few hops, it is required that $r \gg 1$, which is likely the case for the semiconductors typically used for organic spin valves.† At each layer $d = x/a$, we keep track of the average spin polarization along the z-axis, p, averaging over many energetic and hyperfine disorder configurations. In our simulations we focus on $\sigma = 0.1\,\mathrm{eV}$ and $r = 1000$, unless mentioned otherwise, as these values are typical for commonly used organic semiconductors.[22] For different σ, a scaling with E and T, keeping E/σ and $\sigma/k_{\mathrm{B}}T$ constant, can be applied. Moreover, we focus on room temperature, $k_{\mathrm{B}}T = 25\,\mathrm{meV}$, and for convenience define a reduced magnetic field $b \equiv B/B_{\mathrm{hf}}$, and use a as a unit of length.

7.3 Results

First, the case of a high electric field ($Ea/\sigma \to \infty$) is discussed. In this limit, effects of the disorder are negligible ($Ea \gg \sigma$) and only downfield hops occur ($Ea \gg k_{\mathrm{B}}T$). Figure 7.2(a) shows p as a function of the position in the device for $b = 3$, showing three different angles of the applied magnetic field. At $\theta = 0$, the field is aligned with the spin polarization and the same results are obtained as in our previous work,[22] see Ch. 6, where the reduction of p is caused by precession in the random hyperfine fields [Fig. 7.1(a)]. At $\theta = 90°$, the field is perpendicular to the polarization and p shows a damped oscillation around zero. At intermediate angles, oscillations occur around a decaying baseline. The oscillations are caused by a coherent precession of the spins around the external field [Fig. 7.1(b)]. The decay of the amplitude of the oscillations is a result of both loss of spin polarization due to the random hyperfine fields and loss of spin coherence due to dephasing of the precession. We find that p can be fitted with:

$$p = e^{-d/l_{\mathrm{s}}}\left[\cos^2(\theta) + \sin^2(\theta)e^{-d/l_{\mathrm{sc}}}\cos(2\pi d/\lambda_{\mathrm{sc}})\right], \tag{7.2}$$

†Note however, that for OMAR—which is observed in the same materials—slow hopping is needed, $r \leq 1$. One explanation for this apparent discrepancy could be the large spread in waiting times, see Fig. 6.2.

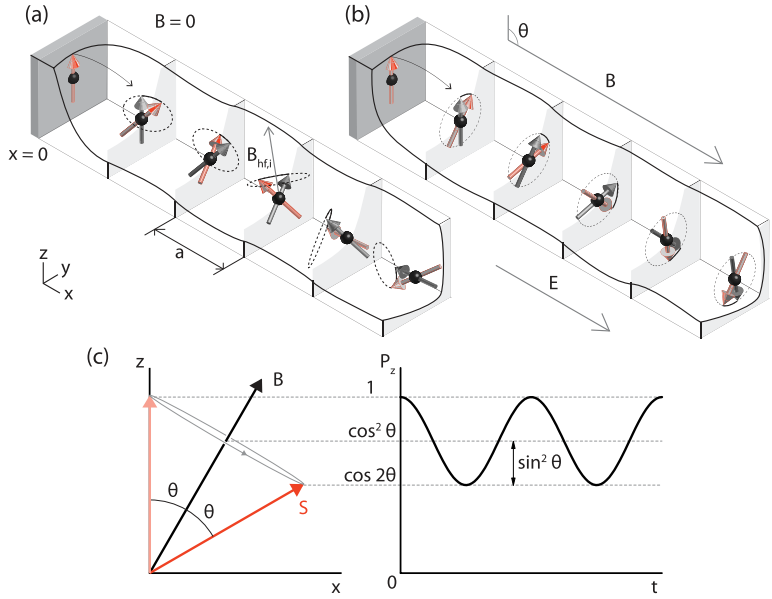

Figure 7.1: (a,b) Spin transport, with spin injection at $x = 0$ and precession in (a) random hyperfine fields, and (b) a perpendicular external field. (c) Spin S precessing around a magnetic field B which has an angle θ with the z-axis. The resulting oscillation in the z-component of the polarization is shown with the equilibrium and amplitude values.

with l_s the spin-diffusion length (as can be obtained at $\theta = 0$), l_{sc} the coherence length of the spin precession and λ_{sc} the period of the spin precession. The $\cos^2(\theta)$ and $\sin^2(\theta)$ terms follow from simple geometric considerations as sketched in Fig. 7.1(c); the maximum polarization along the z-axis is 1 and the minimum is $\cos(2\theta)$, giving an amplitude of $\sin^2(\theta)$ and an offset of $\cos^2(\theta)$. Fitted curves are shown in Fig. 7.2 and match Eq. (7.2) very well. The separate roles of the hyperfine fields and the dephasing are illustrated by performing the same simulation as in Fig. 7.2(a), but now with the influence of the hyperfine fields disabled ($B_{hf} = 0$), see Fig. 7.2(b). In this case, the baseline of the oscillation is constant and the decay of the oscillations is slightly slower (as $l_s \to \infty$), while the period of the oscillation is not affected.

In the case of $Ea \lesssim \sigma$, the effects of disorder are no longer negligible. Figures 7.2(c) and (d) show p as a function of the position in the device for $Ea/\sigma = 1$ and $Ea/\sigma = 0.1$ respectively, both at small field ($b = 0.5$, circles) and large field ($b = 5$, squares) for $\theta = 0°$ (open symbols) and 90° (closed). At 90° and large B, a fast decrease of p is observed, while for a small field the effect of coherent precession is strongly reduced. For $Ea \to \infty$ clear oscillations could be observed, but these are much less pronounced when E becomes comparable or smaller than σ. This dependence on disorder can be seen more clearly from Fig. 7.3(a), where l_s, l_{sc} and λ_{sc} are plotted as a function of E, with $\sigma = 0.1$ eV. For small and large E, these lengths are constant, while a transition occurs around $E = \sigma$. At low E, p is dominated by l_{sc} and no oscillations are visible [Fig. 7.2(d)], while at large E, λ_{sc} is smallest and oscillations are clearly visible [Fig. 7.2(a)]. Surprisingly, we observe

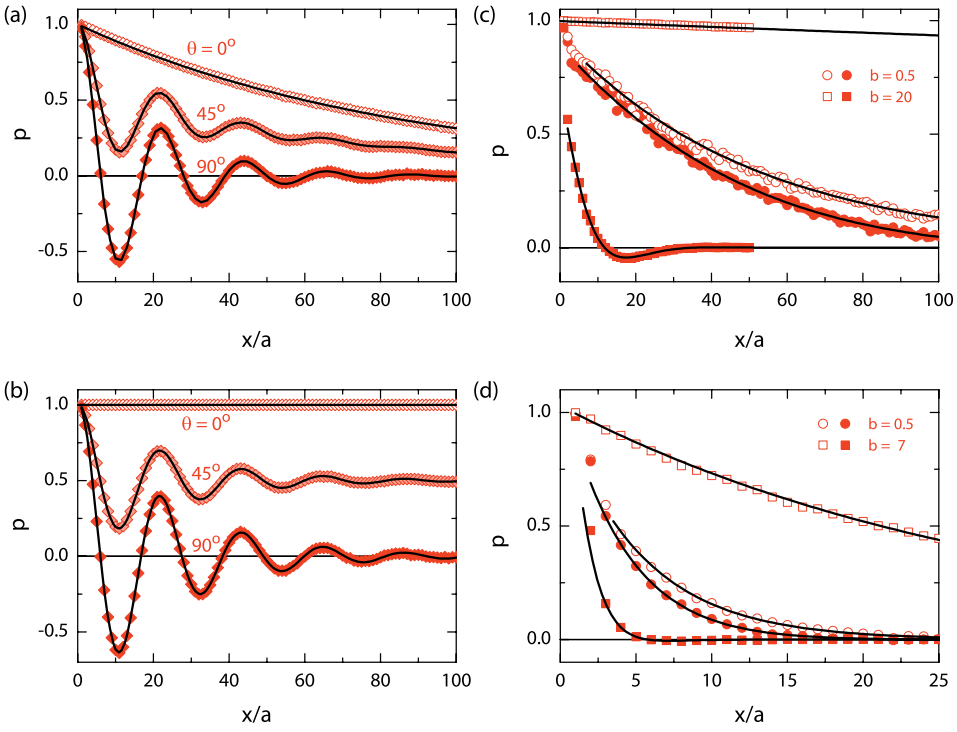

Figure 7.2: Spin polarization as a function of the position in the device for $\theta = 0°$ (open symbols), 45° (grey), and 90° (black), with (a) $Ea \to \infty$, $b = 3$, $\sigma = 0.1\,\text{eV}$, and $r = 10$; (b) same parameters as (a), but with $B_{\text{hf}} = 0$; (c) $Ea = 0.1\,\text{eV}$, $b = 0.5$ (circles) and 20 (squares), $\sigma = 0.1\,\text{eV}$, and $r = 1000$; (d) $Ea = 0.01\,\text{eV}$, $b = 0.5$ (circles) and 7 (squares), $\sigma = 0.1\,\text{eV}$, and $r = 1000$. The lines are fits using Eq. 7.2.

that the ratio l_s/l_{sc} is constant (not shown), hinting that these lengths have a common source.

Next, we look at the effect of the magnitude of a perpendicularly applied field, at constant E. Figure 7.3(b) shows that it acts to reduce l_{sc} and λ_{sc}, while it increases l_s. The finite value of l_s at $B = 0$ and increase for larger B was also found in our previous work, see Ch. 6, where we looked at $\theta = 0°$, but according to Eq. (7.2) we should get the same results.[22] The trend of l_{sc} and λ_{sc} is similar at large B, but they show a clearly different behavior at small B, where B_{hf} is of comparable value. This influence of the random hyperfine fields on l_{sc} and λ_{sc} is tested by performing identical simulations but with $B_{\text{hf}} = 0$ (open symbols). It is clear that both l_{sc} and λ_{sc} are larger at low fields when random hyperfine fields are dominant. We believe this is due to motional narrowing.[12]

7.4 Waiting Time Analysis

To obtain insight into the dependence of l_{sc} and λ_{sc} on B and disorder, we will perform an analysis based on the waiting-time distributions for a few limiting cases. In this discussion, we assume a perpendicularly applied magnetic field and $B_{\text{hf}} = 0$. If we look at all the spins in layer d, they will each have spent a different time τ_d in the device

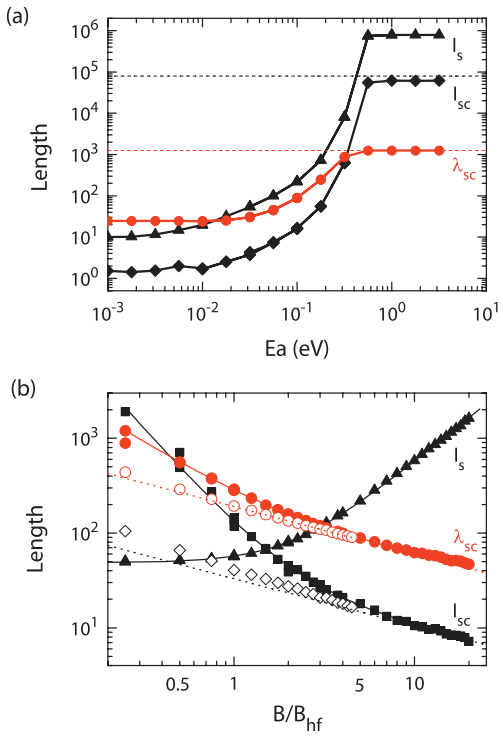

Figure 7.3: l_s, l_{sc} and λ_{sc} as a function of (a) electric field, with $b = 5$; dashed lines indicate values obtained from Eq. (7.5), (b) magnetic field, with $Ea = 0.1\,\text{eV}$; open symbols are for $B_{hf} = 0$, solid lines are empirical fits, and dotted lines are power laws, fitted at large B. Both in (a) and (b) the parameters are $\theta = 90°$, $\sigma = 0.1\,\text{eV}$, and $r = 1000$.

after being injected; τ_d being a sum of hopping times drawn from a specific waiting-time distribution with a characteristic hopping rate ω_{hop}. To obtain the polarization p at distance d, we have to average the z-component of each spin, which is proportional to $\cos(\omega_{prec}\tau_d)$. For this averaging, we need to know the specific distribution of τ_d, which is a result of the transport through the device and the waiting-time distribution. In a first order approximation, λ_{sc} will depend on the mean waiting time per layer τ_d/d compared to ω_{prec}^{-1}, and l_{sc} will depend on the width and specific shape of the τ_d distribution.

In the case of only downfield hops, with hopping times according to an exponential waiting-time distribution with a single ω_{hop}, simple expressions for l_{sc} and λ_{sc} can be found. In this case, at position d all carriers have performed d hops after being injected. At sufficiently large d, τ_d will then follow a Gaussian distribution $G(t)$ with a mean time of d/ω_{hop} and a width $\sqrt{d}/\omega_{hop}$, according to the central limit theorem. The spin polarization as a function of d is obtained by calculating the integral over all transition times:

$$\begin{aligned} p(d) &= \int G(t)\cos(\omega_{prec}t)\mathrm{d}t \\ &= e^{-\frac{1}{2}d\,\omega_{prec}^2/\omega_{hop}^2}\cos(d\,\omega_{prec}/\omega_{hop}), \end{aligned} \tag{7.3}$$

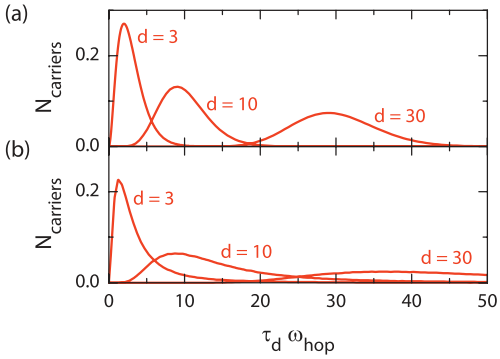

Figure 7.4: Time distributions for the sum of d waiting times from (a) an exponential distribution and (b) an algebraic distribution ($\alpha = \frac{1}{2}$).

with $\omega_{\text{prec}} \equiv \omega_{\text{hf}} b$ the Larmor precession frequency in the external magnetic field. For this simple case, by comparison with Eq. (7.2), we find,

$$\begin{aligned} \lambda_{\text{sc}} &= 2\pi\omega_{\text{hop}}/\omega_{\text{prec}}, \\ l_{\text{sc}} &= 2\left(\omega_{\text{hop}}/\omega_{\text{prec}}\right)^2, \end{aligned} \tag{7.4}$$

where $\omega_{\text{hop}}/\omega_{\text{prec}} = r/b$. The fitted l_{sc} and λ_{sc} of the simulated data for $Ea \to \infty$, as shown in Fig. 7.2(a), correspond well to this relationship. In Fig. 7.3(a), the dashed lines indicate the values for l_{sc} and λ_{sc} obtained from Eq. (7.4), showing a good match for high E.

For small d, the assumption of a Gaussian distribution is no longer valid as, in this case, τ_d is the result of only a few hops. For $Ea \gg \sigma$, the time for each hop is obtained from a single exponential distribution, which is proportional to $\exp(-t\omega_{\text{hop}})$. The sum of a number of hopping times obtained from such an exponential distribution is called a Gamma distribution. For a large number of hops, it converges to a Gaussian distribution, but deviates for a small number of samples [Fig. 7.4(a)]. Again, expressions for l_{sc} and λ_{sc} are found, now by performing the integral in Eq. 7.3 with a Gamma distribution with mean d/ω_{hop}. From a straightforward integration we find

$$\begin{aligned} \lambda_{\text{sc}} &= 2\pi/\arctan(\omega_{\text{prec}}/\omega_{\text{hop}}), \\ l_{\text{sc}} &= 2/\log[1 + \pi^{-1}(\omega_{\text{prec}}/\omega_{\text{hop}})^2]. \end{aligned} \tag{7.5}$$

For $\omega_{\text{hop}}/\omega_{\text{prec}} \gtrsim 10$, this is matching the results with the Gaussian distribution, so only for small b/r. For large b/r and large E, our simulations indeed confirm this different behavior.

If the electric field is comparable to the energetic disorder, more effects start to play a role. When selecting a site to hop to, the possible hops to neighbors all have different energy barriers due to the disorder. Therefore, instead of a single characteristic rate, for each hop a different characteristic rate has to be considered, which is the sum of the rates to the neighbors. As a result, the waiting time between hops no longer follows an exponential distribution, but will have a long, algebraic tail that can be shown to be proportional to $t^{-(1+\alpha)}$.[117] In our case $\alpha = \frac{1}{2}$ in the limit of large disorder and a

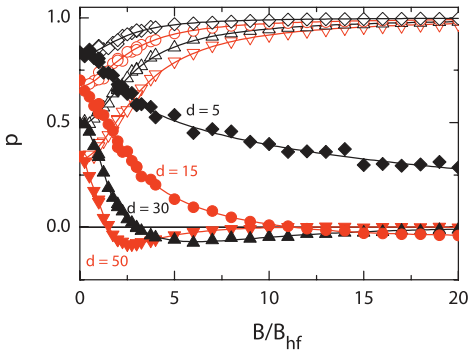

Figure 7.5: Spin polarization as a function of B at different positions d, with $\theta = 0°$ (open symbols) and $\theta = 90°$ (solid symbols). The used parameters are $Ea = 0.1\,\text{eV}$, $\sigma = 0.1\,\text{eV}$ and $r = 1000$. The lines are guides to the eye.

Gaussian density of states.[22] For this distribution, no trivial expression can be found for τ_d. Therefore, we employ a simple one-dimensional model where we explicitly assume hopping times to follow a distribution $\propto t^{-(1+\alpha)}$. We draw many random waiting times from this distribution in order to calculate p at each position [see Fig. 7.4(b) for several τ_d distributions]. For large $\omega_{\text{hop}}/\omega_{\text{prec}}$ (small b) and $\alpha = \frac{1}{2}$, we empirically find the limiting cases,

$$\begin{aligned} \lambda_{\text{sc}} &\propto (\omega_{\text{hop}}/\omega_{\text{prec}})^{\frac{1}{2}}, \\ l_{\text{sc}} &\propto (\omega_{\text{hop}}/\omega_{\text{prec}})^{\frac{1}{2}}. \end{aligned} \tag{7.6}$$

Using this simplified model, we can also assume that the carriers on average execute several hops in the layer before going to the next one, thereby simulating disorder. This does not change the final slope for large $\omega_{\text{hop}}/\omega_{\text{prec}}$, but the convergence is slower, which is most pronounced for λ_{sc}, giving an apparently smaller slope at smaller values of $\omega_{\text{hop}}/\omega_{\text{prec}}$. The resulting magnetic-field dependence ($\propto B^{-\frac{1}{2}}$) is illustrated by the dotted lines in Fig. 7.3(b), which are indeed a decent match when $B \gg B_{\text{hf}}$, and an even better match when $B_{\text{hf}} = 0$.

So far, we have found different oscillatory behavior of p, depending on whether disorder is important. For strong disorder, l_{sc} dominates the obtained results. By analyzing the waiting-time distributions, we found relationships for l_{sc} and λ_{sc} in the different regimes. In the next sections we will use these relationships to make predictions about possible experiments.

7.5 Hanle Experiment

In a typical Hanle experiment, the polarization is electrically detected at a fixed d while changing the magnitude of the perpendicularly applied magnetic field.[30,58,60,66] In such measurements, the signal is proportional to the polarization at the detecting electrode. Therefore, we plot p as a function of field at four different thicknesses [Fig. 7.5]. With $\theta = 0°$ (open symbols), an increase of l_{s} with field is observed, corresponding to the enhancement of l_{s} by B. For $\theta = 90°$ (solid symbols), at small d, p slowly decays

and no negative values are observed. With increasing d, p decays more quickly and a negative dip becomes visible. At smaller electric fields, this negative dip disappears completely, as both l_s and l_{sc} become smaller than λ_{sc} [Fig. 7.3(a)].

The main difference between Hanle experiments on most inorganic materials and organic semiconductors is the disorder in the latter. In the former, a Gaussian distribution is usually assumed for τ_d,[30] which is equivalent to our analysis with $Ea \to \infty$. Thus in that case, we expect l_{sc} and λ_{sc} to depend on the magnetic field as $(r/B)^2$ and r/B, respectively [Eq. (7.4)]. Moreover, for $r/B > \pi$ (which is typically the case in these high mobility materials), we find that $\lambda_{sc} < l_{sc}$ resulting in clear oscillations in the signal. In disordered materials, we find a $(r/B)^{\frac{1}{2}}$ dependence for both l_{sc} and λ_{sc}, with $\alpha = \frac{1}{2}$ [Eq. (7.6)]. For $0 < \alpha < 1$, usually $\lambda_{sc} > l_{sc}$, resulting in no or few oscillations to be observable.

These simulations show that it should be possible to perform successful Hanle measurements on spin transport in organic semiconductors. With high electric fields the signals should be even observable for large thicknesses. However, for this, proper injection at high bias should first be achieved as in the current experiments the spin-injection efficiency seems to be reduced at high bias. Due to the high disorder, we do not expect pronounced oscillatory behavior.

7.6 Spin Valves

By changing θ, we can control the total spin polarization at d [Eq. (7.2)], thus giving us a handle to modulate the signal of an organic spin valve. In Ch. 6, we have shown that one of the effects of a magnetic-field dependent spin-diffusion length is that the magnetoresistance curves [MR(B)] will be modified, see Fig. 6.5 on p. 75.[22] At low magnetic field, l_s is smaller than at large magnetic field, leading to a reduced signal around zero field, with a specific shape. Using the simple model we previously developed to predict the shape of MR(B) curves, we will now show the effect of rotating the sample. When we go from a spin-valve signal ($\theta = 0°$) to a Hanle signal ($\theta = 90°$). Here, it is assumed that due to the high anisotropy of the thin film electrodes, the magnetization will not tilt out of the plane. Rotating the field will cause the apparent coercive fields of the electrodes to increase with a factor $1/\cos(\theta)$, because only the component of the field in the plane of the sample causes the switching. In addition, the spins will precess around the constant external field, reducing the spin correlation as discussed before. As can be seen from Eq. (7.2), rotating the magnetic field out-of-plane will reduce the polarization reaching the other electrode.

Previously, we developed a very basic model to describe the response of a spin valve, including a magnetic-field dependent l_s, see Ch. 6.[22] Here, we use the same model but instead of only including the influence of B on l_s, we include Eq. (7.2) to study the angle dependence. In the model we use two ferromagnetic electrodes with the organic layer represented by a single intermediate reservoir. Loss of spin polarization is described by spin mixing in the reservoir. This model leads to a generic equation for the current, in which a model parameter R is introduced that contains information about the ratio of the polarizations and spin accumulation in the layer. For $R = 1$, spin accumulation is absent for equal polarizations, and $R = 0$ is comparable to direct tunneling between the electrodes. We parameterized the curves for l_s, l_{sc} and λ_{sc} as a function of B [Fig. 7.3(b)]

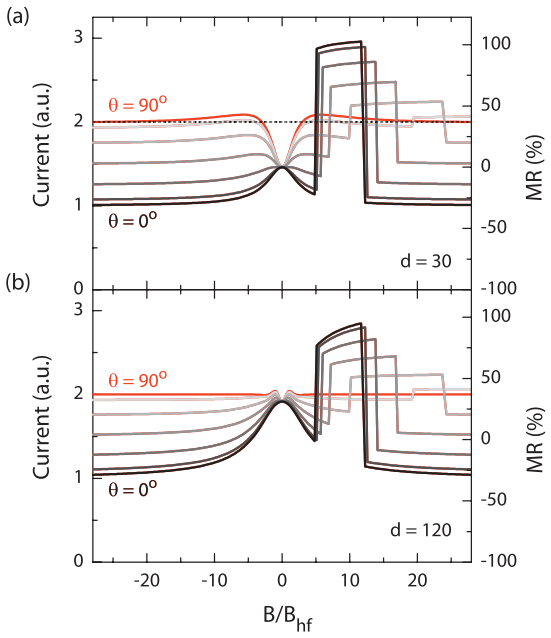

Figure 7.6: Predicted MR of a spin valve as a function of B with l_s, l_{sc} and λ_{sc} dependencies as in Fig. 7.3(b), for different angles $\theta = 0$–90°, with steps of 15°. The thickness of the organic layer is (a) $d = 30$ and (b) $d = 120$. The used parameters are $Ea = 0.1\,\text{eV}$, $\sigma = 0.1\,\text{eV}$, $r = 1000$, and $R = 1$.

and used these as input for the calculations.

In Fig. 7.6, we show MR(B) curves for increasing magnetic field, for two different thicknesses (see Sect. 1.2 for a general discussion of spin valves). At $\theta = 0^\circ$, we observe the spin valve signal, with the typical shape around $B = 0$ due to the magnetic-field dependence of l_s (see Fig. 6.5 on p. 75). At $\theta = 90^\circ$, a Hanle measurement is obtained, similar to Fig. 7.5. The dashed line indicates the current if no spin polarization were present. For $\theta = 90^\circ$, the current approaches this line as the coherent precession destroys the spin polarization. In the case of the thin spin valve [Fig. 7.6(a), $\theta = 0^\circ$], considerable spin polarization is still left at $B = 0$, while this is not the case in the thick spin valve [Fig. 7.6(b), $\theta = 0^\circ$]. Intermediate angles give a combination of the Hanle signal at an angle and a spin-valve signal that switches at increased B. These simulations show that a rotation of the spin valve can be used to separate the effects of the spin transport from spurious effects from switching of the electrodes.

7.7 Conclusion

In conclusion, we have shown how spin transport in disordered organic semiconductors can be modified by applying a magnetic field under an angle with the spin polarization. At low electric fields, because of incoherent hopping due to disorder and precession in random hyperfine fields, a different Hanle effect is found than at high electric field. The last case is comparable to experiments on most inorganic materials. We show that Hanle experiments in organic semiconductors should be possible, but no pronounced oscillatory behavior is expected.

Extensions of the experiments and models

8

This chapter gives an overview of three promising extensions of the topics covered in this thesis. First, an extension of the two-site bipolaron model (Ch. 3) is discussed, in which physical parameters like the energy of sites and the electric field are used instead of abstract hopping rates. When aiming at understanding OMAR behavior, for instance as function of temperature and applied bias, this model offers a convenient alternative to the 'black box'-like Monte Carlo simulations. Second, an alternative analysis of the measured MC(B) line shapes is introduced, using an equation that takes both the role of the hyperfine fields and the broadening induced by the model into account. This equation could be used to make more quantitative comparisons between measurements using different materials. Third, a new experiment is suggested in which a spin-polarized current is combined with OMAR, which could validate the bipolaron model and prove spin injection. We model OMAR in a device with a single ferromagnetic electrode and show that an angle dependence and line shape are obtained that are different from OMAR in a regular device.

8.1 Extending the two-site bipolaron model with physical parameters

In Ch. 3 we have introduced an analytical approach for investigating the bipolaron model. We reduced the transport to the critical blocking step in the transport by looking at two sites, where the second site already contained one carrier and thus acted as a blocking site. The model was successful in obtaining a magnetoconductance and reproducing the experimentally observed line shapes. However, abstract rate parameters were used and only forward hopping was considered. On the other hand, Bobbert *et al.* used Monte Carlo simulations to investigate the influence of magnetic field dependent bipolaron formation under more realistic conditions by using a large grid of sites with random energies and hyperfine fields in which they monitored the transport of carriers.[20] Although such Monte Carlo simulations allow the direct input of physical parameters like electric field, temperature and disorder strength, they can be time consuming to perform and act more like a black box. In this section, we give an outlook for an adapted two-site model in which physical parameters are introduced and present

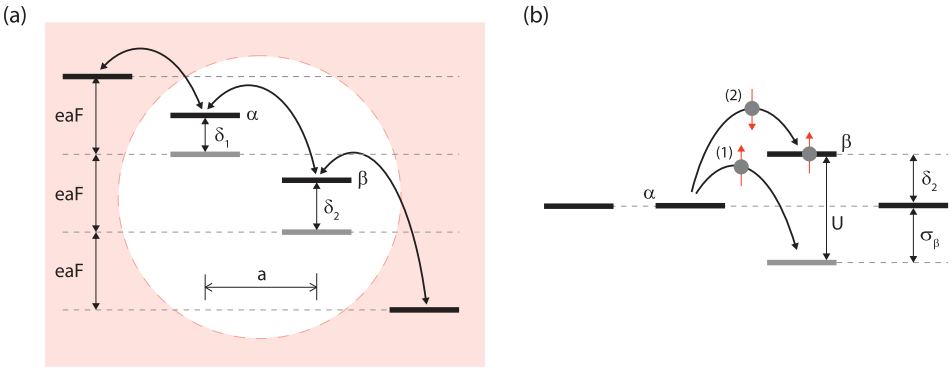

Figure 8.1: (a) Energy alignment of sites α and β with respect to the sites in the environment. The electric field F determines the relative alignment of the sites, to which deviations δ_1 and δ_2 can be added. The separation between the sites is a. (b) The effect of the bipolaron formation energy U on the energy alignment of site β, with an energy that is σ_β lower if unoccupied.

some first results.

In the adapted two-site model, we still use two sites α and β, each linked to the environment, but now specify the energy levels explicitly and calculate transitions accordingly, see Fig. 8.1(a). The relative energy between the sites is determined by the electric field F and a local deviation in energy δ_1 or δ_2. The transport rates are now dependent on the relative energy difference of the sites and the temperature (Eq. 7.1). In this case, also thermally activated backward hops are considered. The deviations δ_1 and δ_2 can be used to simulate disorder and the change in energy associated with forming a bipolaron. This bipolaron formation can be implemented in the following way. Consider the unoccupied site β to have an energy σ_β below the other sites due to disorder, as illustrated in Fig. 8.1(b). When a second charge is added to form a bipolaron, the bipolaron formation energy U has to be taken into account, shifting the site up in energy. As we consider site β to always be at least singly occupied, this means that its energy deviation is:

$$\delta_2 = U - \sigma_\beta. \tag{8.1}$$

Analogously to the approach in Ch. 3, rate equations can be written down for the many electron states A_{nm}, which are subsequently solved to get the current.[78] Even in this rather different model, with only the inclusion of backward hopping and not including branching, the current can still be expressed in the same generic form as in the original two-site model (Eq. 3.3):

$$I = I_\infty + I_B \left\langle 1 - \frac{1}{1 + \Gamma P_\mathrm{P} P_\mathrm{AP}} \right\rangle = I_\infty + I_B g\left(\Gamma, \frac{B}{B_\mathrm{hf}}\right), \tag{8.2}$$

where Γ now depends on the new parameters (F, δ_1/kT, δ_2/kT and p, the density of carriers in the environment). As the same expression is found, the line shapes that can be calculated are identical to the original model [Figs. 3.3 and 3.4]. Therefore, we only have to investigate the dependence of Γ on the new parameters to investigate the shape of the curves and of the prefactors to investigate the magnitude of the effect [using

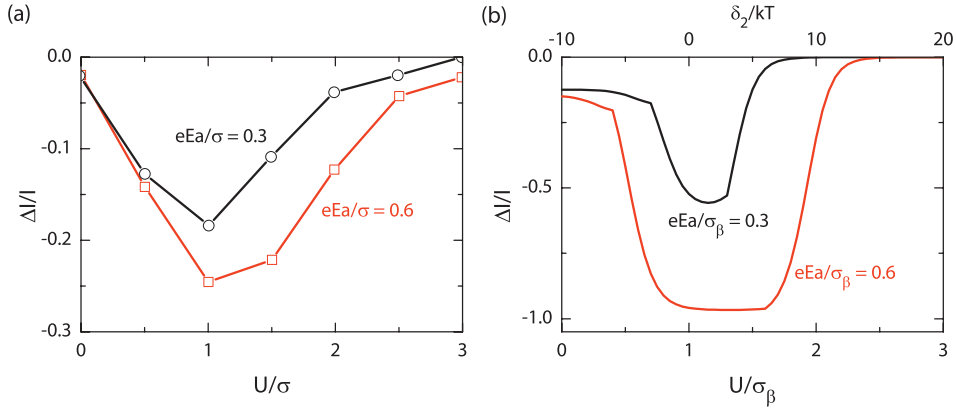

Figure 8.2: Magnetoconductance at a large magnetic field as a function of the bipolaron formation energy U for different electric fields F. (a) Results obtained with Monte Carlo simulations, where σ is the disorder strength and $\sigma/kT = 10$. Data adapted from Ref. 20. (b) Results calculated with the adapted two-site model, with σ_β as defined in Fig. 8.1(b). Resulting in $\delta_2 = U - \sigma_\beta = \sigma_\beta(U/\sigma_\beta - 1)$ (top axis), with $\sigma_\beta/kT = 10$, $\delta_1 = 0$, and $p = 0.5$.

Eq. (3.4)].

In the original model, a blocked situation with two parallel spins could only be lifted by the carrier on the first site hopping to the environment. The degree to which a carrier on the first site is forced to go through the second site was defined as the branching ratio b. For a large b it is hard to lift a blocked situation, resulting in a large MC and a large Γ, which gives a broad curve. In the simplest version of the extended model, no branching is included, but there are two other ways to lift a blocked situation. (i) The carrier on the first site can hop back into the environment. (ii) A carrier can hop from the environment back onto the second site to form a bipolaron. After dissociation by hopping to the environment of one of the two carriers in the bipolaron, a spin with random orientation is left on the site.

A first analysis of the influence of the different parameters has been made.[78] Here, we will focus on the comparison with several results from the Monte Carlo simulations by Bobbert *et al.*[20] In Fig. 8.2(a), the MC, as was found in the Monte Carlo simulations, is plotted as a function of the bipolaron formation energy U. The magnitude of the MC is largest around $U/\sigma \approx 1$, with σ the disorder strength, and it increases for a larger electric field. In the adapted model, we calculate the MC as a function of U/σ, using Eq. (8.1) that followed from Fig. 8.2(b). For all parameters we use the same values as in the Monte Carlo simulations. Note, however, that only a single energy of β is evaluated instead of averaging over an ensemble of configurations. Doing so, we obtain results as plotted in Fig. 8.2(b). Like in the Monte Carlo simulations, the magnitude of the MC is largest around $U/\sigma \approx 1$ and a similar trend with electric field is found. Moreover, the MC has a finite value at $U/\sigma = 0$, while it goes to zero for $U/\sigma \to \infty$. Considering the simplifications made, these results can already be considered a good agreement.

In the Monte Carlo simulations, an increase of the magnitude of the MC with decreasing temperature (increasing $1/kT$) is found, Fig. 8.3(a).[20] For increasing electric field, a larger saturation value is obtained. Simulations with similar parameters have

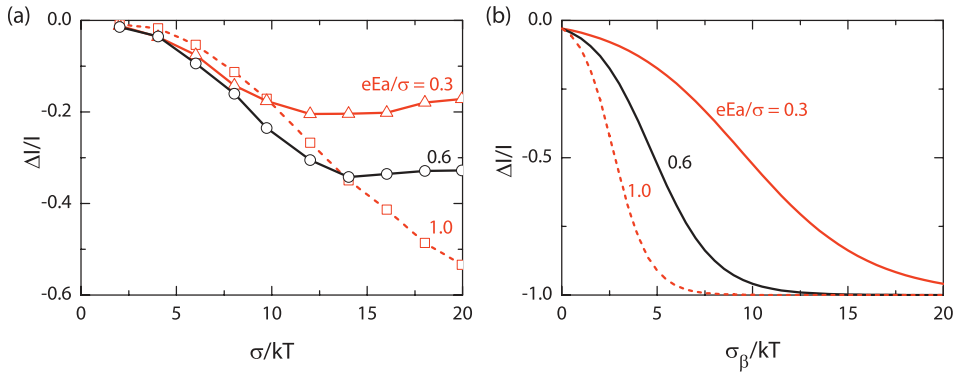

Figure 8.3: Magnetoconductance at a large magnetic field as a function of the inverse temperature for different electric fields. (a) Results obtained with Monte Carlo simulations, with U/σ = 1–1.5. Data adapted from Ref. 20. (b) Results calculated with the adapted two-site model, with σ_β as defined in Fig. 8.1(b), with $U/\sigma_\beta/kT$ = 1–1.5, $\delta_1 = 0$, and $p = 0.5$.

been performed with the adapted model, see Fig. 8.3(b). The increase in magnitude with decreasing temperature is confirmed, but the saturation behavior is different. In the Monte Carlo simulations, hopping to a neighboring site (branching) is always considered, resulting in a leakage current that determines the maximum magnitude of the MC. In the adapted model, at small temperatures (large $1/kT$), the system can become completely blocked if the thermal energy is too small to allow back hopping. So far, branching has not been included in the model, but it could be done by including the possibility for a magnetic-field-independent hop to a site at the same energy or a different energy.

In conclusion, the inclusion of physical parameters in the two-site bipolaron model shows a good agreement with the results obtained on a large grid of sites via Monte Carlo simulations. By averaging over a distribution of site energies and by including branching, the agreement could be further improved. This adapted model allows us to quickly investigate the influence of parameters like the electric field on the line shape and magnitude of the MC, which is time consuming with the Monte Carlo simulations. Moreover, Coulomb repulsion could be included like done in Ch. 3 in order to investigate sign changes of the MC. Being able to work with physical parameters may contribute to a better understanding of the Monte Carlo simulations, but also allows the direct comparison with experimental results.

8.2 An alternative approach to OMAR line shapes

One of the main characteristics of OMAR is the observation of MC(B) curves with a typical shape. It has been shown that these can be fitted well with either a Lorentzian function [$\propto B^2/(B_0^2 + B^2)$, Eq. 1.6] or an empirical non-Lorentzian function [$\propto B^2/(B_0 + |B|)^2$, Eq. 1.7]. Both functions have a similar width, characterized by the parameter B_0 that is typically 3–6 mT.[79] This width is believed to be related to the magnitude of the local, random hyperfine fields,[125] as was recently confirmed by experiments on deuterated polymers,[92] which were described in Sect. 1.3.4. However, from the models for OMAR, like the two-site bipolaron model in Ch. 3, we know that even with the same

hyperfine fields additional broadening occurs through the interactions in the model. This additional, hyperfine-field independent broadening also affects the value of B_0 obtained with either fitting function. Moreover, the models show that a smooth transition is present from a narrow Lorentzian to a broader non-Lorentzian, see for instance Ref. 20. Curves falling in such a transition regime cannot be fitted correctly by either of the two functions.

Therefore, we suggest to use an alternative empirical function for fitting the experimental curves, which separately includes the magnitude of the hyperfine fields and the effect of the model. This broadening, caused by the microscopic details of the model, is not unique to the bipolaron model. It will also occur in the e–h pair model, because this can be treated in an equivalent way.[23] Moreover, it is also present in the models we investigated with the Liouville equation (introduced in Ch. 7), like the exciton–charge quenching model.[116] In the models, the Lorentzian is the more fundamental line shape, as was, for instance, shown by Sheng *et al.*[125] A sum of two Lorentzians with different widths has thus also been used for fitting because two effects were expected to be present.[123] In Ch. 3 we showed that increasing the branching ratio in the two-site bipolaron model (which results in an increase of the parameter Γ that uniquely determines the shape of the curve) results in a broadening of the Lorentzian-like curves. The resulting curves could be fitted reasonably well with a non-Lorentzian, but a much better fit was obtained if an average over a range of Γ values was taken. The improvement when using a distribution indicates that the experimentally observed curves are both broadened by the microscopic mechanism and by the disorder in the material. The disorder results in variations in the transition rates between the sites and the branching parameter, which all influence Γ.

A clear difference between the Lorentzian and the non-Lorentzian curves is the way they converge to their high field value MC_∞. This can be seen by calculating $1 - \mathrm{MC}(B)/\mathrm{MC}_\infty$, which converges as $1/B^2$ for the Lorentzian and as $1/B$ for the non-Lorentzian. The exact power with which B converges is difficult to check experimentally as MC_∞ is usually not well defined due to the limited measuring range and high-field effects possibly playing a role as well. Nevertheless, the majority of the reported experimental curves can be much better fitted with the non-Lorentzian function.

The function we suggest gives very convincing results when fitting multiple data sets, as we will show. Although our equation could be partially motivated by specific models such as the model suggested by Prigodin *et al.*,[106] here we prefer a more generic, model-independent approach. Specifically, in the different models, a $1/B$-like convergence is only obtained after averaging over multiple curves. This averaging does not allow for an analytical treatment of the resulting curves. Therefore, we use an empirical function based on observations from the models and experiments.

In the models, the amount of mixing is determined by the external magnetic field in comparison to the hyperfine field. Furthermore, the details of the model determine how strongly this mixing is reflected in the resulting MC curves, possibly giving rise to additional hyperfine-field independent broadening. We characterize the hyperfine-field induced suppression of mixing by the parameter $\beta \in [1, \infty]$ that is a function of the magnetic field $\beta(B)$. We require the line-shape function $f(B)$, defined as $f(B) = 1 - \mathrm{MC}[\beta(B)]/\mathrm{MC}_\infty$, to fulfil four conditions. (i) For $\beta = 1$: $f = 1$. (ii) For $\beta \to \infty$: $f = 0$.

(iii) For $B \to \infty$, $\beta(B) \propto B^s$, with $s = 1$ as follows from a non-Lorentzian. (iv) For $B = 0$, $\mathrm{d}\beta/\mathrm{d}B = 0$, because there the magnitude of the magnetic field is negligible compared to the hyperfine field.

For $\mathrm{MC}(\beta)$, we use the following function, which fulfils requirement (i) and (ii) and introduces a parameter c_m that defines the width of the curve resulting from hyperfine-field independent broadening:

$$\mathrm{MC}(\beta) = \mathrm{MC}_\infty \left(1 - \frac{c_\mathrm{m} + 1}{c_\mathrm{m} + \beta}\right). \tag{8.3}$$

Now, we need to find a suitable function for $\beta(B)$ that takes the role of the hyperfine field into account and fulfils requirement (iii) and (iv). For this, we define an effective magnetic field B_eff, which is the average magnitude of the vector sum of the hyperfine field and the external field [Fig. 8.4(a)]. The effective field plotted in Fig. 8.4(a) is an average over a constant, but randomly oriented hyperfine field. We assume β to be equal to $B_\mathrm{eff}/B_\mathrm{hf}$. To be able to use β for fitting, we approximate it by using

$$\beta = B_\mathrm{eff}/B_\mathrm{hf} = \left(B_\mathrm{hf}^n + B^n\right)^{1/n}/B_\mathrm{hf}, \tag{8.4}$$

which gives the best fit for $n \approx 2.7$. This expression is inserted in Eq. (8.3), together with $c_\mathrm{m} = B_\mathrm{m}/B_\mathrm{hf}$, where B_m is the field scale of the broadening due to the model. We thus find:

$$\mathrm{MC}(B) = \mathrm{MC}_\infty \left[1 - \frac{B_\mathrm{m} + B_\mathrm{hf}}{B_\mathrm{m} + \left(B_\mathrm{hf}^n + B^n\right)^{1/n}}\right]. \tag{8.5}$$

Equation (8.5) can generate curves that are in good agreement with both Lorentzian and non-Lorentzian curves, reproducing both the fast and slow saturation. This is shown in Fig. 8.4(b) where a Lorentzian and non-Lorentzian curve are fitted with Eq. (8.5) (lines). For large $B_\mathrm{m}/B_\mathrm{hf}$ a non-Lorentzian-like curve is found. For these curves, MC_∞ – $\mathrm{MC}(B)$ converges as $1/B$ for $B \to \infty$, as is characteristic for the non-Lorentzian. For $B_\mathrm{m} \to 0$, a narrow curve that somewhat resembles a Lorentzian is found. We stress, however, that the convergence for $B \to \infty$ remains proportional to $1/B$, unlike a Lorentzian, which converges as $1/B^2$ Next, we will use Eq. (8.5) to fit several theoretical and experimental data sets.

The Monte Carlo simulations of the bipolaron model can produce both Lorentzian and non-Lorentzian curves, depending on the branching ratio b'.[20] On varying this ratio, a gradual transition between the two types of curves is observed, as is shown in Fig. 8.5(a). All the curves have been fitted with Eq. (8.5) to obtain B_hf and B_m as a function of b'. Resulting parameters of these fits are represented in Fig. 8.5(b). The resulting values for B_hf are nearly constant over the broad range of branching ratios, while B_m is found to change considerably. This is indeed what would be expected based on the input of the Monte Carlo simulations, where the hyperfine field is kept constant for all the simulations and only the branching ratio is changed. The new function, thus, not only allows us to fit the Lorentzian and non-Lorentzian curves, but also the intermediate cases.

Next, we compare with some experimental results reported in literature. For different materials, different line shapes have been observed. We fit the different curves

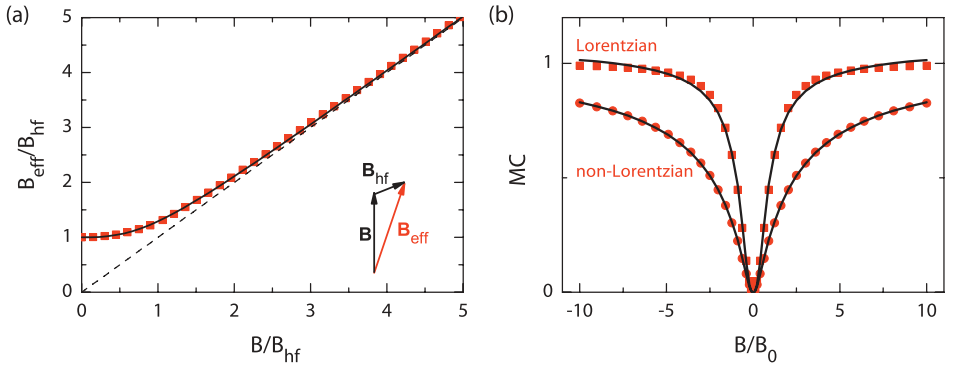

Figure 8.4: (a) Magnitude of the effective magnetic field which is the magnitude of the vector sum of the hyperfine field B_{hf} and the external field B, averaged over all directions of B_{hf}. The solid line is a fit to $B_{\mathrm{eff}} = (B_{\mathrm{hf}}^n + B^n)^{1/n}$, with $n \approx 2.7$. (b) Fits with Eq. (8.5) (lines) of a Lorentzian ($B_{\mathrm{m}} \approx 0$ and $B_{\mathrm{hf}} \approx 0.55\,B_0$) and non-Lorentzian curve ($B_{\mathrm{m}} \approx 2.0\,B_0$ and $B_{\mathrm{hf}} \approx 0.26\,B_0$).

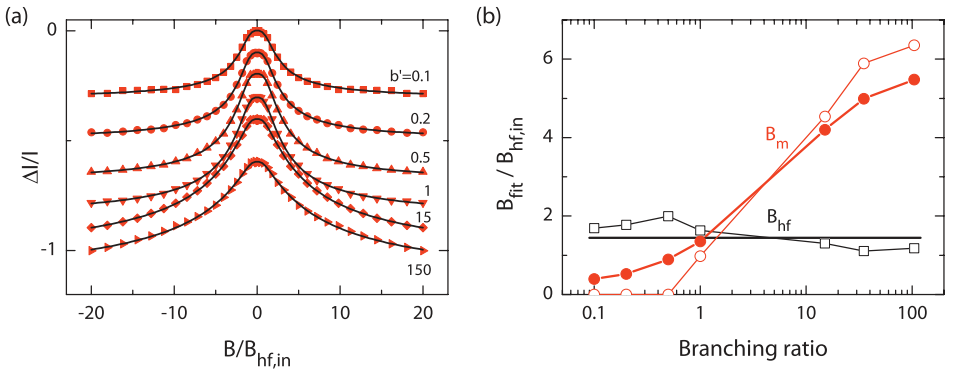

Figure 8.5: (a) OMAR curves calculated with Monte Carlo simulations of the bipolaron model[20] for various branching ratios b' (curves are vertically shifted for clarity). The curves are fitted with Eq. (8.5) (lines). Data obtained from F.W.A. van Oost. (b) Characteristic fields B_{hf} (black) and B_{m} (red) obtained by fitting as a function of branching ratio b'. Thin curves are for individual fits, while thick lines are for a global fit with shared B_{hf}, resulting in $B_{\mathrm{hf}} = 1.44\,B_{\mathrm{hf,in}}$, with $B_{\mathrm{hf,in}}$ the average value of the hyperfine fields used in the simulations.

reported by Mermer *et al.*[79] with Eq. (8.5), as shown in Fig. 8.6(a). In the introduction, we showed the same data, but fitted with a Lorentzian or a non-Lorentzian, see Fig. 1.9 on p. 19. In comparing the new fits with these, especially the fast saturating curves give a better fit than with a Lorentzian. In agreement with the fits of the Monte Carlo simulations, in the fits of these experimental curves the change in shape is completely determined by B_{m}, while B_{hf} has approximately the same value for all materials, $B_{\mathrm{hf}} \approx 2.8$ mT [Fig. 8.6(b)].

The variations in B_{m} can give additional information when comparing between materials or samples. For example, the value found for the polymer RRa-P3HT is slightly larger than the value for the very similar polymer RR-P3HT. The main difference between the polymers is that RRa-P3HT is more disordered, which would indeed give a

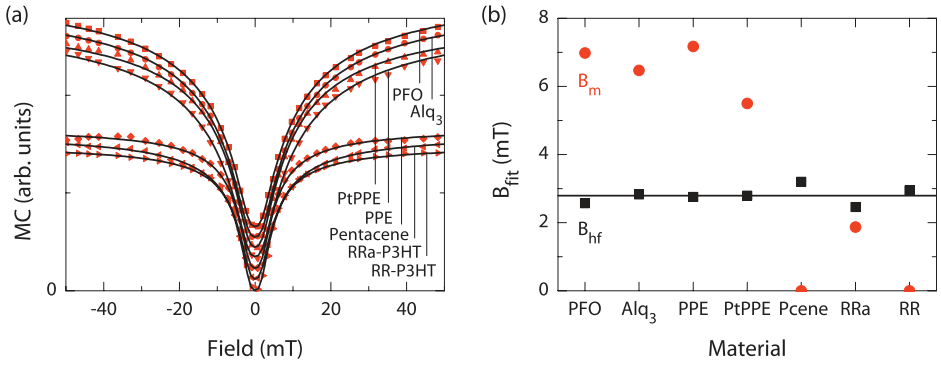

Figure 8.6: (a) OMAR curves measured for different materials, fitted with Eq. (8.5) (curves are vertically shifted for clarity). Data adapted from Ref. 79. (b) Characteristic fields B_{hf} (black) and B_{m} (red) obtained by fitting. The horizontal line indicates the mean $B_{\mathrm{hf}} \approx 2.8\,\mathrm{mT}$.

larger branching ratio in the bipolaron model. The small value of B_{m} for pentacene is in good agreement with this observation, because pentacene is also expected to be less disordered.

Bloom *et al.* have recently performed experiments with devices using Alq_3 with a small fraction of DCM (a dye molecule that acts as both an electron and a hole trap).[19] Here, we will not go into the details of the experiments, but the main observations were a decrease of MC on increased DCM concentration, in combination with a broadening of the MC(B) curves [Fig. 8.7(a)]. Moreover, on increasing the voltage, the width of the curves decreased. We fitted the extensive data set with Eq. (8.5) to obtain B_{hf} and B_{m} as a function of voltage for the different doping concentrations [Fig. 8.6(b)]. The resulting B_{hf} is approximately constant for all measurements and all voltages, with a mean of $B_{\mathrm{hf}} = 1.3\,\mathrm{mT}$. From these fits, it can be concluded that doping does not change the hyperfine fields, but changes the microscopic processes involved in OMAR. More generally, the fitting results show that all the changes in the shape and width of OMAR curves can probably be attributed to details of the microscopic model.

Other experimental results that would be very interesting to fit with the new function, are the anomalous curves observed when the MC changes sign.[16,79] These curves are the result of a different width of the negative and positive effect, whereby a superposition of the two effects leads to local extrema at finite values of the magnetic field. Based on the above observations, we would expect to be able to fit the curves with a sum of two of the new curves, each with different B_{m} and opposite sign, but with the same B_{hf}. Unfortunately, the reported curves are often noisy and with five free parameters the fits do not converge to a unique solution. A more general challenge when trying to fit the many curves available in literature is that these are very often plotted or measured on a large field scale, making it impossible to extract data for 0–5 mT, which is essential to properly fit B_{hf}.

The values found for B_{hf} are smaller than the values of B_0 obtained with the two other functions. These values of B_0 were considered a bit large compared to the hyperfine coupling constants known for these materials ($B_0 = 5.8\,\mathrm{mT}$ versus a hyperfine coupling of 1.8 mT for pentacene).[125] The values found for B_{hf} using the new func-

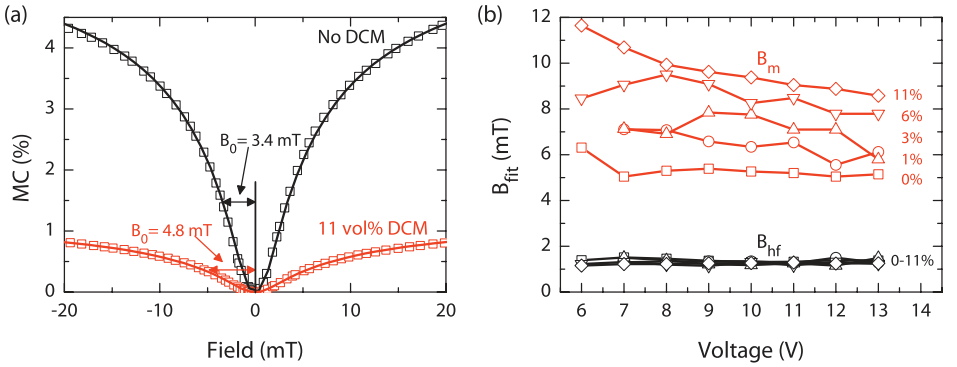

Figure 8.7: (a) OMAR curves measured at 10 V for Alq_3 devices with and without DCM doping, fitted with Eq. (8.5). Values of B_0 obtained with a non-Lorentzian fit are indicated. Data obtained from Ref. 19. (b) Characteristic fields B_{hf} (black) and B_m (red) obtained by fitting as a function of voltage for different amounts of DCM doping.

tion are more in the range of these hyperfine coupling constants (B_{hf} = 1.3–2.8 mT). It should be noted that the values found for B_{hf} for Alq_3 in Fig. 8.6(b) and 8.6(b) differ more than a factor of two. The origin of this difference is unclear as we would expect approximately the same value based on the universal value of B_{hf} for all the different materials in Fig. 8.6(b). We suggest to perform additional measurements, taking care of measuring sufficient data points around zero field, to allow for a better comparison. Also, the deuterated polymers that where recently used [92] are an interesting candidate for further investigation.

In conclusion, we have introduced a new empirical function that allows us to separately extract the role of the hyperfine field and the broadening induced by the microscopic mechanisms involved in OMAR. We have shown that the new function can be successfully used to fit several data sets, showing a constant contribution of the hyperfine field while the parameter describing the effect of the model accounts for al the observed changes in the shape of the curves. We suggest to investigate more materials under different conditions, making sure that measurements are also performed at small fields. Finally, a more formal analysis of the relationship between the mixing rate and the (effective) magnetic field could help in theoretically justifying the used function [Eq. (8.5)].

8.3 OMAR and spin injection

So far, we have discussed OMAR and spin polarized transport separately. We have seen that the relative orientation of the spins of two equal carriers plays an essential role in the bipolaron model for OMAR (Sect. 1.3.3 and Ch. 3), and that this orientation is modified by the random hyperfine fields, which also play an important role in spin transport (Ch. 6 and 7). In the bipolaron model, if the two spins are parallel, they are in a triplet configuration and no bipolaron can be formed, as this requires the pair to be in a singlet configuration. In a normal device, the spins are random and 25% singlets are formed. However, if the carriers would be injected with a fully spin-polarized electrode, only triplet pairs can be formed, assuming no spins are flipped. In this section,

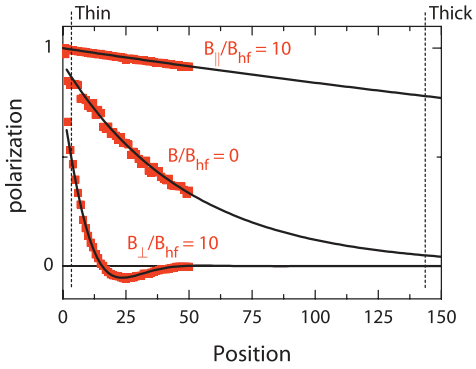

Figure 8.8: Spin polarization along the z-axis as a function of position in the device for parallel ($\theta = 0°$) and perpendicular ($\theta = 90°$) orientation of the magnetic field with respect to the polarization direction. The case without an external field is also shown. Lines are fits with Eq. (7.2).

we will briefly discuss this influence of a spin-polarized current on organic magnetoresistance and make suggestions and predictions for a possible experiment. The impact of this experiment works in two ways. On the one hand, it could be a direct proof of the bipolaron model, on the other hand it would be a clear sign of spin injection into the organic layer.

Assuming a fully spin-polarized electrode, initially all injected carriers have the same spin. However, once they are transported to the other electrode, this correlation is gradually lost, see Fig. 8.8, $B = 0$. In Ch. 6, we have seen that precession in the random hyperfine fields is the origin of this loss, but that, by applying a magnetic field parallel to the spin polarization, the spin-diffusion length can be significantly increased, Fig. 8.8. However, by applying the magnetic field perpendicular to the polarization direction, the spin-diffusion length is decreased due to the precession in this field as we have shown in Ch. 7 (Fig. 8.8). Thus, by changing the angle between the spin polarization and the applied magnetic field, we can tune the depth to which a significant spin polarization is preserved—and thus a correlation between the spins exists.

OMAR is considered to be a bulk effect, so in the case of the bipolaron model, spin blocking occurs throughout the device. If a correlation between the spins is present in part of the device, increased blocking occurs, resulting in an increase of the magnitude of OMAR. We suggest to measure OMAR in a device with a single ferromagnetic electrode for different orientations of the magnetic field with respect to the polarization. We expect a change in magnitude with angle if a spin-polarized current is injected and the bipolaron model is applicable. If OMAR is an e–h pair effect, using one spin polarized electrode will not change the spin statistics of the pairs. The change in magnitude with angle has to be compared to the intrinsic angle dependence that can be present (Ch. 5). Below, we will show that both a change in angle dependence and a change in line shape occur that are not present in the normal angle dependence.

We simulated MC(B) curves using the stochastic Liouville equation used in Ch. 5 [Eq. (5.1)], adapted for the bipolaron model.[116] Instead of assuming a source term with equal values for the singlet and the triplet pairs, these are now dependent on the spin

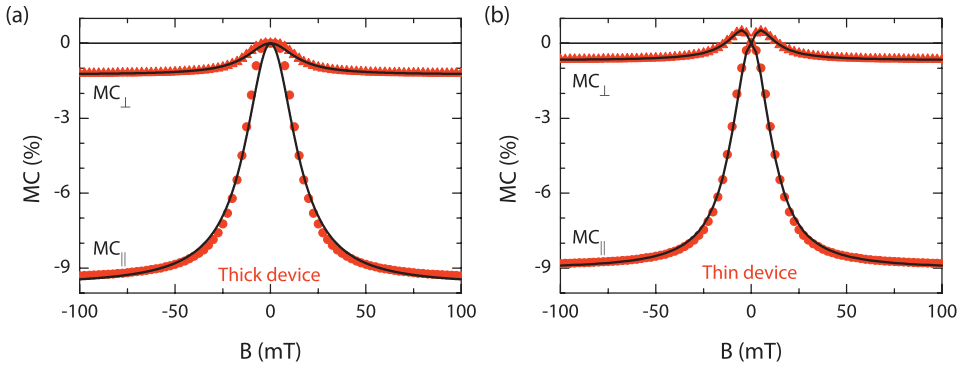

Figure 8.9: Simulated MC as a function of magnetic field, which is applied both parallel and perpendicular to the polarization direction. Assuming a fully spin-polarized electrode and either (a) a thick device and (b) a thin device.

correlation. This magnetic field and thickness dependent spin correlation follows from the analysis in Ch. 7, in particular Eq. (7.2). Note that spin blocking is only sensitive to the coherence of the spins. So, only the envelope of the precession of the spin polarization with the field applied under an angle is of relevance. We consider the two limiting cases of a thick and a thin device. The main difference is that at zero field, a polarization is present in the thin device, while it is negligible in the thick case. For both cases, we simulated OMAR curves for a parallel and perpendicular magnetic field as shown in Fig. 8.10.

For the thick device [Fig. 8.9(a)], the spin polarization at zero field is approximately zero. Increasing the field in the perpendicular direction can only make this smaller, so a regular line-shape is obtained. Increasing the field in the parallel direction increases the spin polarization, resulting in a larger magnitude of the MC. Moreover, the curve broadens as the increase in spin polarization mostly occurs at larger magnetic fields.

In the thin device [Fig. 8.9(b)], a significant polarization is already present at zero field. Applying a field in the parallel direction increases this polarization further, resulting in an increase in the magnitude of the effect, similar to the thick device. In this case it saturates faster than the thick device as the polarization is already larger at zero field, resulting in a smaller width. Due to the finite polarization present, increased spin-blocking already occurs at zero field. However, by applying a field in the perpendicular direction, the coherence is rapidly destroyed, resulting in less blocking compared to zero field, giving a small positive magnetoconductance. For larger fields, the normal spin blocking gives a negative MC. This behavior results in a different line shape that has a dip around zero field [Fig. 8.9(b)].

When the magnitude of the MC at large fields is also evaluated for intermediate angles, a characteristic angle dependence is obtained that follows a $\cos^4(\theta)$ dependence, see Fig. 8.10. As spin blocking by triplet pairs is responsible for the MC, the MC scales with the chance of triplet formation, so with the probability of finding two spins with the same spin direction. Intuitively, as the spin polarization of a single spin follows a $\cos^2(\theta)$ dependence, (Eq. 7.2), the triplet probability will indeed follow a $\cos^4(\theta)$ dependence. This is different from the $\cos^2(\theta)$ angle dependence that was found for the

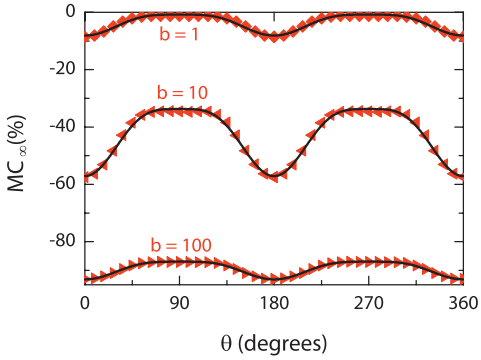

Figure 8.10: Magnitude of the MC at infinite magnetic field as a function of the angle of the field with the polarization direction. Curves for three branching ratios b are plotted and fitted with $\cos^4(\theta)$ (lines).

intrinsic angle dependence (Ch. 5).

In conclusion, when using a spin polarized current, the observed OMAR will change if the bipolaron model is applicable, resulting in a typical angle dependence. Compared to the normal angle dependence, an angle-dependent broadening is predicted in thick devices and a sign change is predicted for thin devices. Moreover, the magnitude at large fields is expected to show a $\cos^4(\theta)$ dependence. Experiments on organic devices of variable thickness with one ferromagnetic electrode could thus be used to simultaneously test the bipolaron model and to prove spin injection into the organic layer.

9 Outlook

In addition to the specific directions for further research that were presented in the previous chapter, in this chapter we more generally discuss the future of organic spintronics. We focus mostly on the two aspects of organic spintronics that are treated in this thesis: organic magnetoresistance and spin transport in disordered organic semiconductors.

In the field of OMAR, one of the main questions still is its origin. Several models have been proposed but still no clear consensus is reached on which model(s) is (are) applicable. Once the origin is understood, OMAR could prove a valuable tool for measuring properties of organic electronic devices. One could think of measuring the strength of hyperfine interaction (which is also very important for other organic spintronics applications), transport characteristics, or parameters involved in charge recombination or generation. Besides using OMAR as a tool, it also has a very promising technological application. It can be used as a cheap magnetic field sensor. In addition, it is (almost) omnidirectional, unlike many other field sensors, which makes it interesting for certain applications. In addition to using it for field sensing in ink-jet printed 'plastic' circuits,[72] one could also look at emerging applications like the use of OLEDs as chemical or biological sensors,[127] to which a new magnetic degree of freedom could be added. For all these applications it is an advantage that there is no need for perfect organic crystals, but that OMAR shows the largest effects in disordered materials. The effect works even better if the devices are partly degraded by conditioning.

One of the important steps towards a final conclusion on the origin of OMAR lies in the design of clever experiments. A good collaboration between physicists and chemists might prove invaluable as smart engineering of molecules could help to elucidate the effect. One successful example is the recent experiment with deuteration which proved the role of the hyperfine fields.[92] For new experiments, one could for instance think about designing materials with significant differences between the HOMO and LUMO, resulting in different hyperfine fields sensed by the electrons and holes. These could help distinguish between single-carrier or double-carrier effects. Doing so, it is important to

separate the broadening induced by microscopic effects from the hyperfine fields like suggested in Sect. 8.2.

In the experiments on organic spin valves, the focus has mostly been on readily available materials and straightforward processing techniques like evaporation and, incidentally, spin coating. The common choice for Alq_3 as the spacer layer is largely based on its wide availability as a prototype OLED material and it being used in the first successful spin valve.[149] There is, however, an interesting future for specially engineered materials and different type of devices. For instance by engineering materials with reduced hyperfine fields, by using lateral FET-like structures, or by using self assembled mono-layers. An interesting material is graphene, which only consists of carbon, so no hydrogen is present. Indeed, very long spin-diffusion lengths are found,[134] but it lacks the flexibility and tunability of conventional organic materials.

A challenge also lies in the fabrication of successful organic spin valves itself. For instance in a proper definition of the interface with the top electrode, preventing an 'ill-defined' layer and pinholes, and in finding proper materials for the bottom electrode that are stable against oxidation *and* are still magnetic at room temperature. This last requirement is only partially met by the commonly used LSMO, which has a strongly reduced magnetization at room temperature. The requirement could be fulfilled by using electrodes of a magnetic metal, like for instance Co, in combination with an oxidic tunnel barrier. This could open up possibilities for making lateral structures and for wet processing techniques.

Our simulations of spin transport in disordered organic semiconductors show that very large spin-diffusion lengths are expected at high electric fields (Ch. 6). In experiments, however, significant magnetoresistance is only reported at low voltages, see Sect. 1.3.1. Furthermore, a strong decrease in magnetoresistance is observed with voltage. The main question is if this discrepancy is caused by a dominance of tunneling through thin regions, or that spin transport is present, but the magnetoresistance is limited via a different mechanism. One such effect could be that there is efficient injection, but detection is reduced by the absence of a barrier at the detecting contact. This could explain the observation of the strongest MR in the diffusive regime at low bias. Perhaps different experiments can be devised that detect the polarization in an alternative way.

So far, to our knowledge no reports have been made on spin valve behavior and OMAR in the same device at the same time. However, both spin valve behavior and OMAR have been demonstrated using the same materials, for instance with Alq_3. Considering the mechanisms involved, this is somewhat unexpected. For spin polarized transport, we have shown in Ch. 6 that fast hopping is required. The time spent between hops has to be less than the typical precession time. On the other hand, for hyperfine mixing in the OMAR models, the time spend on a site should be larger than the typical precession time. This apparent contradiction might be explained in one of the following ways. (i) The effects observed in the spin valves are not originating from spin transport, but from tunneling through thin regions. (ii) Due to the broad distribution in waiting times of the carriers (Fig. 6.2), slow carriers might be contributing to the OMAR effect, while fast carriers are responsible for spin transport. (iii) Minority and majority carriers might play a different role. The fast majority carriers transport the spin, while the slow

minority carriers are responsible for OMAR. The space charge could play an important role in communicating this minority effect to the majority carriers, which carry most of the current. Simultaneous observation of OMAR and spin valve behavior in one device could be a proof that the majority of the current is not going through pinholes and spins are transported through the layer. The most convincing experimental proof would be the manipulation of spins during transport as simulated in Ch. 7.

One interesting application of organic electronics is the organic field effect transistor (OFET). With a gate electrode, the density of charges in the channel is controlled, resulting in typical mobilities of several $cm^2\,V^{-1}\,s^{-1}$. Using this approach, truly single-carrier devices are obtained, which could be useful for testing the mechanisms of OMAR. The high mobility might also prove beneficial for spin transport. However, for both applications, the high mobility and large carrier density could introduce completely new physics. Using several gate electrodes, it might even be possible to create and manipulate quantum dots in organic materials like shown in carbon nanotubes. [26]

In conclusion, organic spintronics is a new, but rapidly growing field. Various interesting effects have been demonstrated, but even more exciting possibilities lie ahead. Many open issues remain to be solved and new applications to be invented. It is not the question *if* we will ever see applications using organic spintronics; the question is *when* and *where* we will see them.

Summary / Samenvatting

Plastic Spintronics

Spin transport and intrinsic magnetoresistance in organic semiconductors

A specific class of plastics and other organic materials is (semi)conducting and can be used for electronic applications. In this thesis, we investigated their use in certain applications using magnetic fields. These applications belong to the field of spin electronics, or 'spintronics', where next to the charge of the electrons, also their spin is utilized. This spin can be considered as a small magnetic moment, pointing either up or down. Organic semiconductors have several advantages that make them interesting for applications in spintronics. They are relatively cheap, are easy to process, and can be chemically adapted. Two different, but related, topics that combine organic materials with spintronics have been studied both experimentally and theoretically.

The first topic is the recently discovered change in the current through an organic layer when a small magnetic field is applied. This effect is called organic magnetoresistance (OMAR). Large changes in the current (10–20%) have been found at relatively small magnetic fields (~10 mT) and at room temperature. These properties make the effect interesting for applications like, for instance, cheap magnetic field sensors, opening the possibility to add magnetic functionality to existing organic electronic applications. Moreover, if its mechanisms are understood, the effect could be used to investigate processes in conventional organic electronic devices by studying their magnetic response.

OMAR is observed in a wide range of organic materials, from small molecules to polymers. It is believed that OMAR originates from the interactions of a pair of charge carriers (for instance, electron–electron, hole–hole, or electron–hole). More specifically, it is believed that the possible interactions depend on the relative orientation of the spins of these two charges. Without an external magnetic field, small intrinsic magnetic fields in the organic layer (resulting from hyperfine coupling to nuclear spins) randomize the orientations of the two spins. This allows a change from a spin configuration that is less favorable for the current into a more favorable configuration. However, applying a magnetic field larger than these hyperfine fields results in a strong reduction of this spin randomization or spin mixing, causing a pair to remain locked in a less favorable

spin configuration.

Although there is agreement on the crucial role of hyperfine fields, the exact mechanisms behind OMAR are still heavily debated. Several models were proposed in literature that explain OMAR in terms of different charge pairs. In this thesis, we investigated a model based on pairs of equal carriers, called the bipolaron model. We used an elementary model of two neighboring sites, where, depending on the spins, one carrier might be preventing another one to pass. With this theoretical model we were able to successfully reproduce several characteristics of OMAR. Both a decrease and an increase in current, as found in experiments, could be obtained and also the universal shapes of the experimental OMAR curves could be reproduced.

Additionally, we performed new types of experiments to gain better understanding of OMAR. We showed that when an oscillating magnetic field is applied, OMAR is reduced beyond a certain frequency threshold. This occurs when the slowest charges can no longer follow the oscillations, as we showed by measuring the frequency dependence of the capacitance. These findings are in agreement with recent interpretations in which these slowest carriers are expected to induce the largest OMAR effect.

In literature, it was claimed that OMAR is independent of the orientation of the magnetic field. However, via sensitive measurements we demonstrated a small but systematic dependence on the angle between the magnetic field and the sample. We showed theoretically that this angle dependence can be explained in the different models by including an interaction between the spins. This interaction has to be direction dependent in order to explain the angle dependence. We identified dipole–dipole coupling or an anisotropy in the hyperfine fields as the most likely candidates.

Furthermore, we outlined a first exploration of an alternative approach to describe OMAR curves. We introduced a function that allows us to extract information both about the hyperfine fields and about an additional broadening of the curves. Thereby, this approach could allow for a more quantitative analysis of changes in the OMAR curves resulting from changes in the operating conditions or the material properties.

In the second topic, the spin of electrons is used in a different way. In many spintronics applications a difference between the number of spin-up and spin-down electrons, called spin polarization, is used to transport information through a device. For the functioning, it is essential that this polarization persists while transporting the charges. The main mechanism for loss of polarization in most *inorganic* semiconductors, which is related to spin–orbit coupling, is negligible in organic materials. The absence of this loss mechanism makes organic materials ideal candidates for these types of spintronics applications. However, there might still be other mechanisms that cause a smaller but non-zero loss of spin polarization. We conjecture that the hyperfine fields are the main source of polarization loss in organic materials, which results from mixing between the spin-up and spin-down electrons by precession of spins about these random fields.

We theoretically investigated this effect of the hyperfine fields on the spin polarization. We explicitly included the hopping transport characteristic for organic semiconductors. Due to spatial and energetic disorder, the charges hop from one localized site to another. The longer the time they spend on a site, the larger the loss of spin polarization. We showed that an external magnetic field larger than the typical hyperfine-field strength reduces the loss of spin polarization. Hence, such an external field causes the

polarization to persist over a larger distance, leading to an increase of the spin-diffusion length. We thus found a magnetic-field dependent spin-diffusion length. In addition, we found the spin-diffusion length to depend only weakly on temperature.

A spintronics device that makes use of spin-polarized transport is the spin valve. Using the magnetic-field dependent spin-diffusion length obtained from our theory, we could very accurately fit experimental data on the magnetoresistance of organic spin valves reported in literature. However, there is still a hot debate on the interpretation of these and similar experiments. The question has been raised whether spins are indeed transported through the whole layer, or only through thin regions. A discriminating experiment would be the manipulation of spins during their transport through the organic layer. This can be done by applying a magnetic field perpendicular to the direction of the spin polarization. Using our spin-transport model, we made predictions about the results that can be expected from such an experiment. We showed that, in the case of transport through the organic layer, an effect of a perpendicular field should be observable, but that the strong oscillations in the signal that are typically seen in inorganic semiconductors will be absent.

Finally, as an extension of the work presented in this thesis, we made predictions about possible future experiments in which spin polarization is combined with OMAR. Because for a spin-polarized current the majority of the spins point in the same direction, most charge pairs will have parallel spins. Therefore, within the bipolaron model, we expect an increase in the magnitude of OMAR when the injected current is spin polarized. Moreover, we showed that the shapes of the OMAR curves will also be changed. These experiments would provide a means to both prove spin-polarized transport and to validate the bipolaron model.

In conclusion, both theoretical and experimental results on OMAR and spin polarized transport have been presented in this thesis. Contributions have been made to a new model for OMAR and new type of experiments have been performed that have added further insights to the puzzle of OMAR. The limiting role of the hyperfine fields on spin-polarized transport has been investigated theoretically, providing an explanation for the experimentally observed magnetoresistance curves of organic spin valves and providing suggestions for future experiments. Although the present work has led to better understanding of OMAR and spin-polarized transport, the field of organic spintronics still poses many theoretical and experimental challenges that should be resolved before a widespread emergence of organic-spintronics applications will occur.

Plastic Spintronica

Spintransport en intrinsieke magnetoweerstand in organische halfgeleiders

Een specifieke klasse van plastics en andere organische materialen is (half)geleidend en kan gebruikt worden voor elektronische toepassingen. In dit proefschrift hebben we hun gebruik in bepaalde magnetische toepassingen onderzocht. Deze toepassingen behoren tot het veld van spinelektronica, of 'spintronica', waarbij naast de lading van de elektronen ook gebruik wordt gemaakt van hun spin. Deze spin kan beschouwd worden als een klein magnetisch moment dat naar boven of naar beneden wijst. Organische halfgeleiders hebben een aantal voordelen die hen interessant maken voor toepassing in spintronica: ze zijn relatief goedkoop, ze zijn gemakkelijk te verwerken en ze kunnen chemisch aangepast worden. In dit proefschrift zijn twee verschillende, maar gerelateerde, onderwerpen die organische materialen combineren met spintronica, zowel experimenteel als theoretisch onderzocht.

Het eerste onderwerp is de recent ontdekte verandering in de stroom door een organische laag ten gevolge van een klein magneetveld. Dit effect wordt organische magnetoweerstand (OMAR) genoemd. Grote veranderingen in de stroom (10–20%) zijn gevonden bij relatief kleine magnetische velden (~10 mT) bij kamertemperatuur. Deze eigenschappen maken OMAR interessant voor toepassingen zoals goedkope magnetischveldsensoren, waardoor bijvoorbeeld magnetische functionaliteiten toegevoegd kunnen worden aan bestaande organische elektronische toepassingen. Daarnaast kan een beter begrip van de OMAR-mechanismes ook gebruikt worden om andere processen in conventionele organische elektronica te onderzoeken door naar hun magnetische respons te kijken.

OMAR komt voor in een breed scala van organische materialen, van kleine moleculen tot (grote) polymeren. Het wordt geloofd dat OMAR ontstaat uit de interactie van twee ladingsdragers (bijvoorbeeld: elektron–elektron, gat–gat of elektron–gat). Meer specifiek wordt geloofd dat de mogelijke interacties afhangen van de relatieve oriëntatie van de spins van deze twee ladingen. Zonder een extern magneetveld worden de oriëntaties van de spins gerandomiseerd door kleine intrinsieke magneetvelden (ten gevolge van de hyperfijnkoppeling aan de kernspins) in de organische laag. Hierdoor kan een spinconfiguratie veranderen van een configuratie die minder gunstig is voor de stroom naar een gunstigere configuratie. Echter, door een magneetveld aan te leggen dat groter is dan deze hyperfijnvelden wordt de randomisatie sterk verminderd. Dit zorgt ervoor dat twee ladingsdragers vast kunnen blijven zitten in een minder gunstige spinconfiguratie.

Hoewel er overeenstemming is over de cruciale rol van hyperfijnvelden, worden de exacte mechanismes achter OMAR nog sterk bediscussieerd. In de literatuur zijn verscheidene modellen voorgesteld die OMAR uitleggen op basis van verschillende soorten ladingsparen. In dit proefschrift hebben we een model onderzocht dat gebaseerd is op paren van gelijke ladingen, het zogenaamde bipolaron model. We hebben een elementair model ontwikkeld van twee naburige posities, waar, afhankelijk van de spin, de ene ladingsdrager kan voorkomen dat de andere ladingsdrager kan passeren. Met dit theoretische model hebben we succesvol verschillende karakteristieken van OMAR kunnen reproduceren, zoals zowel de toename als afname van de stroom die gezien wordt in experimenten, en de universele vorm van de experimentele OMAR-curves.

Daarnaast hebben we verschillende nieuwe type experimenten uitgevoerd om een beter begrip te krijgen van OMAR. We hebben laten zien dat wanneer een oscillerend magneetveld gebruikt wordt het OMAR effect kleiner wordt voorbij een bepaalde frequentie. Dit gebeurt wanneer de langzaamste ladingen de oscillaties niet meer kunnen volgen, wat we hebben aangetoond door de frequentieafhankelijkheid van de capaciteit te meten.

In literatuur wordt geclaimd dat OMAR onafhankelijk is van de oriëntatie van het magnetische veld. Echter, via gevoelige metingen hebben wij een kleine maar systematische afhankelijkheid van OMAR gedemonstreerd van de hoek tussen het magneetveld en het sample. We hebben theoretisch laten zien dat deze hoekafhankelijkheid uitgelegd kan worden door in de verschillende modellen een interactie tussen de spins mee te nemen. Deze interactie moet richtingsafhankelijk zijn om de hoekafhankelijkheid te verklaren. Als de meest waarschijnlijke oorzaken voor de interactie hebben we dipool–dipool koppeling of een anisotropie in de hyperfijnvelden geïdentificeerd.

Tenslotte hebben we een eerste onderzoek geschetst van een alternatieve benadering om OMAR curves te beschrijven. We hebben een functie geïntroduceerd die het mogelijk maakt om informatie te krijgen over zowel de hyperfijnvelden als over een extra verbreding van de curves. Zodoende zou deze benadering het mogelijk kunnen maken om een meer kwantitatieve analyse te maken van veranderingen in de OMAR curves ten gevolge van veranderingen in de experimentele instellingen of de materiaaleigenschappen.

In het tweede onderwerp wordt de spin van elektronen op een andere manier gebruikt. In veel spintronica toepassingen wordt een verschil tussen de spin-op en spin-neer elektronen, een zogenaamde spinpolarisatie, gebruikt om informatie te transporteren. Voor het functioneren is het essentieel dat deze polarisatie behouden blijft terwijl de ladingen getransporteerd worden. Het voornaamste mechanisme voor verlies van polarisatie in de meeste *inorganische* halfgeleiders is verwaarloosbaar in organische materialen. De afwezigheid van dit verliesmechanisme maakt organische materialen ideale kandidaten voor dit type spintronicatoepassingen. Er kan echter nog een ander mechanisme zijn dat een kleiner, maar niet verwaarloosbaar, verlies van polarisatie veroorzaakt. Wij suggereren dat de hyperfijnvelden de voornaamste oorzaak zijn van verlies van spinpolarisatie in organische materialen, omdat de spin-op en spin-neer elektronen kunnen mixen door precessie rond deze random hyperfijnvelden.

Wij hebben het effect van de hyperfijnvelden op de spinpolarisatie theoretisch onderzocht. Hierbij hebben we expliciet het hoppingtransport meegenomen dat karakteristiek is voor organische halfgeleiders. Door ruimtelijke en energetische wanorde hoppen de ladingen namelijk van de ene naar de andere gelokaliseerde positie. Hoe langer ze op een positie zitten, hoe groter het verlies van spinpolarisatie. We hebben laten zien dat een extern magneetveld dat groter is dan de typische hyperfijn veldsterkte het verlies van spinpolarisatie reduceert. Een dergelijk extern veld zorgt er dus voor dat de spinpolarisatie behouden blijft over een grotere afstand, resulterend in een toename van de spindiffusielengte. We hebben dus een magneetveldafhankelijke spindiffusielengte gevonden. Deze hangt bovendien slechts zwak af van de temperatuur.

Een spintronica device dat gebruikmaakt van spingepolariseerd transport is de organische *spin valve*. Met de magneetveldafhankelijke spindiffusielengte uit onze theorie

konden we zeer nauwkeurig de experimentele data uit de literatuur van magnetoweerstand van organische *spin valves* fitten. Er vindt echter nog een verhit debat plaats over de interpretatie van deze en vergelijkbare experimenten. De essentiële vraag is of spins inderdaad getransporteerd worden door de hele laag, of alleen door dunne gebieden. Een onderscheidend experiment zou de manipulatie van spins zijn tijdens hun transport door de organische laag. Dit kan gedaan worden door een magneetveld loodrecht op de richting van de spinpolarisatie aan te leggen. Met ons spintransportmodel hebben we voorspellingen gedaan van resultaten die verwacht kunnen worden van een dergelijk experiment. We hebben laten zien dat, in het geval van transport door de organische laag, een effect van een loodrecht veld waarneembaar zou moeten zijn, maar dat de sterke oscillaties in het signaal die typisch zijn voor inorganische halfgeleiders afwezig zijn.

Tenslotte, als uitbreiding van het werk gepresenteerd in dit proefschrift, hebben we voorspellingen gedaan over mogelijke toekomstige experimenten waarin spinpolarisatie gecombineerd wordt met OMAR. Omdat de meerderheid van de spins dezelfde kant op wijzen in een spingepolariseerde stroom, zullen de meeste paren parallelle spins hebben. In het bipolaron model verwachten we daarom een toename in OMAR als de geïnjecteerde stroom spingepolariseerd is. Bovendien hebben we laten zien dat de vorm van de OMAR curves dan ook zal veranderen. Deze experimenten zouden een mogelijkheid kunnen bieden om zowel spingepolariseerd transport als het bipolaron model te valideren.

In dit proefschrift zijn zowel theoretische als experimentele resultaten van OMAR en spingepolariseerd transport gepresenteerd. Er is bijgedragen aan een nieuw model voor OMAR en er zijn nieuwe type experimenten uitgevoerd die meer inzichten toegevoegd hebben aan de puzzel van OMAR. De limiterende rol van de hyperfijnvelden voor spingepolariseerd transport is theoretisch onderzocht en biedt zowel een verklaring voor de experimenteel geobserveerde magnetoweerstandscurves van organische *spin valves*, als suggesties voor toekomstige experimenten. Hoewel er nog vele theoretische en experimentele uitdagingen opgelost moeten worden, heeft het huidige werk geleid tot beter begrip van OMAR en spingepolariseerd transport. Daarmee draagt het bij aan een toekomst waarin organische spintronica wijdverspreid op zal kunnen komen.

Curriculum vitae

Wiebe Wagemans was born on August 4, 1980, in Arnhem, the Netherlands. There, he went to high school at the Thomas a Kempis College. After his graduation in 1998, he moved to Eindhoven to study Applied Physics at the Eindhoven University of Technology. For his studies he did a local internship in the plasma physics group of prof.dr.ir M.C.M. van der Sanden and an internship abroad in the group of dr. J.S. Moodera at the Massachusetts Institute of Technology on the topic of magnetic tunnel junctions. For his graduation project he investigated organic spin valves in the group of prof.dr. B. Koopmans. After successful completion of the project in 2006, Wiebe decided to stay in the same group as a PhD candidate. Part of his PhD work is described in this thesis, but he also made contributions to several of the related efforts in the group. Moreover, a new infrastructure was set up, including new measurement techniques. As part of his work, Wiebe supervised six Bachelor and three Master students. He was chosen as the best practicum supervisor in 2007.

During his studies, Wiebe was a member of the board of the study association for one year. From 1999 to 2003, he was one of the artists in the Circus of Physics, which performs at primary and secondary schools. In 2002, inspired by the success of the circus, Wiebe and Jelle de Jong founded *Stichting Techniekpromotie*, a foundation that promotes science and technology to children aged 4 to 15. As one of the new activities, Wiebe organized the first edition of the FIRST LEGO League in the Netherlands in 2003. This is a competition for teams of 5–10 children, using a LEGO-based robot, but also asking for many other skills. His work included finding teams, training volunteers, and organizing all logistics. The foundation has rapidly grown and now has many partners in the Netherlands. In 2009, more than 50.000 persons participated in one of the many activities. Wiebe is still involved in the foundation as a board member, but activities are now organized by a dedicated bureau.

After his graduation, Wiebe also became a board member of the alumni association of Applied Physics (2006–2009). First, he was responsible for the quarterly magazine and later became chairman. In his free time, Wiebe likes to take photographs and to practise yoga and meditation.

List of publications

Angle dependent spin–spin interactions in organic magnetoresistance
W. Wagemans, A.J. Schellekens, M. Kemper, and B. Koopmans
in preparation.

Frequency dependence of organic magnetoresistance
W. Wagemans, P. Janssen, E.H.M. van der Heijden, M. Kemerink, and B. Koopmans
in preparation.

The effect of magnetic field orientation on the spin-diffusion length in organic semiconductors
W. Wagemans, F.W.A. van Oost, S. Wouters, A.J. Schellekens, P.A. Bobbert, and B. Koopmans
in preparation.

Microscopic modeling of organic magnetoresistance
A.J. Schellekens, W. Wagemans, and B. Koopmans
in preparation.

Spin in organics, a new route to spintronics
B. Koopmans, W. Wagemans, F.L. Bloom, P.A. Bobbert, M. Kemerink, and M. Wohlgenannt
submitted to Philisophical Transactions of the Royal Society A (2010).

Separating photocurrent and injected current contributions to the organic magnetoresistance
W. Wagemans, W.J. Engelen, F.L. Bloom, and B. Koopmans
Synthetic Metals **160**, 266–270 (2010).

Spin relaxation and magnetoresistance in disordered organic semiconductors
P.A. Bobbert, T.D. Nguyen, W. Wagemans, F.W.A. van Oost, B. Koopmans, and M. Wohlgenannt
Synthetic Metals **160**, 223–229 (2010).

Theory for spin diffusion in disordered organic semiconductors
P.A. Bobbert, W. Wagemans, F.W.A. van Oost, B. Koopmans, and M. Wohlgenannt
Physical Review Letters **102**, 156604 (2009).

Magnetoresistance in hybrid organic spin valves at the onset of multiple-step tunneling
J.J.H.M. Schoonus, P.G.E. Lumens, W. Wagemans, J.T. Kohlhepp, P.A. Bobbert, H.J.M. Swagten, and B. Koopmans
Physical Review Letters **103**, 146601 (2009).

Sign inversion of magnetoresistance in space-charge limited organic devices
F.L. Bloom, M. Kemerink, W. Wagemans, and B. Koopmans
Physical Review Letters **103**, 066601 (2009).

Correspondence of the sign change in organic magnetoresistance with the onset of bipolar charge transport
F.L. Bloom, W. Wagemans, M. Kemerink, and B. Koopmans
Applied Physics Letters **93**, 263302 (2008).

A two-site bipolaron model for organic magnetoresistance
W. Wagemans, F.L. Bloom, P.A. Bobbert, M. Wohlgenannt, and B. Koopmans
Journal of Applied Physics **103**, 07F303 (2008).

Temperature dependent sign change of the organic magnetoresistance effect
F.L. Bloom, W. Wagemans, B. Koopmans
Journal of Applied Physics **103**, 07F320 (2008).

Extremely large magnetoresistance in boron-doped silicon
J.J.H.M. Schoonus, F.L. Bloom, W. Wagemans, H.J.M. Swagten, and B. Koopmans
Physical Review Letters **100**, 127202 (2008).

Separating positive and negative magnetoresistance in organic semiconductor devices
F.L. Bloom, W. Wagemans, M. Kemerink, and B. Koopmans
Physical Review Letters **99**, 257201 (2007).

Detailed study of the plasma-activated catalytic generation of ammonia in N_2–H_2 plasmas
J.H. van Helden, W. Wagemans, G. Yagci, R.A.B. Zijlmans, D.C. and Schram, R. Engeln, G. Lombardi, G.D. Stancu, and J. Röpcke
Journal of Applied Physics **101**, 043305 (2007).

Acknowledgements / Dankwoord

De eerste die ik wil bedanken dat ben jij, omdat je interesse toont in mijn proefschrift, al is het alleen maar in dit dankwoord. Daarnaast zijn er natuurlijk meer mensen die ik wil bedanken, een promotieonderzoek doe je namelijk niet alleen. Veel mensen hebben direct of indirect een bijdrage geleverd. Een aantal wil ik graag met name bedanken.

Mijn directe begeleider en promotor Bert Koopmans, ik wil je graag bedanken voor je vertrouwen, je enthousiasme en je beschikbaarheid. Je maakte altijd tijd voor (wetenschappelijke) discussie en kwam regelmatig enthousiast binnen lopen met nieuwe ideeën. Henk Swagten, wat meer van de zijlijn, maar ik heb onze gesprekken over verschillende onderwerpen zeker erg gewaardeerd. Peter Bobbert, bedankt dat je mijn copromotor wilde zijn, en bedankt voor het gedetailleerde inhoudelijke commentaar op mijn werk en de andere inhoudelijke discussies tijdens mijn onderzoek.

I also want to thank the other committee members, René Janssen, Wilfred van der Wiel, Marcus Wohlgenannt and William Gillin for carefully reading my thesis. Marcus, I also want to thank you for being a co-author on several papers. I have especially fond memories of our editing sessions in Brazil.

Aan bijna alle onderwerpen in deze thesis hebben één of meer afstudeerders en stagairs een bijdrage geleverd. Stagairs Joost Voorbraak, Arno van den Brink, Thomas Lemmens, Roel Heijnen, Rob Mensink en Ilse van der Heijden, en afstudeerders Marijn Kemper, Wouter Engelen en Sjors Schellekens, allemaal bedankt! Ik heb het erg leuk gevonden om jullie te begeleiden en om met jullie samen te werken.

Francisco Bloom, you were the other PhD student on the organic spintronics project. Thank you for the fruitful collaboration, which resulted in the creation of a new setup and many papers. I also enjoyed our trips to several international conferences. Paul Janssen, jij bent nu onze opvolger. Het was leuk om je in te werken en om met je naar Kopenhagen te gaan.

Zonder de technici Gerrie Baselmans, Jef Noijen en Jeroen Francken was het niet mogelijk geweest om zoveel nieuwe opstellingen te maken en experimenten uit te voeren. Daarnaast wil ik ook iedereen van de werkplaats hartelijk bedanken voor hun bijdrage. Met name de 'klusjesman', hij/zij heeft de afgelopen vier jaar talloze klusjes voor mij uitgevoerd.

Bijna alle samples die ik heb gebruikt, heb ik gemaakt bij scheikunde. Graag wil ik de groep daar bedanken voor het beschikbaar stellen van de faciliteiten en vooral ook Martijn Wienk voor de hulp.

Bij natuurkunde wil ik ook nog Martijn Kemerink en Frank van Oost bedanken voor de samenwerking, de discussies en de nodige inzichten.

Ook wil ik graag de leden bedanken van de groep Fysica van Nanostructuren (FNA), waar ik inclusief mijn afstuderen ruim vijf jaar met heel veel plezier heb rondgelopen. Bedankt voor de koffiepauzes, publicatie-borrels, sinterklaasvieringen, oudejaarsbraspartijen, groepsuitjes, tuinfeesten, en nog veel meer. Ik wil zeker ook de spelers en coaches van het zaalvoetbalteam Spin 'm d'r in, waar ik een paar jaar met veel plezier mee heb gespeeld, bedanken. Wim, Jürgen, Oleg, Beatriz, bedankt. Karin bedankt voor de goede support. Kamergenoten Coen, Francesco en Reinoud bedankt voor de gezelligheid, en ook de (oud-)promovendi en post-docs Harm, Karel, Csaba, Corine, Paresh, Omer, Jeroen, Andrei, Gregory, Muriel, Sabine, bedankt. De dynamiek in de groep kwam voor een groot deel ook door alle verschillende studenten, waarvan er te veel zijn geweest om allemaal te noemen, maar toch zeker ook jullie bedankt.

Jan Millenaar, ik wil je graag bedanken omdat je mij als eerstejaars student bij het Natuurkundecircus hebt gevraagd. Niet alleen heb ik veel van je geleerd, maar ook heeft het circus Jelle de Jong en mij geïnspireerd om de Stichting Techniekpromotie op te richten. Jelle, en ook de andere (oud-)bestuursleden van de stichting, bedankt voor de gezellige vergaderingen, maar speciaal ook voor het samenwerken aan zo'n mooi doel.

Ook het lidmaatschap van het bestuur van de Alumnivereniging VENI heb ik erg leuk gevonden. Sonja, Erik, Patrick, Jeroen, Daniel, Thijs, bedankt, vooral ook voor de gezellige vergaderingen en etentjes. Ook oud-Van-der-Waalsbestuur Equilibrium bedankt. Erik ook nog bedankt voor het klimmen en de andere gezellige activiteiten, ook al is dat de laatste tijd in het slop geraakt.

Mijn 'schoonfamilie' wil ik ook graag bedanken. Anja en Rob, bedankt voor het altijd klaar staan, de hulp, jullie liefde voor Kim en de gezellige vakanties.

Een aantal speciale vrienden wil ik ook bedanken. Jenny, Nico en Jasmijn, bedankt voor de fijne en gezellige avonden en de inspirerende discussies. Ook Erik, Marjolein en Michaëla bedankt voor jullie altijd warme en liefdevolle ontvangst. Sri Vasudeva en zijn organisatie Blue Star wil ik graag bedanken voor de steun bij mijn groei en voor de fijne omgeving met liefdevolle mensen. Al deze mensen hebben mij veel verdieping gebracht.

Mijn zus, Olga, dankzij jou ben ik begonnen met yoga en ook met meditatie. Hier heb ik veel aan gehad en heb ik nog steeds veel aan. Ik vind het fijn dat ik je heb kunnen helpen bij het opzetten van je eigen yogastudio. Mijn moeder, Dianne, bedankt voor je steun en liefde. Mijn vader, Gerard, en zijn partner, Gerda, bedankt voor jullie steun en interesse. Gerard, ik heb goede herinneringen aan onze vakantie in Egypte!

Eén iemand heeft wel heel veel voor mij betekend de afgelopen jaren. Kim, jij bent er altijd geweest om alles mee te kunnen delen. We zijn samen veel gegroeid de afgelopen jaren. In al die jaren ben je een onderdeel van mij geworden. Bedankt voor je steun en je liefde!

Bibliography

[1] Alexandrov, A.S. and Bratkovsky, A.M. *Carrier density collapse and colossal magnetoresistance in doped manganites*. Phys. Rev. Lett. **82**, 141 (1999). [p. 23]

[2] Arkhipov, V.I., Emelianova, E.V., Tak, Y.H., and Bässler, H. *Charge injection into light-emitting diodes: Theory and experiment*. J. Appl. Phys. **84**, 848 (1998). [p. 17]

[3] Aziz, H., Popovic, Z., Hu, N., Hor, A., and Xu, G. *Degradation mechanism of small molecule-based organic light-emitting devices*. Science **283**, 1900 (1999). [p. 37]

[4] Bagnich, S.A., Niedermeier, U., Melzer, C., Sarfert, W., and von Seggern, H. *Electron-hole pair mechanism for the magnetic field effect in organic light emitting diodes based on poly(paraphenylene vinylene)*. J. Appl. Phys. **106**, 113702 (2009). [p. 23, 24, and 30]

[5] Bagnich, S.A., Niedermeier, U., Melzer, C., Sarfert, W., and von Seggern, H. *Origin of magnetic field effect enhancement by electrical stress in organic light emitting diodes*. J. Appl. Phys. **105**, 123706 (2009). [p. 18, 19, 51, and 58]

[6] Baibich, M.N., Broto, J.M., Fert, A., Van Dau, F.N., Petroff, F., Etienne, P., Creuzet, G., Friederich, A., and Chazelas, J. *Giant magnetoresistance of (001)Fe/(001)Cr magnetic superlattices*. Phys. Rev. Lett. **61**, 2472 (1988). [p. 12 and 67]

[7] Baldo, M. and Forrest, S. *Transient analysis of organic electrophosphorescence: I. transient analysis of triplet energy transfer*. Phys. Rev. B **62**, 10958 (2000). [p. 31 and 51]

[8] Barth, S., Bässler, H., Rost, H., and Hörhold, H.H. *Extrinsic and intrinsic dc photoconductivity in a conjugated polymer*. Phys. Rev. B **56**, 3844 (1997). [p. 12]

[9] Bässler, H. *Charge transport in disordered organic photoconductors a Monte Carlo simulation study*. Phys. Status Solidi B **175**, 15 (1993). [p. 8, 68, and 80]

[10] Bergenti, I., Dediu, V., Arisi, E., Mertelj, T., Murgia, M., Riminucci, A., Ruani, G., Solzi, M., and Taliani, C. *Spin polarised electrodes for organic light emitting diodes*. Org. Electron. **5**, 309 (2004). [p. 14]

[11] Bergeson, J.D., Prigodin, V.N., Lincoln, D.M., and Epstein, A.J. *Inversion of magnetoresistance in organic semiconductors*. Phys. Rev. Lett. **100**, 067201 (2008). [p. 18, 19, 23, 24, 33, 34, and 57]

[12] Berthelot, A., Favero, I., Cassabois, G., Voisin, C., Delalande, C., Roussignol, P., Ferreira, R., and Gerard, J.M. *Unconventional motional narrowing in the optical spectrum of a semiconductor quantum dot*. Nat. Phys. **2**, 759 (2006). [p. 69 and 83]

[13] Binasch, G., Grünberg, P., Saurenbach, F., and Zinn, W. *Enhanced magnetoresistance in layered magnetic structures with antiferromagnetic interlayer exchange*. Phys. Rev. B **39**, 4828 (1989). [p. 12 and 67]

[14] Blom, P., deJong, M., and Vleggaar, J. *Electron and hole transport in poly(p-phenylene vinylene) devices*. Appl. Phys. Lett. **68**, 3308 (1996). [p. 11 and 38]

[15] Bloom, F.L., Kemerink, M., Wagemans, W., and Koopmans, B. *Sign inversion of magnetoresistance in space-charge limited organic devices*. Phys. Rev. Lett. **103**, 066601 (2009). [p. 28, 29, 51, and 56]

[16] Bloom, F.L., Wagemans, W., Kemerink, M., and Koopmans, B. *Separating positive and negative magnetoresistance in organic semiconductor devices*. Phys. Rev. Lett. **99**, 257201 (2007). [p. 18, 29, 34, 38, 48, 56, and 96]

[17] Bloom, F.L., Wagemans, W., Kemerink, M., and Koopmans, B. *Correspondence of the sign change in organic magnetoresistance with the onset of bipolar charge transport*. Appl. Phys. Lett. **93**, 263302 (2008). [p. 18, 28, and 34]

[18] Bloom, F.L., Wagemans, W., and Koopmans, B. *Temperature dependent sign change of the organic magnetoresistance effect*. J. Appl. Phys. **103**, 07F320 (2008). [p. 18, 34, and 40]

[19] Bloom, F.L. *Exploring organic magnetoresistance—An investigation of microscopic and device properties*. Ph.D. thesis, Eindhoven University of Technology (2010). [p. 96 and 97]

[20] Bobbert, P.A., Nguyen, T.D., van Oost, F.W.A., Koopmans, B., and Wohlgenannt, M. *Bipolaron mechanism for organic magnetoresistance*. Phys. Rev. Lett. **99**, 216801 (2007). [p. 21, 22, 23, 33, 41, 43, 44, 47, 48, 56, 57, 68, 89, 91, 92, 93, 94, and 95]

[21] Bobbert, P.A., van Oost, F.W.A., and Cottaar, J. to be published. [p. 70]

[22] Bobbert, P.A., Wagemans, W., van Oost, F.W.A., Koopmans, B., and Wohlgenannt, M. *Theory for spin diffusion in disordered organic semiconductors*. Phys. Rev. Lett. **102**, 156604 (2009). [p. 69, 79, 80, 81, 83, 86, and 87]

[23] Bobbert, P., Nguyen, T., Wagemans, W., van Oost, F., Koopmans, B., and Wohlgenannt, M. *Spin relaxation and magnetoresistance in disordered organic semiconductors*. Synth. Met. **160**, 223 (2010). [p. 27, 41, and 93]

[24] Bobbert, P.A. *Organic semiconductors: What makes the spin relax?* Nat. Mater. **9**, 288 (2010). [p. 16]

[25] Chappert, C., Fert, A., and Van Dau, F.N. *The emergence of spin electronics in data storage*. Nat. Mater. **6**, 813 (2007). [p. 12]

[26] Churchill, H.O.H., Bestwick, A.J., Harlow, J.W., Kuemmeth, F., Marcos, D., Stwertka, C.H., Watson, S.K., and Marcus, C.M. *Electron-nuclear interaction in ^{13}C nanotube double quantum dots*. Nat. Phys. **5**, 321 (2009). [p. 23 and 103]

[27] Cinchetti, M., Heimer, K., Wuestenberg, J.P., Andreyev, O., Bauer, M., Lach, S., Ziegler, C., Gao, Y., and Aeschlimann, M. *Determination of spin injection and transport in a ferromagnet/organic semiconductor heterojunction by two-photon photoemission*. Nat. Mater. **8**, 115 (2009). [p. 16]

[28] Cölle, M. and Gärditz, C. *Phosphorescence of aluminum tris(quinoline-8-olate)*. Appl. Phys. Lett. **84**, 3160 (2004). [p. 25]

[29] Cölle, M., Gärditz, C., and Braun, M. *The triplet state in tris-(8-hydroxyquinoline)aluminum*. J. Appl. Phys. **96**, 6133 (2004). [p. 25]

[30] Crooker, S.A., Furis, M., Lou, X., Adelmann, C., Smith, D.L., Palmstrom, C.J., and Crowell, P.A. *Imaging spin transport in lateral ferromagnet/semiconductor structures*. Science **309**,

2191 (2005). [p. 16, 80, 86, and 87]

[31] D'Andrade, B.W. and Forrest, S. *White organic light-emitting devices for solid-state lighting*. Adv. Mater. **16**, 1585 (2004). [p. 7]

[32] Davis, A.H. and Bussmann, K. *Organic luminescent devices and magnetoelectronics*. J. Appl. Phys. **93**, 7358 (2003). [p. 14]

[33] Davis, A.H. and Bussmann, K. *Large magnetic field effects in organic light emitting diodes based on tris(8-hydroxyquinoline aluminum) (Alq_3)/N,N′-Di(naphthalen-1-yl)-N,N′diphenyl-benzidine (NPB) bilayers*. J. Vac. Sci. Technol. A **22**, 1885 (2004). [p. 20]

[34] Dediu, V., Hueso, L.E., Bergenti, I., Riminucci, A., Borgatti, F., Graziosi, P., Newby, C., Casoli, F., De Jong, M.P., Taliani, C., and Zhan, Y. *Room-temperature spintronic effects in Alq_3-based hybrid devices*. Phys. Rev. B **78**, 115203 (2008). [p. 15, 68, 69, and 77]

[35] Dediu, V., Murgia, M., Matacotta, F., Taliani, C., and Barbanera, S. *Room temperature spin polarized injection in organic semiconductor*. Solid State Commun. **122**, 181 (2002). [p. 15, 68, 69, and 72]

[36] Dediu, V.A., Hueso, L.E., Bergenti, I., and Taliani, C. *Spin routes in organic semiconductors*. Nat. Mater. **8**, 707 (2009). [p. 14, 15, and 17]

[37] Desai, P., Shakya, P., Kreouzis, T., and Gillin, W.P. *Magnetoresistance in organic light-emitting diode structures under illumination*. Phys. Rev. B **76**, 235202 (2007). [p. 18, 25, and 34]

[38] Desai, P., Shakya, P., Kreouzis, T., and Gillin, W.P. *The role of magnetic fields on the transport and efficiency of aluminum tris(8-hydroxyquinoline) based organic light emitting diodes*. J. Appl. Phys. **102**, 073710 (2007). [p. 18]

[39] Desai, P., Shakya, P., Kreouzis, T., Gillin, W.P., Morley, N.A., and Gibbs, M.R.J. *Magnetoresistance and efficiency measurements of Alq_3-based OLEDs*. Phys. Rev. B **75**, 094423 (2007). [p. 18, 25, 28, 33, 34, 43, and 68]

[40] Drew, A.J., Hoppler, J., Schulz, L., Pratt, F.L., Desai, P., Shakya, P., Kreouzis, T., Gillin, W.P., Suter, A., Morley, N.A., Malik, V.K., Dubroka, A., Kim, K.W., Bouyanfif, H., Bourqui, F., Bernhard, C., Scheuermann, R., Nieuwenhuys, G.J., Prokscha, T., and Morenzoni, E. *Direct measurement of the electronic spin diffusion length in a fully functional organic spin valve by low-energy muon spin rotation*. Nat. Mater. **8**, 109 (2009). [p. 16, 68, 69, and 72]

[41] Ern, V. and Merrifield, R.E. *Magnetic field effect on triplet exciton quenching in organic crystals*. Phys. Rev. Lett. **21**, 609 (1968). [p. 25]

[42] Forrest, S.R. *The path to ubiquitous and low-cost organic electronic appliances on plastic*. Nature **428**, 911 (2004). [p. 7]

[43] Francis, T., Mermer, Ö., Veeraraghavan, G., and Wohlgenannt, M. *Large magnetoresistance at room temperature in semiconducting polymer sandwich devices*. New J. Phys. **6**, 185 (2004). [p. 17, 19, and 57]

[44] Frankevich, E.L., Lymarev, A.A., Sokolik, I., Karasz, F.E., Blumstengel, S., Baughman, R.H., and Hörhold, H.H. *Polaron-pair generation in poly(phenylene vinylenes)*. Phys. Rev. B **46**, 9320 (1992). [p. 18, 23, and 24]

[45] Gärditz, C., Mückl, A.G., and Cölle, M. *Influence of an external magnetic field on the singlet and triplet emissions of tris-(8-hydroxyquinoline)aluminum(iii) (Alq_3)*. J. Appl. Phys. **98**, 104507 (2005). [p. 18]

[46] Godlewski, J., Jarosz, G., and Signerski, R. *Photoenhanced current in thin organic layers*. Appl. Surf. Sci. **175-176**, 344 (2001). [p. 25]

[47] Gómez, J., Nüesch, F., Zuppiroli, L., and Graeff, C. *Magnetic field effects on the conductivity of organic bipolar and unipolar devices at room temperature*. Synth. Met. **160**, 317 (2010). [p. 19]

[48] Gommans, H.H.P., Kemerink, M., Andersson, G.G., and Pijper, R.M.T. *Charge transport and trapping in Cs-doped poly(dialkoxy-p-phenylene vinylene) light-emitting diodes*. Phys. Rev. B **69**, 155216 (2004). [p. 54]

[49] Gommans, H., Kemerink, M., and Janssen, R. *Negative capacitances in low-mobility solids*. Phys. Rev. B **72**, (2005). [p. 51 and 54]

[50] Groff, R.P., Suna, A., Avakian, P., and Merrifield, R.E. *Magnetic hyperfine modulation of dye-sensitized delayed fluorescence in organic crystals*. Phys. Rev. B **9**, 2655 (1974). [p. 58 and 65]

[51] Guyot-Sionnest, P., Yu, D., Jiang, P.h., and Kang, W. *Spin blockade in the conduction of colloidal cdse nanocrystal films*. J. Chem. Phys. **127**, 014702 (2007). [p. 23]

[52] Hartenstein, B., Bässler, H., Jakobs, A., and Kehr, K.W. *Comparison between multiple trapping and multiple hopping transport in a random medium*. Phys. Rev. B **54**, 8574 (1996). [p. 70]

[53] Helbig, M. and Hörhold, H.H. *Investigation of poly(arylenevinylene)s, 40. electrochemical studies on poly(p-phenylenevinylene)s*. Die Makromolekulare Chemie **194**, 1607 (1993). [p. 23]

[54] Hu, B. and Wu, Y. *Tuning magnetoresistance between positive and negative values in organic semiconductors*. Nat. Mater. **6**, 985 (2007). [p. 18, 26, and 30]

[55] Hu, B., Yan, L., and Shao, M. *Magnetic-field effects in organic semiconducting materials and devices*. Adv. Mater. **21**, 1500 (2009). [p. 17, 25, 26, 29, and 51]

[56] Iwasaki, Y., Osasa, T., Asahi, M., Matsumura, M., Sakaguchi, Y., and Suzuki, T. *Fractions of singlet and triplet excitons generated in organic light-emitting devices based on a polyphenylenevinylene derivative*. Phys. Rev. B **74**, 195209 (2006). [p. 18 and 23]

[57] Janssen, R. and Graetzel, M. *Themed issue: solar cells*. J. Mater. Chem. **19**, 5276 (2009). [p. 7]

[58] Jedema, F.J., Heersche, H.B., Filip, A.T., Baselmans, J.J.A., and van Wees, B.J. *Electrical detection of spin precession in a metallic mesoscopic spin valve*. Nature **416**, 713 (2002). [p. 16, 80, and 86]

[59] Jiang, J.S., Pearson, J.E., and Bader, S.D. *Absence of spin transport in the organic semiconductor Alq_3*. Phys. Rev. B **77**, 035303 (2008). [p. 15 and 17]

[60] Johnson, R. and Merrifield, R. *Effects of magnetic fields on the mutual annihilation of triplet excitons in anthracene crystals*. Phys. Rev. B **1**, 896 (1970). [p. 16, 26, 62, 80, and 86]

[61] Kadashchuk, A., Arkhipov, V.I., Kim, C.H., Shinar, J., Lee, D.W., Hong, Y.R., Jin, J.I., Heremans, P., and Bässler, H. *Localized trions in conjugated polymers*. Phys. Rev. B **76**, 235205 (2007). [p. 28]

[62] Kalinowski, J., Cocchi, M., Virgili, D., Di Marco, P., and Fattori, V. *Magnetic field effects on emission and current in Alq_3-based electroluminescent diodes*. Chem. Phys. Lett. **380**, 710 (2003). [p. 18, 23, and 68]

[63] Kutzler, F.W., White, C.T., and Cook, M. *Local spin-density calculations of anisotropic hyperfine constants in oriented free radicals*. Chem. Phys. Lett. **147**, 263 (1988). [p. 65]

[64] Lin, B.C., Cheng, C.P., You, Z.Q., and Hsu, C.P. *Charge transport properties of tris(8-hydroxyquinolinato)aluminum(III): Why it is an electron transporter*. J. Am. Chem. Soc.

127, 66 (2005). [p. 65]

[65] Liu, R., Zhang, Y., Lei, Y.L., Chen, P., and Xiong, Z.H. *Magnetic field dependent triplet-triplet annihilation in Alq_3-based organic light emitting diodes at different temperatures*. J. Appl. Phys. **105**, 093719 (2009). [p. 20 and 31]

[66] Lou, X., Adelmann, C., Crooker, S.A., Garlid, E.S., Zhang, J., Reddy, K.S.M., Flexner, S.D., Palmstrom, C.J., and Crowell, P.A. *Electrical detection of spin transport in lateral ferromagnet-semiconductor devices*. Nat. Phys. **3**, 197 (2007). [p. 16, 80, and 86]

[67] Lupton, J.M. and Boehme, C. *Magnetoresistance in organic semiconductors*. Nat. Mater. **7**, 598 (2008). [p. 26]

[68] Majumdar, S., Laiho, R., Laukkanen, P., Vayrynen, I.J., Majumdar, H.S., and Österbacka, R. *Application of regioregular polythiophene in spintronic devices: Effect of interface*. Appl. Phys. Lett. **89**, 122114 (2006). [p. 68, 69, and 72]

[69] Majumdar, S., Majumdar, H.S., Aarnio, H., and Österbacka, R. *Hysteretic magnetoresistance in polymeric diodes*. Phys. Status Solidi RRL **3**, 242 (2009). [p. 52]

[70] Majumdar, S., Majumdar, H.S., Aarnio, H., Vanderzande, D., Laiho, R., and Österbacka, R. *Role of electron-hole pair formation in organic magnetoresistance*. Phys. Rev. B **79**, 201202 (2009). [p. 18 and 20]

[71] Majumdar, S., Majumdar, H.S., Laiho, R., and Österbacka, R. *Comparing small molecules and polymer for future organic spin-valves*. J. Alloys Compd. **423**, 169 (2006). [p. 15]

[72] Majumdar, S., Majumdar, H.S., Tobjörk, D., and Österbacka, R. *Towards printed magnetic sensors based on organic diodes*. Phys. Status Solidi A **206**, 2198 (2009). [p. 101]

[73] Manriquez, J.M., Yee, G.T., Mclean, R.S., Epstein, A.J., and Miller, J.S. *A room-temperature molecular/organic-based magnet*. Science **252**, 1415 (1991). [p. 14]

[74] Martens, H.C.F., Huiberts, J.N., and Blom, P.W.M. *Simultaneous measurement of electron and hole mobilities in polymer light-emitting diodes*. Appl. Phys. Lett. **77**, 1852 (2000). [p. 51 and 54]

[75] Martin, J., Bergeson, J., Prigodin, V., and Epstein, A. *Magnetoresistance for organic semiconductors: Small molecule, oligomer, conjugated polymer, and non-conjugated polymer*. Synth. Met. **160**, 291 (2010). [p. 23]

[76] McCamey, D.R., Seipel, H.A., Paik, S.Y., Walter, M.J., Borys, N.J., Lupton, J.M., and Boehme, C. *Spin rabi flopping in the photocurrent of a polymer light-emitting diode*. Nat. Mater. **7**, 723 (2008). [p. 14]

[77] McConnell, H.M. *Indirect hyperfine interactions in the paramagnetic resonance spectra of aromatic free radicals*. J. Chem. Phys. **24**, 764 (1956). [p. 16]

[78] Mensink, R. *Putting physical parameters into the two-site bipolaron model*. Bachelor's thesis, Eindhoven University of Technology (2009). [p. 90 and 91]

[79] Mermer, Ö., Veeraraghavan, G., Francis, T., Sheng, Y., Nguyen, D., Wohlgenannt, M., Kohler, A., Al-Suti, M., and Khan, M. *Large magnetoresistance in nonmagnetic π-conjugated semiconductor thin film devices*. Phys. Rev. B **72**, 205202 (2005). [p. 17, 18, 19, 20, 29, 36, 43, 58, 92, 95, and 96]

[80] Mermer, Ö., Veeraraghavan, G., Francis, T., and Wohlgenannt, M. *Large magnetoresistance at room-temperature in small-molecular-weight organic semiconductor sandwich devices*. Solid State Commun. **134**, 631 (2005). [p. 18]

[81] Merrifield, R.E. *Theory of magnetic field effects on the mutual annihilation of triplet excitons*. J. Chem. Phys. **48**, 4318 (1968). [p. 26]

[82] Meruvia, M.S., Freire, J.A., Hummelgen, I.A., Gruber, J., and Graeff, C.F.O. *Magnetic field release of trapped charges in poly(fluorenylenevinylene)s.* Org. Electron. **8**, 695 (2007). [p. 52]

[83] Miller, A. and Abrahams, E. *Impurity conduction at low concentrations*. Phys. Rev. **120**, 745 (1960). [p. 68 and 80]

[84] Moodera, J.S., Kinder, L.R., Wong, T.M., and Meservey, R. *Large magnetoresistance at room temperature in ferromagnetic thin film tunnel junctions.* Phys. Rev. Lett. **74**, 3273 (1995). [p. 13]

[85] Morley, N.A., Rao, A., Dhandapani, D., Gibbs, M.R.J., Grell, M., and Richardson, T. *Room temperature organic spintronics.* J. Appl. Phys. **103**, 07F306 (2008). [p. 15]

[86] Movaghar, B. and Schweitzer, L. *A model for the anomalous magnetoresistance in amorphous semiconductors.* Journal of Physics C: Solid State Physics **11**, 125 (1977). [p. 23]

[87] Naber, W.J.M., Faez, S., and Wiel, W.G.v.d. *Organic spintronics.* J. Phys. D: Appl. Phys. **40**, R205 (2007). [p. 14 and 15]

[88] Nagata, Y. and Lennartz, C. *Atomistic simulation on charge mobility of amorphous tris(8-hydroxyquinoline) aluminum (Alq_3): Origin of Poole–Frenkel–type behavior*. J. Chem. Phys. **129**, 034709 (2008). [p. 72]

[89] Nguyen, T.D., Rybicki, J., Sheng, Y., and Wohlgenannt, M. *Device spectroscopy of magnetic field effects in a polyfluorene organic light-emitting diode.* Phys. Rev. B **77**, 035210 (2008). [p. 30]

[90] Nguyen, T.D., Sheng, Y., Rybicki, J., and Wohlgenannt, M. *Magnetic field-effects in bipolar, almost hole-only and almost electron-only tris-(8-hydroxyquinoline) aluminum devices*. Phys. Rev. B **77**, 235209 (2008). [p. 18, 20, 28, 29, and 56]

[91] Nguyen, T., Sheng, Y., Rybicki, J., Veeraraghavan, G., and Wohlgenannt, M. *Device-spectroscopy of magnetic field effects in several different polymer organic light-emitting diodes.* Synth. Met. **160**, 320 (2010). [p. 20, 30, and 31]

[92] Nguyen, T.D., Hukic-Markosian, G., Wang, F., Wojcik, L., Li, X.G., Ehrenfreund, E., and Vardeny, Z.V. *Isotope effect in spin response of π-conjugated polymer films and devices.* Nat. Mater. **9**, 345 (2010). [p. 16, 27, 79, 92, 97, and 101]

[93] Nguyen, T.D., Sheng, Y., Rybicki, J., Veeraraghavan, G., and Wohlgenannt, M. *Magnetoresistance in π-conjugated organic sandwich devices with varying hyperfine and spin-orbit coupling strengths, and varying dopant concentrations.* J. Mater. Chem. **17**, 1995 (2007). [p. 18]

[94] Nguyen, T.D., Sheng, Y., Rybicki, J.E., and Wohlgenannt, M. *Magnetoconductivity and magnetoluminescence studies in bipolar and almost hole-only sandwich devices made from films of a π-conjugated molecule.* Sci. Technol. Adv. Mater. **9**, 024206 (2008). [p. 18]

[95] Niedermeier, U., Bagnich, S., Melzer, C., Sarfert, W., and von Seggern, H. *Tuning of organic magnetoresistance by reversible modification of the active material.* Synth. Met. **160**, 251 (2010). [p. 18]

[96] Niedermeier, U., Vieth, M., Patzold, R., Sarfert, W., and von Seggern, H. *Enhancement of organic magnetoresistance by electrical conditioning.* Appl. Phys. Lett. **92**, 193309 (2008). [p. 18, 19, 23, 34, and 38]

[97] Niedermeier, U. *Magnetic field effect in organic light emitting diodes.* Ph.D. thesis, Technische Universität Darmstadt (2010). [p. 21, 24, 27, and 30]

[98] Niedermeier, U., Sarfert, W., and von Seggern, H. *Influence of a magnetic field on the*

device performance of OLEDs. In *Organic Optoelectronics and Photonics III*, vol. 6999, pp. 699913–9. SPIE, Strasbourg, France (2008). [p. 19]

[99] Odaka, H., Okimoto, Y., Yamada, T., Okamoto, H., Kawasaki, M., and Tokura, Y. *Control of magnetic-field effect on electroluminescence in alq[sub 3]-based organic light emitting diodes*. Appl. Phys. Lett. **88**, 123501 (2006). [p. 18 and 23]

[100] O'Dea, A.R., Curtis, A.F., Green, N.J.B., Timmel, C.R., and Hore, P.J. *Influence of dipolar interactions on radical pair recombination reactions subject to weak magnetic fields*. J. Phys. Chem. A **109**, 869 (2005). [p. 63]

[101] Parmenter, R.H. and Ruppel, W. *Two-carrier space-charge-limited current in a trap-free insulator*. J. Appl. Phys. **30**, 1548 (1959). [p. 11 and 38]

[102] Pasveer, W.F., Cottaar, J., Tanase, C., Coehoorn, R., Bobbert, P.A., Blom, P.W.M., de Leeuw, D.M., and Michels, M.A.J. *Unified description of charge-carrier mobilities in disordered semiconducting polymers*. Phys. Rev. Lett. **94**, 206601 (2005). [p. 68, 69, 70, and 72]

[103] Petta, J.R., Slater, S.K., and Ralph, D.C. *Spin-dependent transport in molecular tunnel junctions*. Phys. Rev. Lett. **93**, 136601 (2004). [p. 68 and 69]

[104] Pikus, G. and Titkov, A. *Optical Orientation*, chap. 3. Eds. F. Meier and B.P. Zakharchenya, North-Holland, Amsterdam (1984). [p. 68]

[105] Prigodin, V.N. and Epstein, A.J. *Spin dynamics control of recombination current in organic semiconductors*. Synth. Met. **160**, 244 (2010). [p. 23]

[106] Prigodin, V., Bergeson, J., Lincoln, D., and Epstein, A. *Anomalous room temperature magnetoresistance in organic semiconductors*. Synth. Met. **156**, 757 (2006). [p. 23, 24, 33, 34, 43, 57, 63, 68, and 93]

[107] Pulizzi, F. *A new face for organics*. Nat. Mater. **8**, 696 (2009). [p. 17]

[108] Reufer, M., Walter, M.J., Lagoudakis, P.G., Hummel, A.B., Kolb, J.S., Roskos, H.G., Scherf, U., and Lupton, J.M. *Spin-conserving carrier recombination in conjugated polymers*. Nat. Mater. **4**, 340 (2005). [p. 30]

[109] Rocha, A.R., Garcia-suarez, V.M., Bailey, S.W., Lambert, C.J., Ferrer, J., and Sanvito, S. *Towards molecular spintronics*. Nat. Mater. **4**, 335 (2005). [p. 14 and 68]

[110] Rolfe, N., Desai, P., Shakya, P., Kreouzis, T., and Gillin, W.P. *Separating the roles of electrons and holes in the organic magnetoresistance of aluminum tris(8-hydroxyquinoline) organic light emitting diodes*. J. Appl. Phys. **104**, 083703 (2008). [p. 34 and 41]

[111] Rolfe, N.J., Heeney, M., Wyatt, P.B., Drew, A.J., Kreouzis, T., and Gillin, W.P. *Elucidating the role of hyperfine interactions on organic magnetoresistance using deuterated aluminium tris(8-hydroxyquinoline)*. Phys. Rev. B **80**, 241201 (2009). [p. 27]

[112] Salaneck, W.R., Friend, R.H., and BrÃĽdas, J.L. *Electronic structure of conjugated polymers: consequences of electron-lattice coupling*. Physics Reports **319**, 231 (1999). [p. 28]

[113] Salis, G., Alvarado, S.F., Tschudy, M., Brunschwiler, T., and Allenspach, R. *Hysteretic electroluminescence in organic light-emitting diodes for spin injection*. Phys. Rev. B **70**, 085203 (2004). [p. 14]

[114] Santos, T.S., Lee, J.S., Migdal, P., Lekshmi, I.C., Satpati, B., and Moodera, J.S. *Room-temperature tunnel magnetoresistance and spin-polarized tunneling through an organic semiconductor barrier*. Phys. Rev. Lett. **98**, 016601 (2007). [p. 17 and 68]

[115] Sanvito, S. *Spintronics goes plastic*. Nat. Mater. **6**, 803 (2007). [p. 14 and 16]

[116] Schellekens, A.J. *Exploring spin interactions in organic semiconductors*. Master's thesis,

Eindhoven University of Technology (2010). [p. 20, 25, 26, 27, 28, 30, 93, and 98]

[117] Scher, H. and Montroll, E.W. *Anomalous transit-time dispersion in amorphous solids*. Phys. Rev. B **12**, 2455 (1975). [p. 70 and 85]

[118] Schmidt, G. *Concepts for spin injection into semiconductors—a review*. J. Phys. D: Appl. Phys. **38**, R107 (2005). [p. 12 and 14]

[119] Schmidt, G., Ferrand, D., Molenkamp, L.W., Filip, A.T., and van Wees, B.J. *Fundamental obstacle for electrical spin injection from a ferromagnetic metal into a diffusive semiconductor*. Phys. Rev. B **62**, R4790 (2000). [p. 14 and 17]

[120] Schoonus, J.J.H.M., Lumens, P.G.E., Wagemans, W., Kohlhepp, J.T., Bobbert, P.A., Swagten, H.J.M., and Koopmans, B. *Magnetoresistance in hybrid organic spin valves at the onset of multiple-step tunneling*. Phys. Rev. Lett. **103**, 146601 (2009). [p. 17]

[121] Schulten, K. and Wolynes, P.G. *Semiclassical description of electron spin motion in radicals including the effect of electron hopping*. J. Chem. Phys. **68**, 3292 (1978). [p. 16, 63, 65, 68, and 81]

[122] Shakya, P., Desai, P., Kreouzis, T., and Gillin, W.P. *Magnetoresistance in triphenyl-diamine derivative blue organic light emitting devices*. J. Appl. Phys. **103**, 043706 (2008). [p. 18]

[123] Shakya, P., Desai, P., Somerton, M., Gannaway, G., Kreouzis, T., and Gillin, W.P. *The magnetic field effect on the transport and efficiency of group iii tris(8-hydroxyquinoline) organic light emitting diodes*. J. Appl. Phys. **103**, 103715 (2008). [p. 18 and 93]

[124] Sheng, Y., Nguyen, T.D., Veeraraghavan, G., Mermer, Ö., and Wohlgenannt, M. *Effect of spin-orbit coupling on magnetoresistance in organic semiconductors*. Phys. Rev. B **75**, 035202 (2007). [p. 18 and 34]

[125] Sheng, Y., Nguyen, T.D., Veeraraghavan, G., Mermer, Ö., Wohlgenannt, M., Qiu, S., and Scherf, U. *Hyperfine interaction and magnetoresistance in organic semiconductors*. Phys. Rev. B **74**, 045213 (2006). [p. 18, 23, 27, 92, 93, and 96]

[126] Shim, J.H., Raman, K.V., Park, Y.J., Santos, T.S., Miao, G.X., Satpati, B., and Moodera, J.S. *Large spin diffusion length in an amorphous organic semiconductor*. Phys. Rev. Lett. **100**, 226603 (2008). [p. 17]

[127] Shinar, J. and Shinar, R. *Organic light-emitting devices (OLEDs) and OLED-based chemical and biological sensors: an overview*. J. Phys. D: Appl. Phys. **41**, 133001 (2008). [p. 101]

[128] Silvestre, G., Johnson, M., Giraldo, A., and Shannon, J. *Light degradation and voltage drift in polymer light-emitting diodes*. Appl. Phys. Lett. **78**, 1619 (2001). [p. 34 and 37]

[129] Steiner, U.E. and Ulrich, T. *Magnetic field effects in chemical kinetics and related phenomena*. Chemical Reviews **89**, 51 (1989). [p. 17]

[130] Stingelin-Stutzmann, N., Smits, E., Wondergem, H., Tanase, C., Blom, P., Smith, P., and de Leeuw, D. *Organic thin-film electronics from vitreous solution-processed rubrene hypereutectics*. Nat. Mater. **4**, 601 (2005). [p. 7]

[131] Sun, Z., Li, Y., Gao, K., Liu, D., An, Z., and Xie, S. *Dynamical study of polaron-bipolaron scattering in conjugated polymers*. Org. Electron. **11**, 279 (2010). [p. 28]

[132] Szulczewski, G., Tokuc, H., Oguz, K., and Coey, J.M.D. *Magnetoresistance in magnetic tunnel junctions with an organic barrier and an MgO spin filter*. Appl. Phys. Lett. **95**, 202506 (2009). [p. 17]

[133] Tajima, H., Miyakawa, M., Isozaki, H., Yasui, M., Suzuki, N., and Matsuda, M. *Magnetophotocurrent effect in organic photovoltaic cells at low temperatures*. Synth. Met. **160**, 256 (2010). [p. 20]

[134] Tombros, N., Jozsa, C., Popinciuc, M., Jonkman, H.T., and van Wees, B.J. *Electronic spin transport and spin precession in single graphene layers at room temperature*. Nature **448**, 571 (2007). [p. 102]

[135] van der Waals, J. and ter Maten, G. *Zero-field splitting of the lowest triplet state of some aromatic hydrocarbons: Calculation and comparison with experiment*. Mol. Phys. **8**, 301 (1964). [p. 25]

[136] van Mensfoort, S.L.M. *Effects of disorder on the charge transport and recombination in organic light-emitting diodes*. Ph.D. thesis, Eindhoven University of Technology (2009). [p. 8]

[137] Vardeny, Z.V. *Spintronics organics strike back*. Nat. Mater. **8**, 91 (2009). [p. 16]

[138] Veeraraghavan, G., Nguyen, T.D., Sheng, Y., Mermer, Ö., and Wohlgenannt, M. *An 8 x 8 pixel array pen-input OLED screen based on organic magnetoresistance*. IEEE T. Electron. Dev. **54**, 1571 (2007). [p. 14, 18, and 52]

[139] Vinzelberg, H., Schumann, J., Elefant, D., Gangineni, R.B., Thomas, J., and Buechner, B. *Low temperature tunneling magnetoresistance on (La,Sr)MnO_3/Co junctions with organic spacer layers*. J. Appl. Phys. **103**, 093720 (2008). [p. 15 and 80]

[140] Žutić, I., Fabian, J., and Das Sarma, S. *Spintronics: Fundamentals and applications*. Rev. Mod. Phys. **76**, 323 (2004). [p. 12 and 13]

[141] Wagemans, W., Bloom, F.L., Bobbert, P.A., Wohlgenannt, M., and Koopmans, B. *A two-site bipolaron model for organic magnetoresistance*. J. Appl. Phys. **103**, 07F303 (2008). [p. 21, 33, 41, and 56]

[142] Wagemans, W., Engelen, W., Bloom, F., and Koopmans, B. *Separating photocurrent and injected current contributions to the organic magnetoresistance*. Synth. Met. **160**, 266 (2010). [p. 52, 53, and 58]

[143] Wang, F.J., Bässler, H., and Vardeny, Z.V. *Magnetic field effects in π-conjugated polymer-fullerene blends: Evidence for multiple components*. Phys. Rev. Lett. **101**, 236805 (2008). [p. 18, 20, 23, 28, 29, 31, 34, 56, and 66]

[144] Wang, F.J., Yang, C.G., Vardeny, Z.V., and Li, X.G. *Spin response in organic spin valves based on $La_{2/3}Sr_{1/3}MnO_3$ electrodes*. Phys. Rev. B **75**, 245324 (2007). [p. 15, 68, 69, and 77]

[145] Wohlgenannt, M., Tandon, K., Mazumdar, S., Ramasesha, S., and Vardeny, Z.V. *Formation cross-sections of singlet and triplet excitons in π-conjugated polymers*. Nature **409**, 494 (2001). [p. 11]

[146] Wolf, S.A., Awschalom, D.D., Buhrman, R.A., Daughton, J.M., von Molnar, S., Roukes, M.L., Chtchelkanova, A.Y., and Treger, D.M. *Spintronics: A spin-based electronics vision for the future*. Science **294**, 1488 (2001). [p. 12 and 67]

[147] Wu, Y., Xu, Z., Hu, B., and Howe, J. *Tuning magnetoresistance and magnetic-field-dependent electroluminescence through mixing a strong-spin-orbital-coupling molecule and a weak-spin-orbital-coupling polymer*. Phys. Rev. B **75**, 035214 (2007). [p. 18, 23, 33, and 34]

[148] Xin, L., Li, C., Li, F., Liu, S., and Hu, B. *Inversion of magnetic field effects on electrical current and electroluminescence in tri-(8-hydroxyquinoline)-aluminum based light-emitting diodes*. Appl. Phys. Lett. **95**, 123306 (2009). [p. 18]

[149] Xiong, Z.H., Wu, D., Vardeny, Z.V., and Shi, J. *Giant magnetoresistance in organic spin-valves*. Nature **427**, 821 (2004). [p. 15, 68, 69, 72, 73, 76, 77, and 102]

[150] Xu, W., Szulczewski, G.J., LeClair, P., Navarrete, I., Schad, R., Miao, G., Guo, H., and Gupta, A. *Tunneling magnetoresistance observed in $La_{0.67}Sr_{0.33}MnO_3$/organic molecule/Co junc-*

tions. Appl. Phys. Lett. **90**, 072506 (2007). [p. 15]

[151] Xu, Z. and Hu, B. *Photovoltaic processes of singlet states in organic solar cells*. Adv. Funct. Mater. **18**, 2611 (2008). [p. 20, 26, 30, and 34]

[152] Yang, C.G., Ehrenfreund, E., and Vardeny, Z.V. *Polaron spin-lattice relaxation time in π-conjugated polymers from optically detected magnetic resonance*. Phys. Rev. Lett. **99**, 157401 (2007). [p. 14]

[153] Yoo, J.W., Jang, H., Prigodin, V., Kao, C., Eom, C., and Epstein, A. *Tunneling vs. giant magnetoresistance in organic spin valve*. Synth. Met. **160**, 216 (2010). [p. 17]

[154] Yusoff, A.R.B.M., da Silva, W.J., Serbena, J.P.M., Meruvia, M.S., and Hummelgen, I.A. *Very high magnetocurrent in tris-(8-hydroxyquinoline) aluminum-based bipolar charge injection devices*. Appl. Phys. Lett. **94**, 253305 (2009). [p. 18, 19, and 28]

Index

Admittance, 53
Alq_3, 9

Bipolar, *see* Double carrier
Bipolaron, 10, 21, 23, 44
Bipolaron formation energy (U), 23, 90
Bipolaron model, 28, 56
Branching ratio, 23, 41, 45, 91, 94
Built-in voltage, 10

Capacitance, 53, 54
Charge injection, 9
    Injection barrier, 10
    Ohmic contact, 10
Charge localization, 8
Charge transport, 11, 54
Conductivity mismatch, 14, 17
Coulomb interaction, 10, 23, 28, 45
Current–voltage, 38
    Double-carrier device, 11
    Power law, 11, 38
    Single-carrier device, 11
    Trapping, 11

Density matrix, 62
Density of states
    Gaussian, 8, 68
Deuteration, 16, 27
dI/dB, 35, 36
Dipole coupling, 60, 63
Disorder, 8, 68, 77, 80, 85, 90
Displacement vector, 60
dMC/dB, 52
Double-carrier device, 10

e–h pair, *see* Electron–hole pair
Electrical device
    Energy diagram, 9
    Layout, 9
Electroluminescence, 10
Electron–hole pair, 10, 23
    Dissociation, 23
    Recombination, 23
Exchange interaction, 10, 60, 63
Exciton, 10, 12, 23, 25
Exciton–charge interaction, 25
Exciton–exciton interaction, 26

Giant magnetoresistance, 12
GMR, *see* Giant magnetoresistance

Hanle experiment, 16, 80, 86
HOMO, 8, 9
Hopping time distribution
    Algebraic, 85
    Gamma, 85
    Gaussian, 84, 87
Hopping transport, 8, 68, 80, 90
Hyperfine field, 16, 21, 27, 46, 60, 63, 68, 81

Liouville equation, 62, 98
LSMO, 15
LUMO, 8, 9

Magnetic tunnel junction, 13
Magnetoconductance, 18, 35
Magnetoresistance, 13, 18
Magnetoresistance curve, 87
Majority carriers, 11, 55
MC, *see* Magnetoconductance

MC Spinner, 35
Minority carriers, 11, 55
Modulation
  Illumination, 35, 39
  Magnetic field, 35, 36, 51
Monte Carlo, 69, 81, 89
Motional narrowing, 69, 83
MR, *see* Magnetoresistance

OLED, *see* Organic light-emitting diode
OMAR, *see* Organic magnetoresistance
Organic electronics, 7
Organic light-emitting diode, 7, 10, 14
Organic magnetoresistance, 17, 33
  Angle dependence, 57
  Bulk effect, 18
  Conditioning, 19, 23, 38
  Drift, 34, 36
  Electroluminescence, 18, 30
  Frequency dependence, 51
  High field effects, 20
  Magnetoconductance, 18
  Measuring, 35
  Phosphorescence, 30
  Photocurrent, 18, 29, 38
  Sign change, 18, 23–25, 29, 47
  Single-carrier devices, 20, 28
  Singlet and triplet density, 30
  Spin polarization, 97
  Spin–spin interactions, 57
  Temperature dependence, 18
  Trapping, 29, 52
  Traps, 23, 25, 37
  Voltage dependence, 18, 24, 29, 35, 52, 58, 96
Organic magnetoresistance lineshape, 23, 27, 30, 39, 46, 63, 99
  Alternative approach, 92
  B_0, 18, 40, 58, 93
  Broadening, 27, 47, 93
  Lorentzian, 18, 94
  Non-Lorentzian, 18, 94
Organic magnetoresistance models, 20
  Bipolaron model, 21, 43, 62, 89, 97
  e–h pair model, 23, 30, 62, 98
  Exciton–charge interaction model, 25, 31, 93
Organic materials
  Conduction, 8
  Mobilities, 8, 11, 70
  π-conjugation, 8
  Semiconducting, 8
  Typical examples, 9
Organic spin valve, 15, 87
  Hybrid barrier, 17
  Tunneling, 15, 17
Organic spintronics, 14

Photocurrent, 11
Photoluminescence, 12
Polaron, 10
PPV, 9

Recombination, 10, 11
Recombination mobility, 11, 55, 63

Sample fabrication, 9, 34
SCLC, *see* space-charge limited conduction
Single-carrier device, 10
Singlet, 10, 60
Singlet–triplet ratio, 11, 14, 97
Space-charge limited current, 11
Spin accumulation, 75, 87
Spin blocking, 21, 44, 91
Spin-coherence length, 82
Spin-diffusion length, 13–17, 69, 74, 79, 82, 98
Spin injection, 14, 77, 87
Spin lifetime, 14
Spin manipulation, 13, 16, 79
Spin mixing, 60
Spin–orbit coupling, 14, 30
Spin polarization, 12, 69, 74
Spin precession, 16, 21, 60, 68, 81
Spin transport, 12, 15, 67, 97
Spin valve, 12
  Modeling, 72
  MR(B), 13, 15, 73, 75, 87
  Switching, 13, 15, 73, 75
Spintronics, 12

Transit time, 51, 54
Trapping, 11, 54
Trion, 28
Triplet, 10, 60
Two-site bipolaron model, 43, 89

Unipolar, *see* Single carrier

Waiting-time distribution, 70, 83

Zero-field splitting, 25